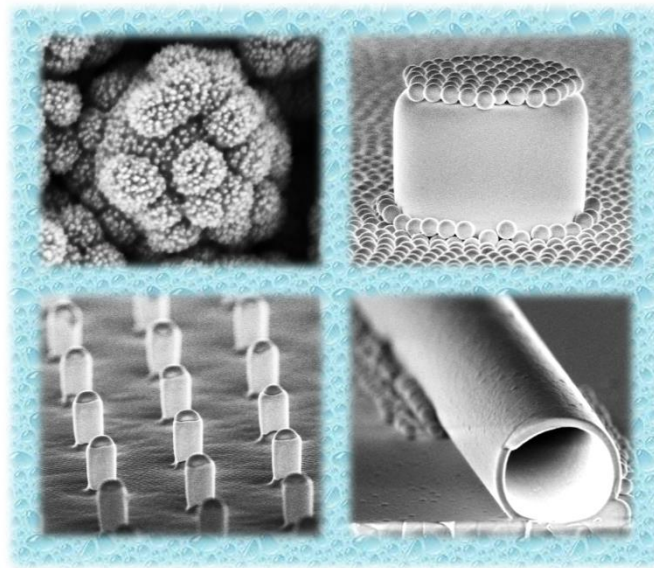# CONTROLLED WETTING ON SILICA-BASED NANO- AND MICROSTRUCTURED SURFACES

DISSERTATION

zur Erlangung des Grades

„Doktor der Naturwissenschaften"

im Promotionsfach Chemie

am Fachbereich Chemie, Pharmazie und Geowissenschaften

der Johannes Gutenberg-Universität

in Mainz

Lena Mammen

geboren in Heidelberg

Mainz, November 2013

Die vorliegende Arbeit wurde in der Zeit von August 2010 bis November 2013 unter der Betreuung von [In der elektronischen Fassung aus Datenschutzgründen entfernt] am Max-Planck-Institut für Polymerforschung in Mainz angefertigt.

„Die Erde ist ein gebildeter Stern

mit sehr viel Wasserspülung.“

ERICH KÄSTNER

TABLE OF CONTENTS

ABSTRACT

This thesis focuses on the controlled wetting of solid surfaces which is of great interest in many fields such as microfluidics, coatings and biological studies of cells or bacteria.

The first part deals with the question how nanoroughness influences the wetting behaviour i.e. the contact angles and pinning strength of hydrophobic and superhydrophobic coatings. For this purpose, a novel method to introduce a nanorough silica coating in vapour phase is developed and superimposed onto a superhydrophobic surface consisting of rough polystyrene-silica core-shell particles. It is found that the topography and density of the silica nanoasperities determine whether superhydrophobic behaviour is impaired or enhanced i.e. whether the liquid drop is in the nano-Wenzel or nano-Cassie state. In the nano-Wenzel state the pinning is increased caused by penetration of liquid molecules into nanopores whereas in the nano-Cassie state the liquid sits on top of the nanoasperities leading to a reduced pinning strength. These experimental results are related to molecular dynamics simulations of the influence of the surface coating density and length of semifluorinated silanes on the hydrophobicity of a surface.

Several techniques have been developed to fabricate transparent superhydrophobic i.e. highly liquid repellent surfaces. A current challenge is it to pattern a superhydrophobic surface with functionalities while maintaining the superhydrophobic properties. This is demanding as most of the functional groups are hydrophilic. In this work a sophisticated procedure to fabricate transparent superhydrophobic Janus micropillar arrays with variable dimensions and topographies is created. The Janus pillars possess hydrophobic sidewalls and hydrophilic silica tops enabling a selective post-functionalization of the top sides without losing the superhydrophobic properties of the surface. The selective surface functionalization is illustrated with confocal microscopy by chemically binding fluorescent molecules to the pillar top sides. It is shown that the wetting behaviour is controlled by the solid-liquid interactions close to the wetting line. This finding contradicts the well-established Cassie-Baxter model and implies that hydrophilic top faces caused by mechanical abrasion of the surface need not induce a breakdown of superhydrophobicity as widely expected.

Wetting can also be controlled by the spatial confinement of liquids, e.g. in microfluidic devices. Herein a modified Stöber synthesis is used to coat artificial and natural fibre templates with a layer of silica. After thermal removal of the organic

template material well-defined silica channels and channel junctions with uniform diameters in the nano- and micrometer-scale are obtained. Due to their transparency, tightness and high length-to-diameter ratio the channels are highly suited to study the filling velocities of liquids with varied surface tensions and viscosities over a distance of several mm as well as very close to the channel entrance using confocal microscopy. The late stage of capillary filling can be described well by the Lucas–Washburn equation. However, the early stage is found to be slower than predicted. Whereas the previous parts of this work focus on a quasi-static wetting now the dynamics of wetting become important. Indeed, the deviations can be explained by a velocity dependent advancing contact angle and modeled with dynamic wetting theories. Thus, this work solves the widely discussed problem of the deviations from the Lucas-Washburn equation at short filling times.

Der Fokus dieser Doktorarbeit liegt auf der kontrollierten Benetzung von festen Oberflächen, die in vielen Bereichen, wie zum Beispiel in der Mikrofluidik, für Beschichtungen und in biologischen Studien von Zellen oder Bakterien, von großer Bedeutung ist.

Der erste Teil dieser Arbeit widmet sich der Frage, wie Nanorauigkeit das Benetzungsverhalten, d.h. die Kontaktwinkel und die Pinningstärke, von hydrophoben und superhydrophoben Beschichtungen beeinflusst. Hierfür wird eine neue Methode entwickelt, um eine nanoraue Silika-Beschichtung über die Gasphase auf eine superhydrophobe Oberfläche, die aus rauen Polystyrol-Silika-Kern-Schale-Partikeln besteht, aufzubringen. Es wird gezeigt, dass die Topographie und Dichte der Nanorauigkeiten bestimmt, ob sich die Superhydrophobizität verringert oder erhöht, d.h. ob sich ein Flüssigkeitstropfen im Nano-Wenzel- oder Nano-Cassie-Zustand befindet. Das verstärkte Pinning im Nano-Wenzel-Zustand beruht auf dem Eindringen von Flüssigkeitsmolekülen in die Nanoporen der Beschichtung. Im Nano-Cassie-Zustand dagegen sitzt der Tropfen auf den Nanorauigkeiten, was das Pinning vermindert. Die experimentellen Ergebnisse werden mit molekulardynamischen Simulationen in Bezug gesetzt, die den Einfluss der Oberflächenbeschichtungsdichte und der Länge von fluorinierten Silanen auf die Hydrophobizität einer Oberfläche untersuchen.

Es wurden bereits verschiedenste Techniken zur Herstellung von transparenten superhydrophoben, d.h. extrem flüssigkeitsabweisenden, Oberflächen entwickelt. Eine aktuelle Herausforderung liegt darin, Funktionalitäten einzuführen, ohne die superhydrophoben Eigenschaften einer Oberfläche zu verändern. Dies ist extrem anspruchsvoll, da funktionelle Gruppen in der Regel hydrophil sind. In dieser Arbeit wird eine innovative Methode zur Herstellung von transparenten superhydrophoben Oberflächen aus Janus-Mikrosäulen mit variierenden Dimensionen und Topographien entwickelt. Die Janus-Säulen haben hydrophobe Seitenwände und hydrophile Silika-Oberseiten, die anschließend selektiv und ohne Verlust der superhydrophoben Eigenschaften der Oberfläche funktionalisiert werden können. Diese selektive Oberflächenfunktionalisierung wird mittels konfokaler Mikroskopie und durch das chemische Anbinden von fluoreszenten Molekülen an die Säulenoberseiten sichtbar gemacht. Außerdem wird gezeigt, dass das Benetzungsverhalten durch Wechselwirkungen zwischen Flüssigkeit und Festkörper in der Nähe der Benetzungslinie bestimmt wird. Diese Beobachtung widerlegt das allgemein akzeptierte Modell von Cassie und Baxter und beinhaltet, dass hydrophile Flächen, die durch mechanischen Abrieb freigelegt werden, nicht zu einem Verlust der Superhydrophobizität führen müssen, wie allgemein angenommen.

Benetzung kann auch durch eine räumliche Beschränkung von Flüssigkeiten kontrolliert werden, z.B. in mikrofluidischen Systemen. Hier wird eine modifizierte Stöber-Synthese verwendet, um künstliche und natürliche Faser-Template mit einer Silika-Schicht zu ummanteln. Nach der thermischen Zersetzung des organischen Templat-Materials entstehen wohldefinierte Silika-Kanäle und Kanalkreuzungen mit gleichmäßigen Durchmessern im Nano- und Mikrometerbereich. Auf Grund ihrer Transparenz, mechanischen Stabilität und des großen Länge-zu-Durchmesser-Verhältnisses sind die Kanäle sehr gut geeignet, um die Füllgeschwindigkeiten von Flüssigkeiten mit variierenden Oberflächenspannungen und Viskositäten zu untersuchen. Konfokale Mikroskopie ermöglicht es hierbei, die Füllgeschwindigkeiten über eine Länge von mehreren Millimetern, sowie direkt am Kanaleingang zu messen. Das späte Füllstadium kann sehr gut mit der Lucas-Washburn-Gleichung beschrieben werden. Die anfänglichen Füllgeschwindigkeiten sind jedoch niedriger als theoretisch vorhergesagt. Wohingegen die vorhergehenden Abschnitte dieser Arbeit sich mit der quasistatischen Benetzung beschäftigen, spielt hier die Dynamik der Benetzung eine wichtige Rolle. Tatsächlich lassen sich die beobachteten Abweichungen durch einen geschwindigkeitsabhängigen Fortschreitkontaktwinkel erklären und durch dynamische Benetzungstheorien modellieren. Somit löst diese Arbeit das seit langem diskutierte Problem der Abweichungen von der Lucas-Washburn-Gleichung bei kleinen Füllgeschwindigkeiten.

1   INTRODUCTION AND MOTIVATION

This chapter gives a theoretical introduction into the wetting behaviour of liquids on solid surfaces, especially on rough surfaces. The conventional models that describe the wetting phenomena of highly water or liquid repellent surfaces i.e. the Wenzel and Cassie-Baxter models are introduced and their assumptions are discussed. These models are still widely accepted, even though their validity was doubted several times in the past. However, in this thesis it is shown experimentally that these models are insufficient to predict the wetting properties of highly liquid repellent surfaces.

Besides, this introduction presents the design parameters that are needed for the fabrication of robust superhydrophobic and superamphiphobic surfaces and gives an overview on the state of the art to fabricate superhydrophobic and superamphiphobic coatings related to the approaches developed in this work.

Also a special case of controlled wetting, the confined liquid flow in horizontal nano- and microchannels, is described as the last part of this thesis deals with the fabrication of transparent, uniform and airtight silica nano- and microchannels and their wetting behaviour with different liquids.

1.1   WETTING

Understanding the wetting phenomena of solids by liquids is essential in a myriad of biological, medical and industrial processes, ranging from the sophisticated live forms evolved on earth to artificial tissue engineering to practical applications like non-fogging coatings or self-cleaning textiles. Especially surfaces with high liquid repellency, mostly inspired by nature, have attracted high attention in the last decade.

1.1.1   WETTING ON A SMOOTH SURFACE

The wetting behaviour of an ideal flat and chemically homogeneous surface can be described with the well-known Young's equation by balancing the interfacial forces at the three-phase contact line, the so-called wetting line:[1]

$$\cos\theta = \frac{\gamma_S - \gamma_{SL}}{\gamma_L} \tag{1.1}$$

Here γ_L, γ_S and γ_{SL} are the liquid-vapour, solid-vapour and solid-liquid interfacial tensions and θ is the macroscopic contact angle that can be observed by eye or optical microscopy (Fig. 1.1). Notably, this equation implies thermodynamic equilibrium what is never the case in practical applications. Neither an ideally flat nor a chemically homogeneous surface can be prepared. For $\gamma_S = \gamma_{SL} + \gamma_L$ follows complete wetting of the surface whereas for $\gamma_S < \gamma_{SL} + \gamma_L$ a finite contact angle is formed.

Depending on the value of θ one distinguishes between hydrophilic ($\theta < 90°$, $\gamma_S > \gamma_{SL}$) and hydrophobic ($\theta > 90°$, $\gamma_S < \gamma_{SL}$) surfaces (Fig. 1.1). Whereas a drop can completely wet a substrate ($\theta = 0°$) the maximum known contact angle on a smooth homogeneous surface is about 120°-130° on trifluoromethyl group (CF$_3$)-terminated surfaces.[2],[3]
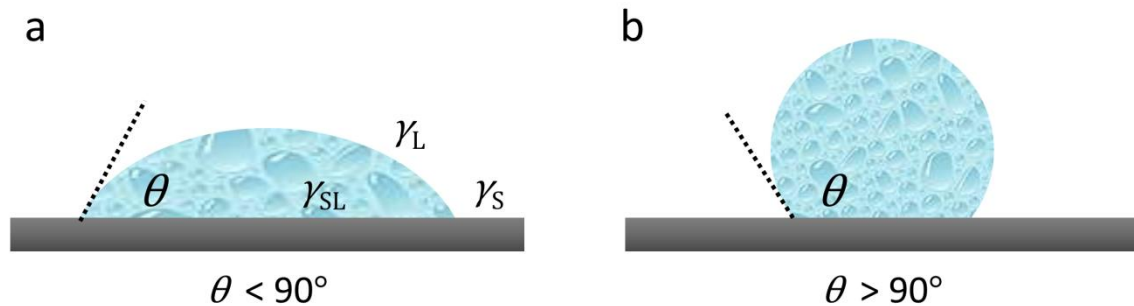
**Figure 1.1:** Contact angle θ of a sessile liquid drop on a hydrophilic (a) and on a hydrophobic (b) surface.

Young's contact angle describes wetting at the macroscopic scale, meaning 0.1-1 μm away from the wetting line. However, very close to the wetting line i.e. in a range of 1-100 nm surface forces, like van der Waals or electrostatic double-layer forces, may dominate leading to a deviating microscopic contact angle.[4]

1.1.2 WETTING ON A ROUGH SURFACE

In reality a completely smooth surface does not exist. Nano- or microscale roughness, defects, as well as chemical inhomogenities, can influence the wetting behaviour significantly. Hydrophobicity and hydrophilicity can be increased by surface roughness. Wenzel assumed complete wetting of the surface asperities (Fig. 1.2a). He developed a simple model to calculate the apparent contact angle on a rough surface θ_W by introducing a roughness factor r:[5]

$$\cos \theta_W = r \cdot \cos \theta \,, \quad r \geq 1 \tag{1.2}$$

r is defined as the total surface area divided by the projected surface area. θ is the Young's contact angle on a smooth surface with the same chemical composition. The solid surface energy can be seen as multiplied by the factor r.[6] The Wenzel equation predicts that the apparent contact angle decreases on a hydrophilic material and increases on a hydrophobic material with increasing roughness.
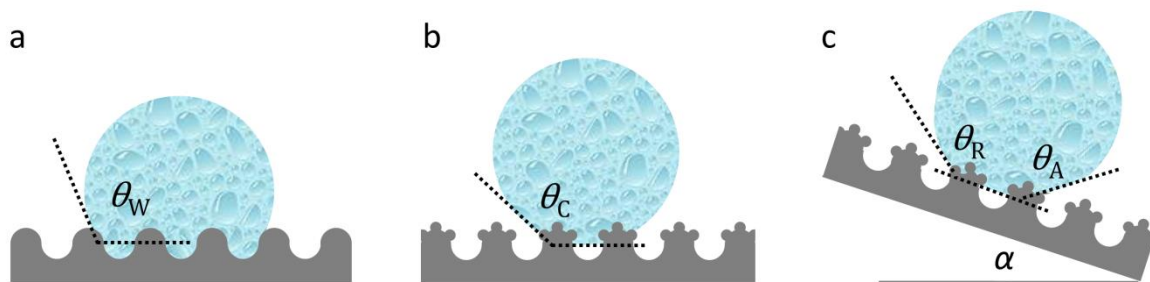
Figure 1.2: A sessile liquid drop on a rough surface resting in the fully wetted Wenzel state (a) and in the composite Cassie-Baxter state (b) respectively. By tilting a surface until the liquid drop starts to slide one obtains the roll-off angle α as well as the advancing and receding contact angles, θ_A and θ_R.

However, for surfaces that are either very hydrophobic (large θ) or very rough (large r) the Wenzel formula predicts a total drying of the surface ($\theta_W = 180°$) which is not physical due to the lack of contact between the drop and the substrate.[7] In this case it is energetically favourable that the liquid drop rests on air pockets and touches the surface only on top of the asperities leading to a composite surface (Fig. 1.2b). This composite state is referred to as Cassie-Baxter state. It is still widely assumed that the contact angle on a composite surface consisting of two materials θ_C can be calculated with the Cassie-Baxter equation:[8]

$$\cos \theta_C = f_1 \cos \theta_1 + f_2 \cos \theta_2 \qquad (1.3)$$

Here f_1 and f_2 are the fractional surface areas of the two components being in contact with the liquid drop and θ_1 and θ_2 the corresponding Young's contact angles. In the following it is shown that this equation is meaningless i.e. the contact angle derived by Equation 1.3 can vary greatly from the experimentally measured contact angle raising the question whether the wetting behaviour is dominated by interfacial energies or forces.

The adhesion properties of a drop in the Wenzel or Cassie-Baxter state differ significantly. In both cases high contact angles can be obtained. If the drop sits on air cushions in a composite state ($f_2 = f_{air}$) hardly any interactions between the liquid and the solid surface exist and the drop can be removed easily, an important property for the preparation of self-cleaning surfaces, whereas a drop in the wetted Wenzel state does not roll-off but is highly pinned.

However, the models described above predict only one contact angle for a certain surface topography and surface material, whereas experimental studies result in a wide range of possible contact angles depending on the way of deposition, the time scale and the environmental conditions. Measuring the advancing and receding contact angles is much more reliable. To obtain the advancing contact angle θ_A the volume of a liquid drop is increased until the wetting line advances. Correspondingly, to receive the receding contact angle θ_R the volume is reduced until the wetting line recedes. Alternatively, the surface can be tilted until at a certain angle, the roll-off angle α, the liquid drop starts to slide (Fig. 1.2c). Here, the larger contact angle is close to θ_A and the smaller to θ_R. The difference $\theta_A - \theta_R$ is called contact angle hysteresis. The hysteresis originates from surface roughness at the submicroscopic scale, chemical or structural inhomogenities or dissolved substances that adsorb at the three-phase contact line.[4] In case of soft polymers the high line tension can also create mechanical deformations of the surface. Roughness and surface inhomogenities cause a pinning of the contact line at certain positions leading to energy dissipative deformations of the wetting line. Microscopically the contact line looks like a random zigzag.[4],[9] Furthermore, it should be noted that even the advancing and receding contact angles are not fixed quantities. One needs to distinguish between the "quasi-static" and the dynamic angles. If the drop is in motion the contact angles depend on the velocity of the moving contact line as outlined in Chapter 6.

The effect of nanoroughness on contact angles and pinning is studied detailed in Chapter 2 of this thesis. A nanorough silica coating was added to a superhydrophobic

surface made of raspberry particles. It was found that whether superhydrophobic behaviour can be enhanced by nanoroughness depends on the structure and density of the nanoasperities. The underlying mechanism is still unclear although it is clear that if water penetrates the nanopores the droplet is pinned more strongly and the solid-liquid free energy decreases. This effect competes with an increase of the contact angles probably caused by the formation of a so-called nano-Cassie state.

1.1.3   CONTACT LINE VERSUS CONTACT AREA

In the previous paragraph the limitations of the Wenzel and Cassie-Baxter models are mentioned. Bartell, Extrand and Mc Carthy demonstrated experimentally that these models are inadequate to predict and explain contact angles.[10],[11],[12],[13] Bartell questioned the Wenzel model already in 1953.[10] He prepared paraffin surfaces of controlled roughness and observed that the measured advancing and receding angles of water or glycerol droplets were not consistent with Wenzel's theorem. Finally, he concluded that the contact angles and the resulting drop shape are determined at the solid-liquid-air interface. Extrand created chemically heterogeneous islands on smooth surfaces. He deposited small sessile droplets of water or hexadecane on the centre of an island and found that the contact angles and the hysteresis are identical to those of surfaces without islands when the rim of the drop lays beyond the island perimeter.[11] McCarthy extended this experiment and fabricated three types of surfaces, hydrophilic spots in a hydrophobic field (Fig. 1.3a), rough spots in a smooth field (Fig. 1.3b) and smooth spots in a rough field (Fig. 1.3c).[12],[13] The rough surface topography was created using photolithography (Fig. 1.3d). Analogously, the interior area didn't influence the behaviour of the contact line and the contact angles were only determined by interactions of the liquid and the solid at the contact line. McCarthy pointed out that the contact angles are defined by the activation energies that have to be overcome to move the contact line and that the contact area only dictates the ground-state energy of the contact line. However, it is unclear whether it is possible to fabricate superhydrophobic arrays of Janus pillars with hydrophobic sidewalls and hydrophilic domains on top as in this scenario the wetting line would not be in a homogeneous area as described in the experiments above but at the interface of hydrophobic and hydrophilic domains.
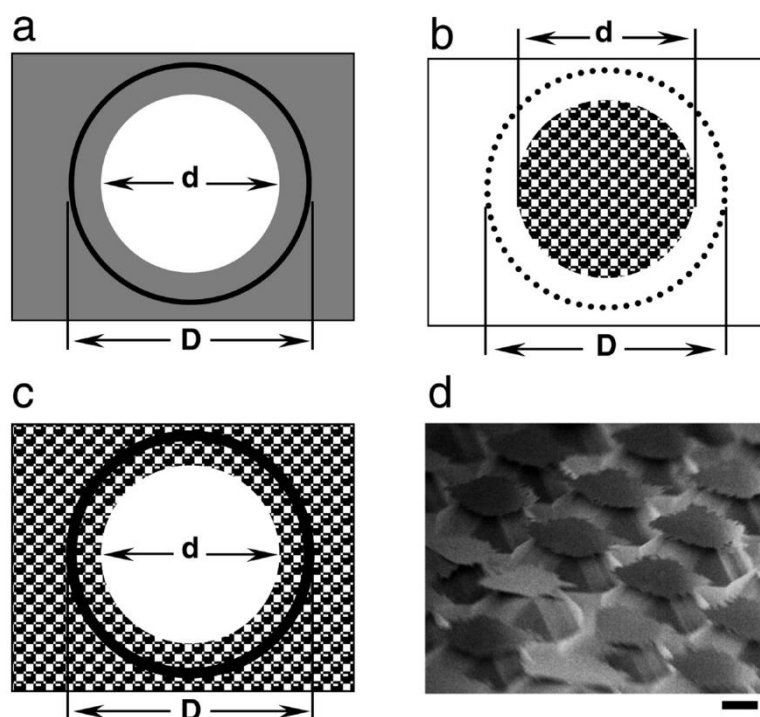
Figure 1.3: Schematic top views of surfaces consisting of hydrophilic spots in a hydrophobic field (a), of rough spots in a smooth field (b) and of smooth spots in a rough field (c). Beside of the hydrophilic spots all surfaces are hydrophobized with a semifluorinated silane. The spot size d and the contact area diameter D were varied. Scanning electron microscopy images illustrates the rough surface topography (d). The scale bar in d is 10 µm. Reprinted with permission from Gao *et al*.[13] Copyright © 2009 ACS.
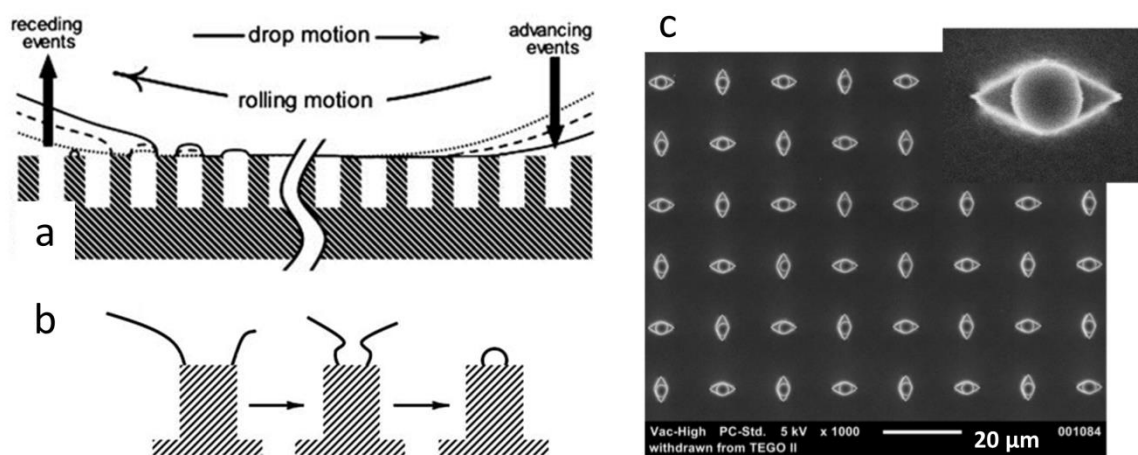
**Figure 1.4:** Sketches of a rolling drop on a surface composed of microposts showing high advancing and receding contact angles (a) and of a microcapillary bridge rupturing during a receding event (b) leading to the formation of microdrops as visualized by scanning electron microscopy using a non-volatile ionic liquid (c). Adapted with permission from Krumpfer *et al*.[14] Copyright © 2011 ACS.

The advancing and receding activation energies or energy barriers may differ significantly, especially if a drop rolls over a surface composed of micrometer-sized pillars or posts. The advancing event is not associated with an energy barrier.[15] The wetting line does not move but sections of the liquid-vapour interface come down and wet the top of the next post forming a new three-phase contact line (Fig. 1.4a). Since the apparent advancing angle is much larger than the intrinsic material advancing contact angle the top surfaces is wetted spontaneously. The receding event proceeds quite different, but no detailed experimental data monitoring the receding event on a micrometer scale exist yet. The macroscopic data suggest the following scenario: The wetting line cannot recede across the top since the apparent receding contact angle is much higher than the intrinsic one and has to detach (Fig. 1.4a). This vertical dewetting involves the rupturing of a microcapillary bridge leaving small sessile drops on the tops (Fig. 1.4b). These microdrops could be visualized recently by Krumper *et al*. using a non-volatile ionic liquid.[14] Hence, the receding activation energy is much higher than the advancing activation energy. However, the receding contact angle can be increased significantly by introducing positive curvature to the top sides, for example, by coating pillars with a monolayer of spheres as described in Chapter 5.

1.1.4   SUPERHYDROPHOBICITY

Extreme water repellency, referred to as superhydrophobicity, was first observed in nature[16] and can be observed on many plant leaves[17] like the famous lotus leaf[18] (Fig. 1.5b) or on insect wings[19] and legs[20] (Fig. 1.5a). These surfaces possess a multiscale (hierarchic) surface structure in combination with a low surface tension material. The surface of a water strider leg, for example, consists of numerous needle-shaped setae (Fig. 1.5c) with nanoscale grooves (Fig. 1.5c, inset) that enable the water strider to stand and move on water.[20] The lotus leaf surface consists of micrometer-sized papillae covered with a hydrophobic layer of wax crystals (Fig. 1.5d, inset). In particular roughness at two length scales was found to be highly efficient for extreme water repellency.[15]

A surface is usually defined as superhydrophobic if the contact angle with water is 150° and higher and the hysteresis below 10°. However, this definition is vague and different authors interpret it according to their findings. Tilting a superhydrophobic surface by a few degrees is already sufficient for a drop to overcome adhesion, to roll off easily and wash away dirt particles encountered on its way. In addition to a micro- and nanoscopic architecture of the surface a material with low surface free energy is
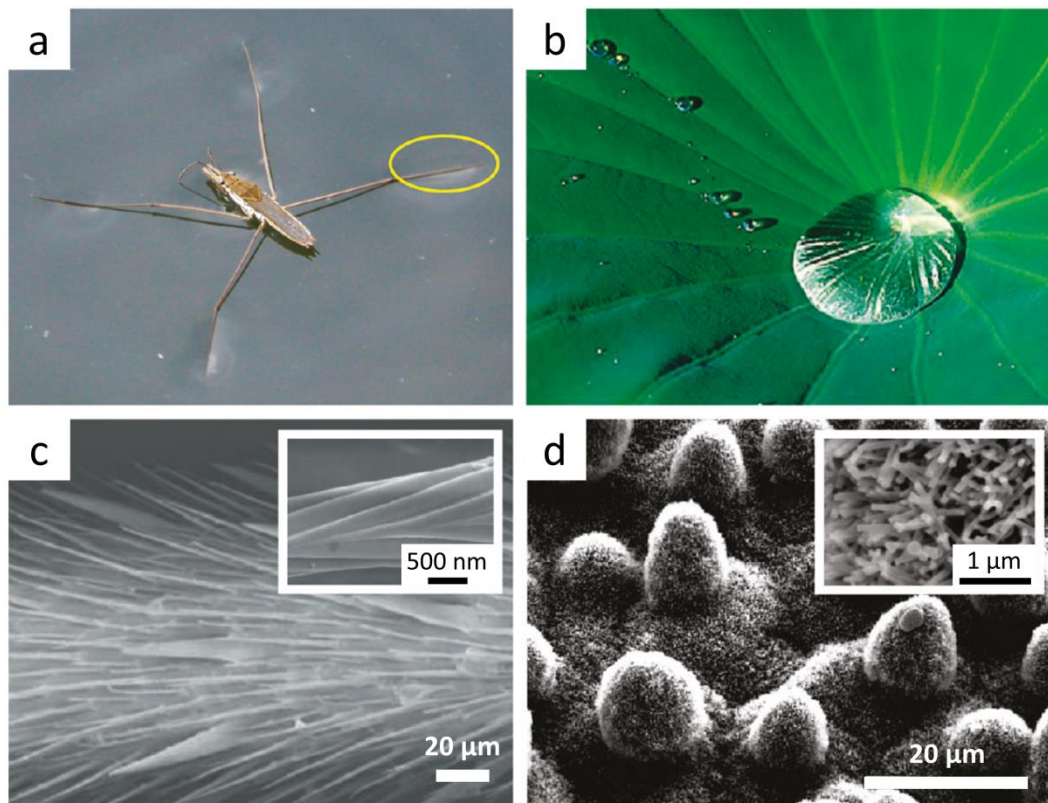
Figure 1.5: Examples for natural superhydrophobic surfaces, like the water strider leg (a) and the lotus leaf (b). Both surfaces possess a hierarchical structure on two length scales. The water strider leg surface consists of micrometer-sized sitae (c) with nanogrooves (c, inset) and the lotus leaf surface of microbumps (d) covered with nanometer-sized wax crystals (d, inset). Reprinted with permission from Su et al.[21] Copyright © 2010 ACS. The images of the water strider leg surface are reprinted by permission from Macmillan Publishers Lt: _Nature_[20], copyright © 2004. The images of the lotus leaf surface are reprinted by permission from Springer Science and Business Media[18], copyright © 1997, and by permission from Zhang et al.[22], copyright © 2006 ACS.

required. According to Young's relation it was expected that the material should possess an intrinsic contact angle of at least 90°. For example, poly(tetrafluoroethylene) with a surface free energy $\gamma_S = 18.5$ mN m^{-1} has a Young's contact angle with water of about 108°.[23]

However, superhydrophobic properties can also be observed on intrinsically weakly hydrophilic materials.[24],[25] This was predicted from Herminghaus theoretically[26] who was inspired from some superhydrophobic plant surfaces where hydrophobic wax is absent.[17] Recently, it was shown experimentally that even the wax of the lotus leaf is weakly hydrophilic with an intrinsic contact angle θ_{flat} of ~74°.[27] Cao _et al_. fabricated superhydrophobic surfaces with multiscale roughness by packing flower-like hematite particles (Fig. 1.6a). The 1-2 μm-sized α-Fe$_2$O$_3$ particles possess a rough
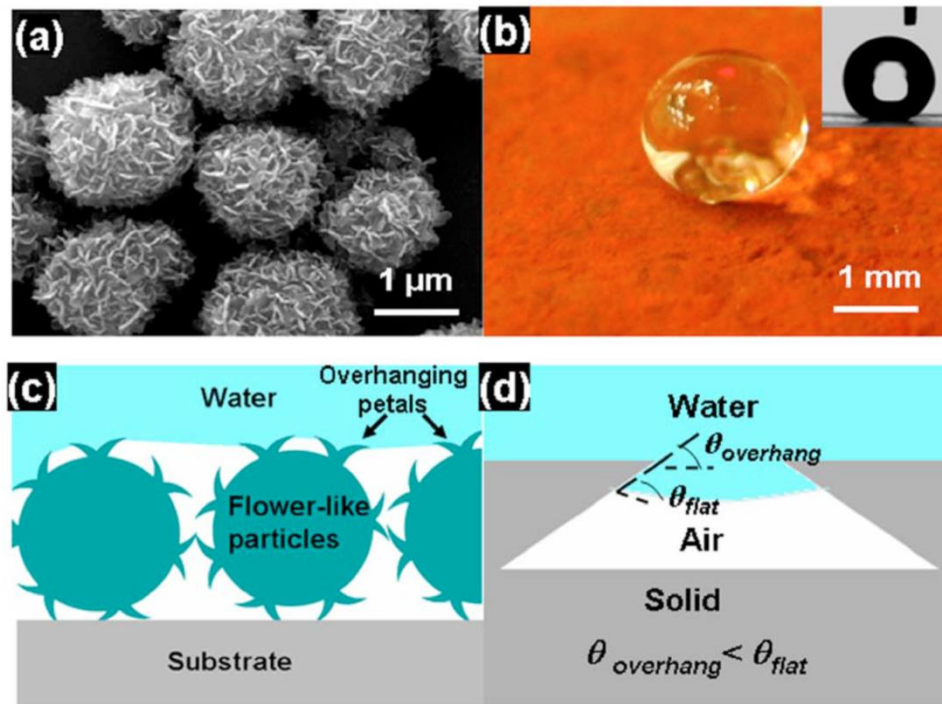
Figure 1.6: Superhydrophobic surface made of intrinsically hydrophilic hematite flower-like particles (a) showing a macroscopic contact angle with water of 159° (b). The superhydrophobic behaviour relies on the overhanging structure of the petals (c,d) that create an energy barrier for the water to penetrate into the inter-asperity spaces. Reprinted with permission from Cao *et al*.[24] Copyright © 2007 AIP Publishing LLC.

surface consisting of 40-60 nm thick distorted plates of interconnected crystals which remind to the petals of a flower. The overhanging structure of these petals (Fig. 1.6c-d) prevents the water from penetrating the textures and renders the surface superhydrophobic (Fig. 1.6b), even though a θ_{flat} of 45° for α-Fe$_2$O$_3$ predicts a complete wetting of the surface. The overhangs act as energy barrier preventing a transition from the composite to the fully wetted state. A critical parameter is here the angle θ_{overhang} formed between the sidewalls of the indent and the horizontal line (Fig. 1.6d). In the case of $\theta_{\text{overhang}} < \theta_{\text{flat}}$ the water-air interface inside the indent is convex when viewed from the water side and the capillary force hinders the water from penetrating the indent.

A transition from the composite to the wetted state can be induced, for example by an external pressure, merging of two droplets or through the vapour phase (condensation of dew, evaporation of a drop).[7] This leads to two different contact angles with different local minimum energy states and extremely different adhesion behaviour on the same rough surface depending on the way the drop is formed.[28] The stability of the composite state i.e. the value of the transition energy barrier is

highly dependent on the surface geometry. Here energy considerations predict complete wetting of the surface and interfacial forces at the wetting line have to be considered.

Also a reversible switching between a wetted Wenzel and a superhydrophobic Cassie-Baxter state could be realized experimentally by the application of electrical voltage and current (Fig. 1.7).[29] Here a Pt wire was dipped into a water drop deposited on a superhydrophobic nanostructured surface (Fig. 1.7a) to apply a potential difference between the water and the underlying substrate leading to a transition from the Cassie-Baxter to the Wenzel state, also referred to as electrowetting (Fig. 1.7b). This potential difference modifies the solid-liquid interfacial energy causing the drop to spread. After removal of the voltage the drop remained in the wetted state, even though the wetted state is no longer the minimum-energy state. To reverse this transition a short pulse of electrical current was transmitted through the substrate,
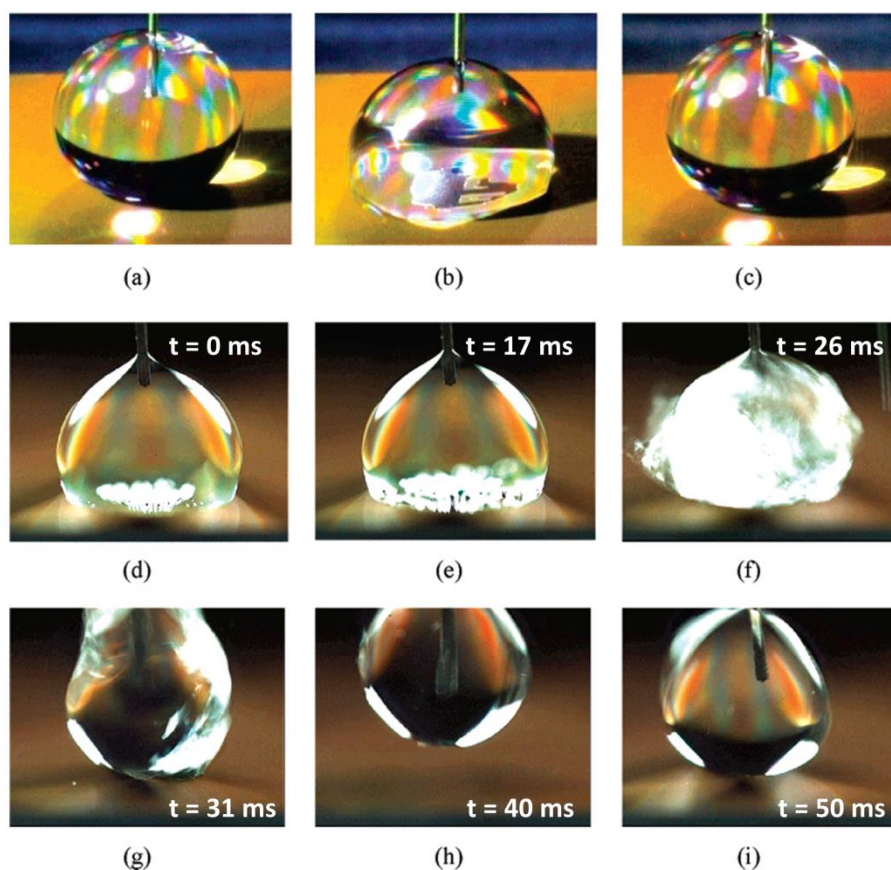
Figure 1.7: Electrically induced reversible transitions between different wetting states of a water drop on a nanostructured substrate (a - c). For better visualization of the Wenzel-to-Cassie transition a high speed camera was used (d - i). Reprinted with permission from Krupenkin *et al*.[29] Copyright © 2007 ACS.

causing a momentary increase of the surface temperature and the formation of a thin vapour layer which levitates the droplet back into the Cassie-Baxter state (Fig. 1.7c). High speed camera images made it possible to observe the air bubbles formed at the solid-liquid interface (Fig. 1.7d-i).

Verho *et al.* succeeded to switch reversibly between two Cassie-type wetting states on a superhydrophobic surface with dual-scale roughness.[30] In one wetting state the air occupied the space between microposts, referred to as micro-Cassie state, in the other state this space was mostly filled with water but air remained in the spaces of a nanorough coating leading to a so-called nano-Cassie state. The nano-Cassie-to-micro-Cassie transition has only a low kinetic barrier due to the small area fraction of the wetted solid and is therefore reversible. A transition between two Cassie states is also described in Chapter 5 of this work. In Verho's case the second scale roughness is already superhydrophobic by itself. Therefore, it was unclear whether this is a requisite to realize a nano-Cassie state. In this work it is shown that the second scale roughness only needs to favour a Cassie state.

1.1.5 SUPERAMPHIPHOBICITY

Whereas innumerable plants and many insects are known for their superhydrophobic phenomena, extremely oil repellent, so-called superamphiphobic, natural surfaces are rare. One example are the springtails that are mainly soil-dwelling wingless arthropods (Fig. 1.8A).[31] Their skin forms a stable air layer, a so-called plastron, upon immersion into water (Fig. 1.8B) or oils (Fig. 1.8C) protecting the skin breathing animals against suffocation. Scanning electron microscopy revealed that the skin of springtails is covered by a nanoscopic comb structure with hexagonally arranged cavities (Fig. 1.8D).[31] Granules are located at the intersections of the combs. A cross-sectional profile of the skin, taken by transmission electron microscopy, illustrates that the cavities possess pronounced overhangs at their top edges (Fig. 1.8E) similar to the petals of the flower-like particles described in Chapter 1.1.4.

Superamphiphobic surfaces show high contact angles ($\geq 150°$) in conjunction with low roll-off angles ($\leq 5°$ to $10°$) with water and non-polar liquids.[32],[33] To achieve an intrinsic contact angle higher than $90°$ for most alkanes with a surface tension $\gamma_L = 20\text{-}30$ mN m^{-1} a solid surface energy γ_S of less than ~ 6 mN m^{-1} is postulated.[34] This is theoretically barely fulfilled for (CF$_3$)-terminated surfaces, but experimentally not realizable. However, according to the metastable superhydrophobic phenomena on intrinsically hydrophilic surfaces metastable superamphiphobicity can be induced to

intrinsically oleophilic materials by creating local overhanging structures, also referred to as re-entrant texture.[33],[35],[36] Re-entrant means that the surface topography cannot be described by a simple univalued function $z = h(x,y)$, and a vector projected normal to the *x-y* plane intersects the texture more than once.[37]
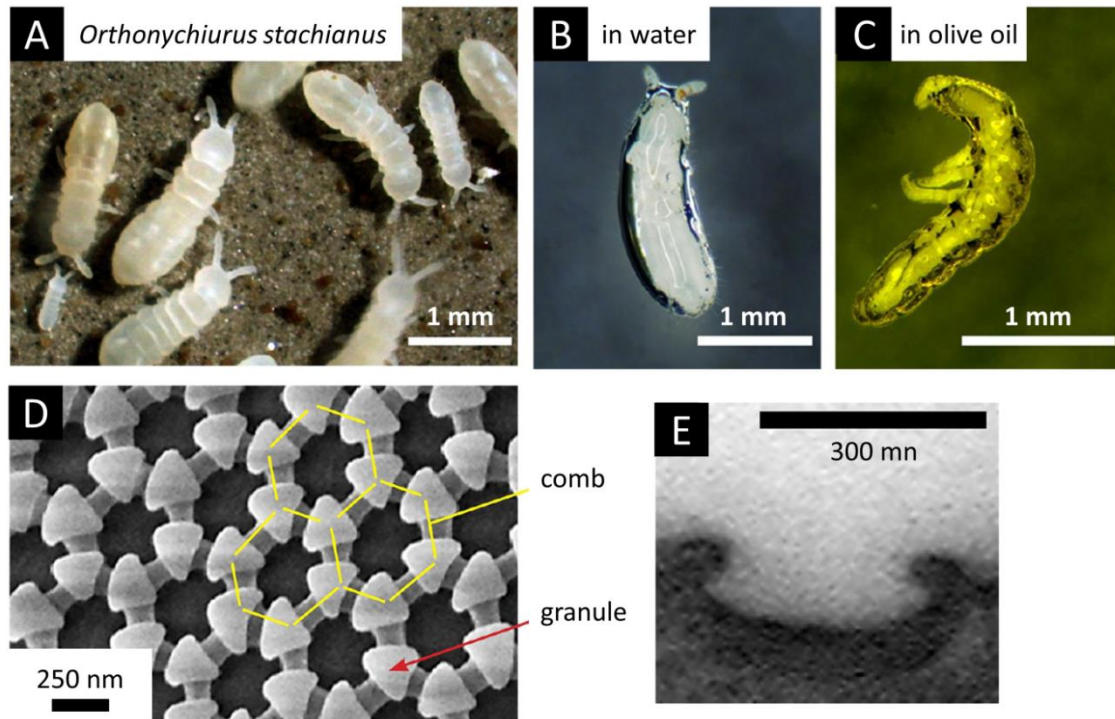
Figure 1.8 (A) Springtail colony of Orthonychiurus stachianus. (B,C) Plastron surrounding the entire animal upon immersion into (B) water and (C) olive oil. (D) Scanning electron microscopy image and (E) cross-sectional transmission electron microscopy image of the nanoscopic skin ornamentation. Reprinted with permission from Hensel *et al*.[31] Copyright © 2013 ACS.

Nosonovsky studied the stability of the composite interface of a liquid on a multirough surface with re-entrant curvature (Fig. 1.9a).[38] The surface consists of rectangular pillars of height h separated by distance b, covered with small semicircular bumps and grooves with radius R. The effect of gravity is neglected and the liquid-air (LA) interface is assumed as a horizontal plane and its position is characterized by the vertical coordinate z ($0 < z < h$). Such a surface provides many equilibrium states for the LA interface where the Young equation is satisfied leading to the Young contact angle θ_0 (Fig. 1.9a, solid and dotted lines). Nosonovsky claimed that whether an equilibrium state is stable or unstable depends on the sign on curvature of the surface as a change in $d\theta$ is equal to the change in surface slope and

that for an advancing liquid ($dA_{SL} > 0$) the equilibrium is stable if θ decreases upon advancing (Fig. 1.9a, upper dashed line):[38]

$$dA_{SL}\, d\theta < 0 \tag{1.4}$$

Hence, the convex (bumpy) surface leads to a stable LA interface, whereas a concave (groovy) surface leads to an unstable interface. Figure 1.9b shows the dependence of the interface free-energy W on the position of the LA interface z/R for the cases of hydrophobic ($\theta_0 = 150°$) and hydrophilic ($\theta_0 = 30°$) materials having the same texture as shown in Figure 1.9a. For $z/R \approx 1.5$ it is possible to form a (meta)stable composite interface on the hydrophilic surface that is energetically trapped. However, this minimum in W is no globul minimum and the fully wetted interface for $z/R \approx 4$
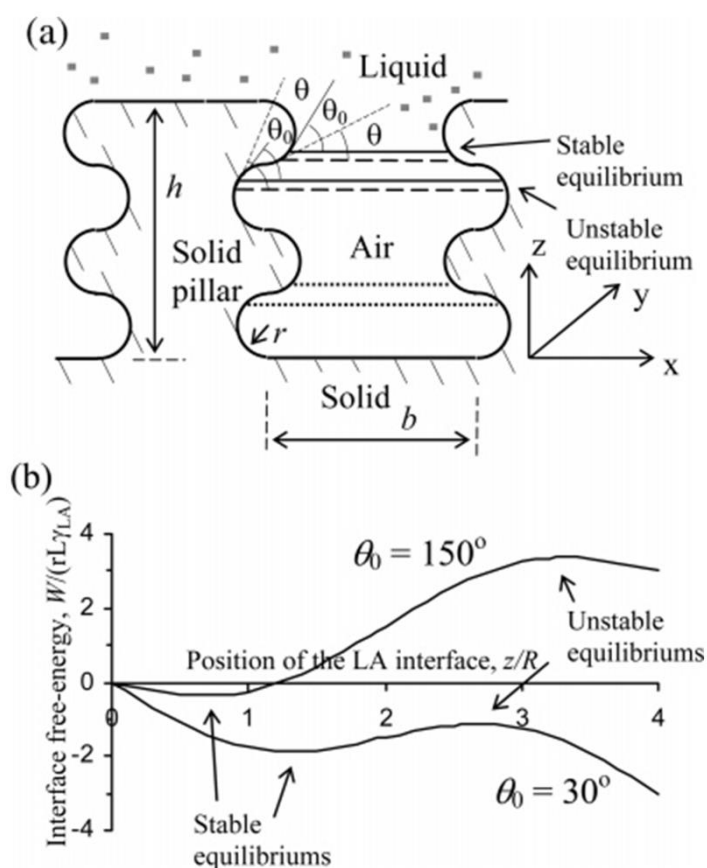
Figure 1.9: (a) Sketch of 2-dimensional pillars with semicircular bumps/grooves. The bumps may pin the contact line because an advancing LA interface results in a decrease in the contact angle ($\theta < \theta_0$). The equilibrium positions on grooves are instable because an advancing LA interface results in an increase in the contact angle ($\theta > \theta_0$). (b) Interface free-energy W as a function of the position of the LA interface z/R for a hydrophobic ($\theta_0 = 150°$) and hydrophilic ($\theta_0 = 30°$) material. Reprinted with permission from Nosonovsky *et al.*[38] Copyright © 2007 ACS.

has a lower free energy, making it to the thermodynamically favoured state. These considerations can be transferred to superamphiphobic surfaces with $\theta_0 < 90°$ for low-surface-energy liquids, such as alkanes.

Tuteja *et al*. showed that re-entrant texture alone is not sufficient for robust superamphiphobic behaviour.[37],[39] Even if Gibbs free-energy calculations predict a metastable composite interface the activation energy required for an irreversible transition to the fully wetted state might be so small that the Laplace pressure of the droplets, gravity or externally applied pressure may be enough for a sagging of the liquid-air interface.[37] They defined two dimensionless design parameters that have to be maximized simultaneously to create robust superamphiphobic surfaces. One is the spacing ratio D^* which directly determines the solid fraction f_S and therefore the apparent contact angle. For a surface of electrospun fibres (Fig. 1.10A, Fig. 1.11) they derived:

$$D^* = \frac{(R + D)}{R} \qquad (1.5)$$

R is the radius and D the edge to edge spacing of the nanofibres.

Secondly, they defined a robustness parameter H^* which measures the robustness of the metastable Cassie-Baxter state related to the liquid properties, to the material contact angle θ which can be approximated with the Young's angle and to the surface geometry. For the fibre net H^* they yielded:

$$H^* = 2 (1 - \cos \theta) \, R l_c / D^2 \qquad (1.6)$$

$l_c = (\gamma_L / \rho g)^{1/2}$ is the capillary length of the liquid. Here, varying of D and R has competing consequences on the apparent contact angle and the stability against impalement. Thus, in practice the metastable Cassie-Baxter state is not accessible with low-surface-tension liquids and the surface is fully wetted despite the re-entrant curvature.

For a superamphiphobic surface composed of micro-hoodoos (Fig. 1.10B, Fig. 1.11) the design parameters have the following form:

$$D^* = (\frac{W + D}{D})^2 \qquad (1.7)$$

$$H^* = (\frac{2[(1 - \cos \theta)R + H] \, l_{cap}}{D^2})^2 \qquad (1.8)$$
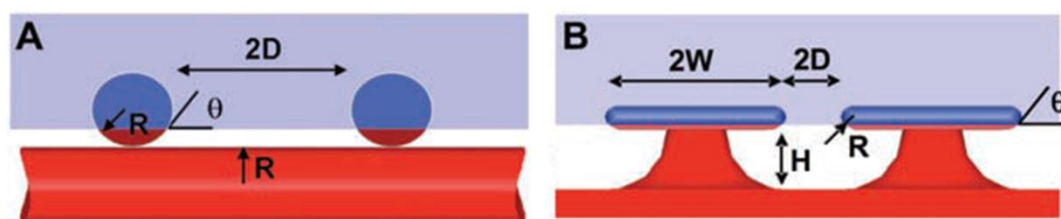
Figure 1.10: Side view of a surface of electrospun fibers (A) and of micro-hoodoos (B). From Tuteja *et al.*[33] Reprinted with permission from AAAS.
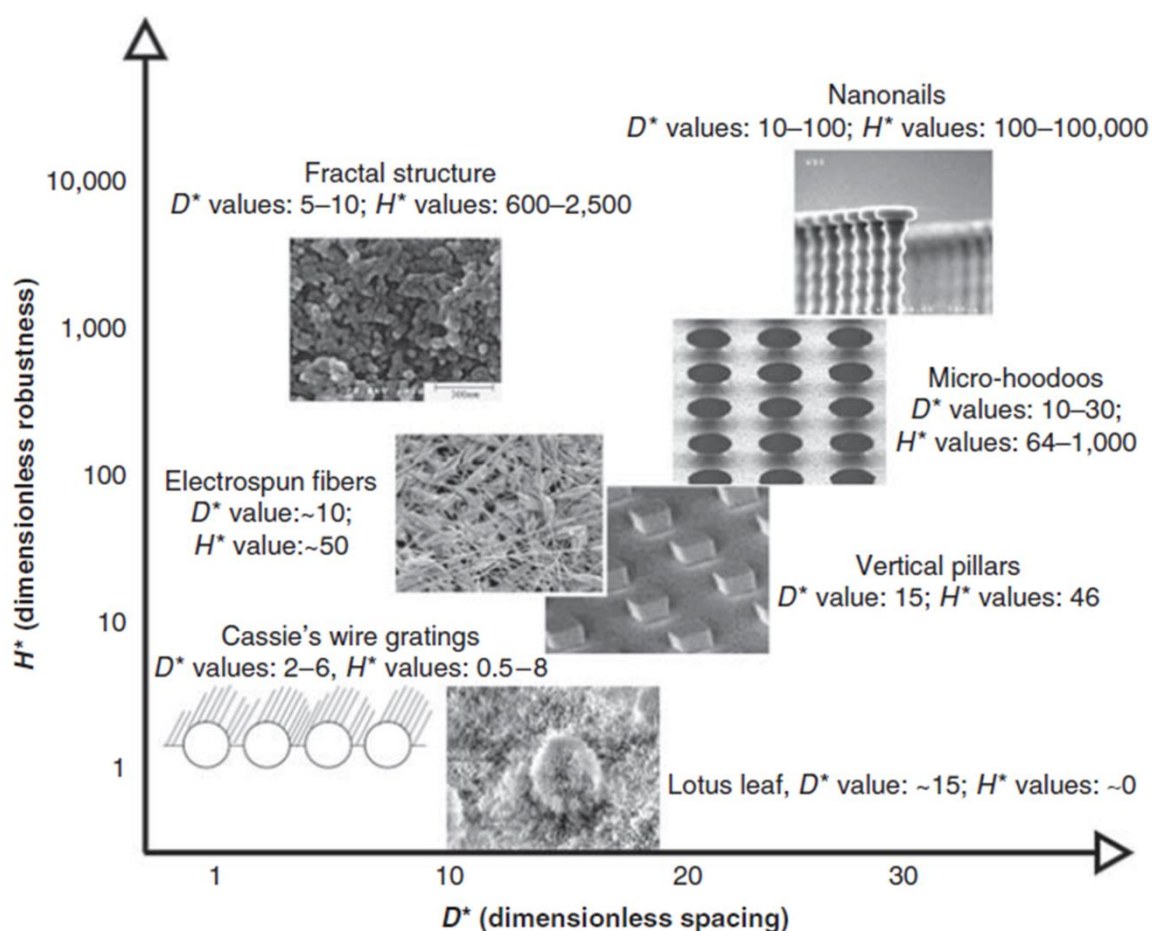
Figure 1.11: Plot of the robustness parameter H^* as a function of the spacing ratio D^* for different superhydrophobic and superamphiphobic surfaces from the literature. The plot is reproduced with permission from Tuteja *et al.*[37] Copyright © MRS 2008. The fractal structure SEM image is reproduced with permission from Tsujii et al.[40] Copyright © 1997 Wiley-VCH. The nanonail SEM image is reproduced from Ahuja *et al.*[35] Copyright © 2008 ACS. SEM Images of the electrospun fibres, micro hoodoos, and the lotus leaf are reproduced with permission from Tuteja *et al.*[33] Copyright © 2007 AAAS. The SEM image of the vertical pillars is reproduced with permission from Patankar *et al.*[41] Copyright © 2003 ACS.

One can see that the hoodoo spacing W and the hoodoo height H can be varied independently in that way that both the superamphiphobic behaviour, characterized by the apparent contact angle, and the robustness of the surface against liquid impalement is increased. However, the design parameters are insufficient to predict the height of the energy barriers.

The plot in Figure 1.11 summarizes the spacing ratios D^* and the robustness parameters H^* of octane droplets ($\gamma_L = 21.6$ mN m^{-1}) on several natural or artificial superhydrophobic or superamphiphobic surfaces described in the literature.[8],[33],[35],[40],[41] Beside of the vertical pillars all of these surfaces possess re-entrant texture. However, only the surfaces with high D^* ($D^* >> 1$) and H^* ($H^* >> 1$) values are robust superamphiphobic, like the nanonails[35] or the micro-hoodoos. Although this gives a first hint towards the stability of superamphiphobicity it is still far from being quantitative. For example, comparing the micro-hoodoos and the vertical pillars, the values for D* and H* can be close. However, vertical pillars are only superhydrophobic.

The approaches presented so far are energy-based. Butt *et al.* balanced the forces at the three-phase contact line. As many superoleophobic surfaces are composed of spherical structures they considered a convenient model system to study and predict the superamphiphobic properties of a surface.[42] This model surface consists of vertical pillars composed of spheres (Fig. 1.12). The pillars are either arranged in a square lattice or hexagonally with a lattice constant a. The spheres are all of equal radius R and partially sintered together leading to the formation of necks. The position of the neck is given by the angle β.
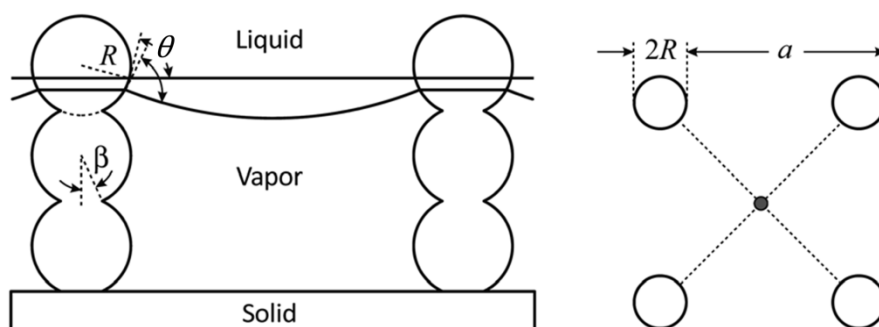
Figure 1.12: Sketch of the superamphiphobic surface consisting of spheres sintered together from side and top view. Reproduced from Butt *et al.*[42] with permission from The Royal Society of Chemistry.

There are two mechanisms for the Cassie-to-Wenzel transition induced by an applied pressure. In the first case the liquid touches the substrate due to a high curvature of the liquid-air interface, referred to as sag impalement. In the other case the contact line depins from the top sphere and moves downwards, referred to as depinning impalement. Butt demonstrated that the depinning impalement pressure is lower than the impalement pressure due to sagging and formulated an equation for the depinning impalement pressure P considering the vertical component of the capillary force of the liquid interface along the contact line:

$$P = \frac{2\pi\gamma R}{A_0} \sin^2 \frac{\theta_A}{2} \tag{1.9}$$

θ_A denotes the intrinsic material advancing contact angle and A_0 the total area per pillar with $A_0 = a^2$ for a unit cell of a square lattice and $A_0 = a^2 \sqrt{3}/2$ for hexagonally arranged pillars. This equation shows that the impalement pressure increases linearly with R/a^2.

Furthermore, by balancing the forces at the rim of a drop which is moving perpendicular to the rows of pillars the material receding contact angle θ_R could be related to the apparent receding contact angle θ_R^{app}:

$$\theta_R^{app} = \pi \left(1 - \frac{2R}{a} \cos^2 \frac{\theta_R}{2}\right) \tag{1.10}$$

This shows that for a given material receding angle the apparent receding angle only depends on the ratio a/R which should be maximized to achieve a high apparent receding angle. These results point out that for the fabrication of superamphiphobic surfaces not all parameters can be optimized at the same time. So far no model surface exists where the contact angles and wetting behaviour can be monitored on a micrometer scale.

1.1.6 FABRICATION TECHNIQUES OF SUPERHYDROPHOBIC AND SUPERAMPHIPHOBIC COATINGS

There are numerous manifold techniques to construct superhydrophobic surfaces with hierarchical structures employing various materials and substrates.[43] Here some recently developed routes are presented. An easy way to make rough surfaces on various metal surfaces is wet chemical reaction.[44],[45] Pan *et al.* fabricated interconnected $Cu(OH)_2$ nanowires on a copper plate via its immersion into a solution

of NaOH and $K_2S_2O_8$ (Fig. 1.13a).[44] Another facile method is the hydrothermal reaction.[43] Guo *et al*. fabricated superhydrophobic surfaces made of spiral Co_3O_4 nanorod arrays (Fig. 1.13b).[46] A widely-used technique to construct superhydrophobic surfaces with nano- and microscale roughness is electrochemical deposition.[47],[48] Wang *et al*. prepared in this way superhydrophobic meshes by long-chain fatty acid-induced deposition of copper microclusters (Fig. 1.13c).[48] Other employed methods include plasma etching[49],[50], chemical vapour deposition[51],[52], sol-gel method[53],[54], layer by layer assembly[55],[56] and electrospinning[57].

In this work colloidal assembly of composite particles consisting of polystyrene cores with a rough silica shell, so-called raspberry particles, is used to prepare superhydrophobic coatings with dual-scale roughness.[58],[59] After calcination these coatings can also become transparent.[60] To further enhance the superhydrophobic behaviour the particles were coated with a nanorough silica coating leading to surfaces with multiscale roughness as described in Chapter 2.
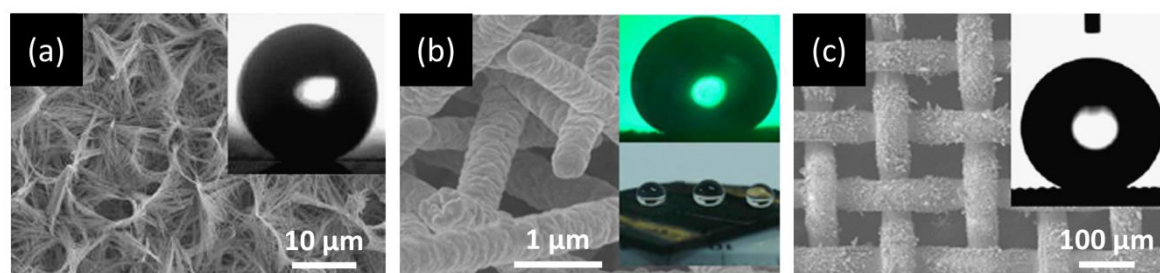
Figure 1.13: Scanning electron microscopy images of superhydrophobic surfaces fabricated by wet chemical reaction (a), hydrothermal reaction (b), electrochemical deposition (c). All surfaces show superhydrophobic behaviour after surface hydrophobization. The images are reproduced from Guo *et al*.[43] with permission from Elsevier. Copyright © 2010 Elsevier Inc. The SEM image of the interconnected $Cu(OH)_2$ nanowires (a) is reproduced with permission from Pan *et al*.[44] Copyright © IOP Publishing. All rights reserved. The SEM image of the Co_3O_4 nanorod arrays (b) is reproduced with permission from Guo *et al*.[46] Copyright © 2007 AIP Publishing LLC. The SEM image of the deposited copper mesh (c) is reproduced with permission from Wang *et al*.[48] Copyright © IOP Publishing. All rights reserved.

The fabrication of superamphiphobic surfaces is experimentally more demanding due to the complex overhang structures that are required. Strategies include spontaneous bottom-up[36],[61] like spray casting[62], lithographic top-down[33],[63] or combined approaches[34],[64]. The bottom-up approach is usually simpler, cheaper and reaches smaller sub-100 nm features.[42] In Chapter 3 of this thesis a superamphiphobic

surface is easily fabricated by coating deposited porous candle soot with silica. The soot deposit consists of spherical particles forming a fractal-like network and introducing the required re-entrant curvature.

1.1.7 CAPILLARY WETTING

So far, we focused on the quasi-static advancing and receding contact angles which are determined by tilting a plate or by adding liquid to the droplet and visualizing the moment when the drop starts to move. However, the contact angle also depends on velocity. Although this is known in general, it was unclear whether this also holds for capillary wetting. Does the velocity dependence of the contact angle change the capillary filling?

This section deals with a special case of controlled wetting, the confined liquid flow in small capillaries. The distance x penetrated by a liquid into an open horizontal cylindrical capillary of radius r due to capillary pressure can be described with the Lucas-Washburn equation:[65],[66]

$$x = c \sqrt{t}, \quad c = \sqrt{\frac{r \, \gamma_L \cos \theta_A}{2 \, \eta}} \tag{1.11}$$

η is the dynamic viscosity, θ_A the advancing contact angle of the liquid, and c is the Lucas-Washburn coefficient. This equation is based on the law of Hagen-Poiseuille that describes the volume of liquid dV transported per time interval dt assuming laminar flow and neglecting air resistance and slip:

$$\frac{dV}{dt} = \frac{\pi \, r^4 P}{8 \, \eta \, x} \tag{1.12}$$

P is the total effective pressure forcing the liquid through the capillary. As the capillary is open the atmospheric pressure is equal on both capillary ends. If no external (hydrostatic) pressure occurs the only contribution to P is the Laplace pressure $P = 2 \, \gamma_L \cos \theta_A / r$. Inserting the Laplace pressure and $dV = \pi r^2 dx$ into Equation 1.12 followed by integration one obtains the power law of the Lucas-Washburn equation (Eq. 1.11) which predicts that the penetration length x is proportional to the square root of time.

In Chapter 6 the filling velocities of liquids with varied surface tensions and viscosities in silica nano- and microchannels are measured and related to the Lucas-Washburn equation. By preparing transparent nano- and microtubes with tunable circular cross-section we are able to monitor the early stage of capillary filling by laser scanning confocal microscopy and observed deviations from the predicted $t^{1/2}$ power law to lower velocities which are explained with a velocity dependent advancing contact angle i.e. θ_A increases with increasing velocity v of the wetting line. The velocity dependent contact angle can be described with the molecular-kinetic theory and the hydrodynamic theory.[67]

The molecular-kinetic theory assumes that contact line movement results from energy-dissipative detachments and attachments of fluid molecules in the vicinity of the wetting line (Fig. 1.14a). A disturbance of the adsorption/desorption equilibria changes the local surface tensions causing a moving of the wetting line across the solid surface and a velocity dependent contact angle. The velocity of the wetting line is written as

$$v = \zeta^{-1} \gamma \left(\cos \theta_A^0 - \cos \theta_A \right) \tag{1.13}$$

with ζ is the wetting-line friction that depends on the distance between adsorption sites on the solid surface λ and the jump frequency of the molecules κ^0. θ_A^0 is the advancing contact angle for $v \rightarrow 0$.
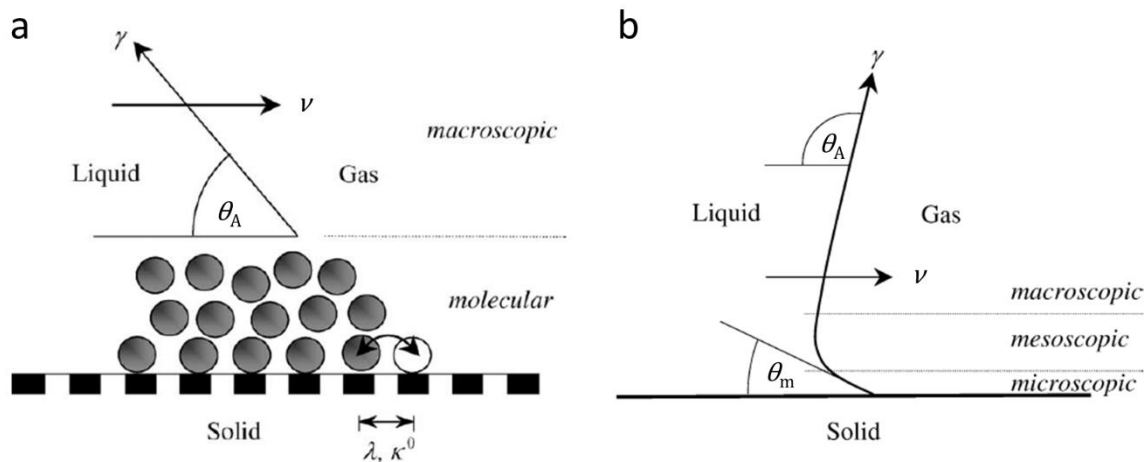
Figure 1.14: Illustration of the advancing wetting line movement in the molecular-kinetic theory (a) and hydrodynamic theory (b). Reprinted from Blake[67] with permission from Elsevier. Copyright © 2006 Elsevier Inc.

The hydrodynamic theory describes the change of the advancing contact angle due to an energy-dissipative viscous bending of the liquid-gas interface on the mesoscale close to the wetting line (Fig. 1.14b). The apparent advancing contact angle can be determined by extrapolating the static interface to the solid surface assuming that the local microscopic contact angle θ_m remains constant i.e. velocity-independent and can be written in terms of the capillary number Ca:

$$\theta_\mathrm{A}^3 - \theta_\mathrm{m}^3 = 9\,Ca\,\cdot\ln\frac{r}{L_\mathrm{m}} \tag{1.14}$$

The dimensionless capillary number correlates the velocity, dynamic viscosity and liquid-vapour surface tension: $Ca = v\eta/\gamma_\mathrm{L}$. L_m is the microscopic length and in the order of molecular size.

1.2   AIM OF THE THESIS

Despite the wide variety of studies on superhydrophobicity there are still many open questions and challenges, in particular from the fundamental side, partially due to lack of well-defined model systems and measuring techniques. As mentioned above especially hierarchical structures with dual-scale roughness were found to be very effective as highly liquid repellent i.e. self-cleaning surfaces. The first part of this thesis deals with the question whether the superhydrophobic properties can be further enhanced by introducing an additional level of roughness. Therefore dual-scale rough surfaces of assembled rough core-shell particles, referred to as raspberry particles, are coated with a nanorough silica layer leading to surfaces with multiscale roughness. The wetting behaviour is studied using liquids with varied surface tensions. It is found that the additional nanoroughness either enhances or reduces the superhydrophobic properties dependent on the size and density of the nanoasperities. Water either penetrates into the nanocavities leading to a decrease of the solid-liquid free energy and an increased contact angle hysteresis or sits on top of the nanoasperities in a so-called nano-Cassie state with reduced hysteresis.

Still it is under debate whether the wetting properties of a solid surface depend on the contact area or on the three-phase contact line formed with a liquid drop. The contact area perspective as suggested by Cassie and Baxter is still widely accepted, even though it was doubted by several researchers in the past. This issue whether the stability of the superhydrophobic state is determined by the interfacial energies or the forces at the wetting line is important for the fabrication of superhydrophobic

surfaces with hydrophilic domains. Variable techniques for the preparation of transparent superhydrophobic surfaces exist. However, for many applications, e.g. for the observation and separation of cells or bacteria, superhydrophobic surfaces with functionalities are needed. The introduction of functional groups is challenging as they are normally hydrophilic. In this work a sophisticated procedure for the fabrication of Janus micropillar arrays is presented combining photolithography and self-assembly of colloids. The Janus pillars possess hydrophobic sidewalls and hydrophilic silica tops which can be chemically post-functionalized. It is shown that the superhydrophobic behaviour remains unchanged independently on the post-functionalization by imaging the air cushions between the liquid and the substrate with confocal microscopy. This finding confirms that only solid-liquid interactions close to the wetting line determine the contact angles and that the Cassie-Baxter model is insufficient to predict wetting phenomena. Furthermore, this insight has the consequence that hydrophilic top faces caused by mechanical abrasion of the surface need not imply a breakdown of superhydrophobicity as widely expected.

Wetting can be controlled not only by surface texturing but also by spatial confinement of liquids. In the last part of this work a novel method to fabricate silica nano- and microchannels is presented using a simple template-assisted technique. Due to their transparency, tightness, high length-to-diameter ratio and well-defined diameter the channels are highly suited as models to measure the filling velocities of liquids using confocal microscopy. The capillary rise can be described with the well-known Lucas-Washburn power law. However, often deviations are observed, especially in the first stage of capillary filling. The origin of these deviations is still controversial. With the model channel system created in this work it is possible to investigate and exclude different possible origins for the initial deviations. Finally, the decrease of the initial filling velocities is attributed to a velocity dependent contact angle and modeled by dynamic wetting theories.

2   Effect of nanoroughness on highly hydrophobic and superhydrophobic coatings

Lena Mammen,[1] Xu Deng,[1,2] Maria Untch,[1] Dandapani Vijayshankar,[1] Periklis Papadopoulos,[1] Rüdiger Berger,[1] Enrico Riccardi,[3] Frédéric Leroy,[2,3] and Doris Vollmer[1]

[1] Max Planck Institute for Polymer Research,

Ackermannweg 10, D-55128, Mainz (Germany)

[2] Center of Smart Interfaces, Technische Universität Darmstadt, Petersenstrasse 32, D-64287, Darmstadt (Germany)

[3] Eduard-Zintl-Institut für Anorganische und Physikalische Chemie, Technische Universität Darmstadt, Petersenstrasse 22, D-64287, Darmstadt (Germany)

The effect of nanoroughness on contact angles and pinning is investigated experimentally and numerically for low energy surfaces. Nanoroughness is introduced by chemical vapor deposition of tetraethoxysilane and was quantified by scanning force microscopy. Addition of a root mean square roughness of 2 nm on a flat surface can increase the contact angle after fluorination by a semifluorinated silane by up to 30°. On the other hand, nanoroughness can improve or impair the liquid repellency of superhydrophobic surfaces which were made from assembled raspberry particles. Molecular dynamics simulations are performed in order to gain a microscopic understanding on how the length and the surface coating density of semifluorinated silanes influence the hydrophobicity. Solid-liquid surface

free energy computations reveal that the wetting behavior strongly depends on the density and alignment of the semifluorinated silane. At coating densities in the range of experimental values, some water molecules can penetrate between the semifluorinated chains, thus increasing the surface energy. Combining the experimental and numerical data exhibits that a roughness induced increase of the contact angle competes with increased pinning caused by penetration of liquid into nanopores or between neighboring semifluorinated molecules.

2.1   INTRODUCTION

Changing the nano- or microscopic topography of particles or substrates affects their mechanical and wetting properties. Increasing the nanoscale roughness decreases adhesion,[68] increases the viscosity of particle suspensions and allows the alignment or aggregation of particles by tuning depletion attraction.[69],[70] The wetting properties of a surface can be tuned via its roughness such that with an appropriate combination and distribution of asperities on the surface it is possible to build water repellent (superhydrophobic),[71],[72] superwetting,[73] or antifogging[74] materials. In nature, superhydrophobicity is conferred by surface roughness on the micro- and nanometer scale. Many methods are proposed for making artificial superhydrophobic surfaces, such as lithography, chemical or electrochemical deposition, or plasma etching.[19],[73],[75] Recently, Ming *et al.* showed that raspberry-like particles (short: raspberry particles) can be used to make superhydrophobic surfaces.[58],[76],[77] The term "raspberry particle" refers to the topography of their surfaces with 20-100 nm sized secondary spheres attached to a considerably larger primary particle (200 nm - 1 μm). Common to all approaches is the goal of minimizing the contact area of the droplet with the low-energy surface, since superhydrophobicity requires that water droplets roll off at tilting angles of only a few degrees.[72] However, superhydrophobicity is often impeded by the edges of the resting sites of a droplet, which can form strong pinning sites of the water-air-substrate (three-phase) contact line.[78] This increases the tilting angle and may even prevent the droplet from rolling off.[78],[79] Spherical shapes of the underlying surface lower adhesion and therefore reduce pinning strength.[80] Therefore it would be desirable to coat raspberry particles with spherical nanoasperities. Depending on the characteristic length scales water will either sit on the nano- or microasperities or completely wet them. This has been well investigated for microscopic length scales but the meaning of nanometer-sized asperities[81],[82] is less clear. If the material has a nanoporous and fibrous

structure, water can penetrate into the cavities and adhesion can rise in spite of the additional nanoroughness.

To reach a better understanding on the meaning of nanoroughness on wetting and pinning we designed a method to coat flat and rough surfaces with nanoasperities and related the results to molecular dynamic simulations. Coating raspberry particles with 5-25 nm sized chemically bonded silica nanoasperities gives rise to coatings with a roughness in three length scales, a micrometer-sized length scale set by the primary particles, a 100 nm-sized length scale set by the secondary particles, and a 5-25 nm-sized length scale set by the nanoasperities. After fluorination the hydrophobic films assembled from these particles can show lower tilting angles depending on details of the morphology. To better understand the interaction of water molecules with fluorinated molecules (perfluoroalkyldimethylsilanes) bonded to the silica surfaces, molecular dynamics simulations were performed. Especially, we computed the solid-liquid surface free energy of water in contact with a coated silica surface. To relate the molecular dynamics simulations to the experimental system the freely variable parameters were chosen to resemble the experimental system.

2.2   MATERIALS AND METHODS

MATERIALS

Styrene (99 % extra pure, stabilized) was purchased from Acros Organics and the inhibitor was removed by washing with 3 aliquots of 2 M potassium hydroxide (Sigma-Aldrich) solution and 3 aliquots of Milli-Q water. The washed styrene was distilled under reduced pressure before use. All other chemicals and solvents were used without further purification. Acrylic acid (AA) (99.5 %, stabilized), ammonium persulfate (98 %), and tetraethoxysilane (TES) (98 %) were purchased from Acros Organics, ethanol absolute from Sigma Aldrich, poly(allylamine hydrochloride) (PAH) (average molecular weight, M_w = 15,000 g/mol) from Aldrich, ammonia solution (28 % in water) from VWR International, sodium chloride (99.8 %) from Riedel-de Haën and (1H,1H,2H,2H)-perfluorodecyldimethylchlorosilane (tech. 90 %) from Alfa Aesar. Polystyrene (PS) (M_w = 66,000 g/mol, polydispersity index = 1.05) was synthesized by anionic polymerization. Milli-Q water was obtained from a Millipore purification system operating at 18.2 MΩ. Glass slides and silicon wafers used as substrates were sonicated twice in a 2 % Hellmanex II solution (Hellma GmbH), extensively rinsed with Milli-Q water and dried under nitrogen flux for at least 30 min before usage.

SYNTHESIS OF RASPBERRY PARTICLES

Polystyrene particles used as templates for raspberry particles were synthesized by soap-free emulsion polymerization of styrene with ammonium persulfate as initiator and acrylic acid as comonomer (0.8 wt% AA with respect to styrene).[58] The diameter of the spherical almost monodisperse particles was 880 nm ± 20 nm (Fig. 2.1a-d). The PS particles (0.5 g) were washed three times with fresh Milli-Q water in subsequent centrifugation steps and were resuspended in ethanol (32 mL). Subsequently, silica nanoparticles were grown on the PS surface following the Stöber synthesis,[83] resulting in hybrid silica-PS particles, so called "composite particles" (Fig. 2.1b). Thereto ammonia (2.1 mL) and TES (0.3 mL/0.5 mL) were added to the polystyrene particles suspended in ethanol. The size of the attached particles can be tuned by the amount of tetraethoxysilane and its number by the amount of acrylic acid.[58] After 1 night under stirring the attached silica hemispheres (Fig. 2.1e, light dots) reached a diameter of 113 nm ± 20 nm (Fig. 2.1e, 0.3 mL TES) or 120 nm ± 21 nm (0.5 mL TES). Likely, the silica particles attached to the surface due to the formation of hydrogen bonds between carboxyl (AA) and hydroxyl groups (silica) under the assumption that silica hardly dissociates in ethanol and that TES don't bind covalently to the carboxyl groups.[58] The surface coverage of the randomly distributed silica particles depends on the amount of AA and TES and was below 20 % for the given compositions. Subsequently the composite particles were washed with ethanol and redispersed in ethanol (24 mL). To prevent the physically attached silica particles from detaching the composite particles were coated with a thin (10-20 nm) completely closed silica layer yielding raspberry particles with a rough silica shell (Fig. 2.1c). Therefore a solution of PAH (28 mg) in water (2 mL) was added. PAH favors a homogeneous nucleation of silica on the composite surface.[58],[84] The coating with PAH was performed in a water/ethanol mixture as a partially detaching of the silica hemispheres during centrifugation in pure water was observed. After stirring for 1 h the excess of PAH was removed by centrifugation in ethanol and the particles were dispersed in fresh ethanol (37 mL). Ammonia (2.95 mL) and TES (0.39 mL/0.55 mL) were added under stirring. After 1 day the raspberry particles were washed 3 times with ethanol and were redispersed in Milli-Q water. The silica shell increased the diameter of the silica hemispheres to 140 nm ± 30 nm (Fig. 2.1f, 0.3 mL TES for the silica hemispheres and 0.39 mL TES for the silica shell) or 160 nm ± 30 nm (0.5 mL TES for the hemispheres and 0.55 mL TES for the shell) respectively.
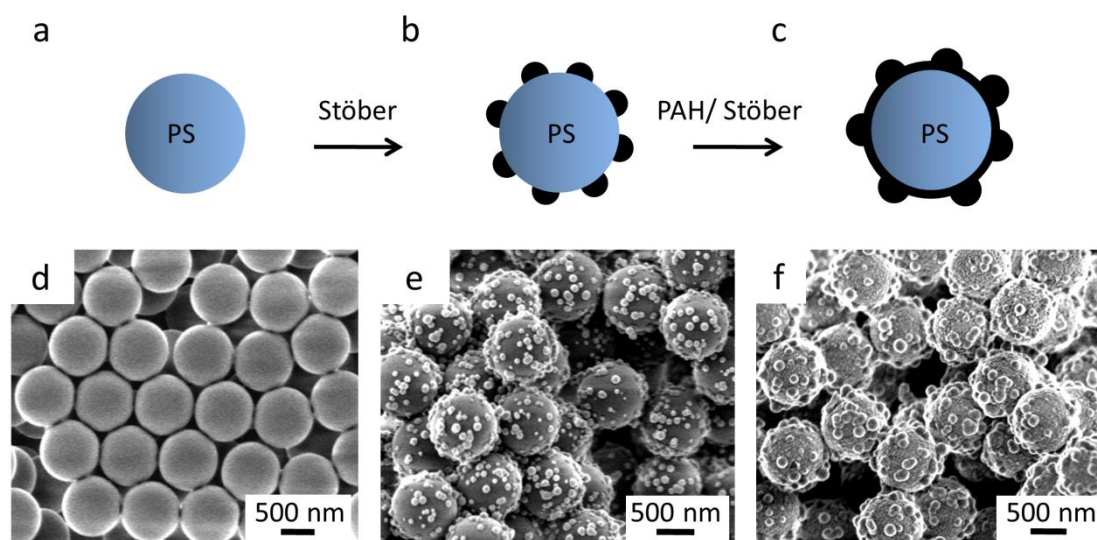
Figure 2.1: a) Sketch and d) SEM image of polystyrene (PS) particles prepared by soap-free emulsion polymerization with a diameter of 880 nm ± 20 nm. b) Sketch and e) SEM image of composite particles: PS particles covered with silica particles (white dots) with a size of 113 nm ± 20 nm. c) Sketch and f) SEM image of raspberry particles: composite particles coated with a completely closed silica shell with a thickness of about 13 nm.

PARTICLE AND SURFACE ANALYSIS

The particles and surfaces were characterized by Scanning Electron Microscopy (SEM) with a LEO 1530 Gemini (Zeiss, Oberkochen, Germany) and a Hitachi SU8000 (Hitachi High-Technologies Europe GmbH, Krefeld, Germany) at low operating voltages (0.5-1.5 kV). The diameter of the polystyrene (PS) and silica particles was obtained from SEM images averaging over 100 particles. The topography of the silica nanoasperities was determined by scanning force microscopy (SFM) in tapping-mode (Multimode Nanoscope IIIa, Veeco Metrology Group, Plainview, NY; 5500 Agilent Technologies, Santa Clara, California) at 25 °C ± 2 °C using silicon SFM probes (OMCL-AC 160TS, Olympus, Japan) with a resonance frequency of about 300 kHz and a tip radius of less than 10 nm. Contact angle measurements were performed with a contact angle meter DSA 10 (Krüss GmbH, Germany). Static contact angles were measured depositing a liquid droplet of 3 μL on the surface. For the tilting, advancing, and receding contact angles a liquid droplet of 3 μL was deposited and the stage was tilted at a speed of 1.3°/s immediately. The angle just before the drop started to move was assigned (tilting angle) and the corresponding droplet shape was used to determine the advancing and receding contact angles. Alternatively, the advancing and receding contact angles were measured by adding water to a deposited drop of 3 μL while keeping the needle inside (Table 2.1). The advancing and receding contact

angles were determined when the contact line velocity remained constant. The values given are the arithmethric means of 4-5 droplets deposited at different positions on the sample and the error is the standard deviation.

DIP COATING

Layers of irregularly distributed raspberry particles were prepared by dip coating. A cleaned glass slide (1.5 × 2.5 cm^2) was immersed into a Milli-Q water solution (10 mL) containing PAH (10 mg) and NaCl (16 mg). After 10 min the glass was washed twice by swinging in fresh Milli-Q water. Then the particle-coated glass plate was dipped into a dispersion of raspberry particles (0.6 g) in water (10 mL). After 10 min the glass was washed by swinging in Milli-Q water and dried in air. The thickness of the raspberry particle multilayer attached to the substrate decreases with the number of washing steps.

CHEMICAL VAPOR DEPOSITION (CVD) OF TES

The substrates to be covered with silica (flat silicon wafers, flat glass plates or multilayer made of raspberry particles) were placed in a desiccator together with two open vessels, one containing TES (1 mL) and the other aqueous ammonia solution (1 mL). CVD of TES was performed for 24 h at ambient temperature. In some cases the period was reduced towards 5 h, 10 h or 19 h, respectively. Thereafter, the samples were placed in a vacuum chamber (circa 1 mbar) for 2 h to remove TES or ammonia residuals.

To measure the absolute height of the silica layer the samples were treated as follow: The silicon substrates were half dipped into a PS/THF solution (5 g of PS dissolved in 20 mL of THF) for ca. 10 seconds. The substrates were dried at room temperature for one minute and placed in a desiccator together with two open vessels, one containing TES (1 mL) and the other aqueous ammonia solution (1 mL). CVD of TES was carried out for various time periods between 0 h and 48 h. Thereafter, the PS shield layer was removed by annealing at 500 °C for 3 hours in a furnace (Thermo Scientific, Germany). Only few isolated regions of silica remained on that part of the sample. The silica film thickness was determined by SFM. Line profiles across the step created by the PS shield layer were taken on 15 different regions, for each period of CVD. The error bar is the standard deviation.

HYDROPHOBIZATION OF SILICA SURFACES

CVD of (1*H*,1*H*,2*H*,2*H*)-perfluorodecyldimethylchlorosilane was done in a desiccator or closed glass vessel, respectively. The semifluorinated silane (100 µL) was put in an open glass bowl (diameter of opening: circa 2 cm) placed next to the samples (silicon wafer or raspberry particle-coated substrate). The chlorine group reacts with an ambient water molecule forming a hydroxyl group that binds covalently to the silicon/silica surface. CVD was performed for 3 days at 70 °C. To remove unreacted residuals the substrates were left in a vacuum chamber overnight. All surfaces which are characterized by contact angle measurements were chemically modified by silanization with this semifluorinated silane to decrease the surface tension of the substrate.

MOLECULAR DYNAMICS SIMULATIONS

We performed classical atomistic molecular dynamics simulations (MD) of water in contact with α-quartz surfaces coated with either (1*H*,1*H*,2*H*,2*H*)-perfluorodecyldimethylsilane (C8F) or (1*H*,1*H*,2*H*,2*H*)-perfluorooctyldimethylsilane (C6F) at different surface concentrations. Although MD simulations may be used to study the effect of nanoroughness on wetting properties, it is restricted to a level of roughness which cannot exceed a few nanometers at most. This is still below what is currently achievable experimentally. However, the knowledge of the intrinsic interfacial energy of water in contact with flat surfaces can be used to understand the wetting behavior of rough surfaces, too. Therefore, we performed simulations where the perfluoroalkyldimethylsilanes were grafted on a flat surface. We restricted our study to the water-substrate interface i.e. there is neither liquid-vapor nor solid-vapor interface present in our simulations. Thus, the results are not affected by evaporation or by changes of relative humidity that might influence experimental results. The simulations are carried out under thermodynamic equilibrium conditions, although the time-scale of the MD simulations is in the range of hundreds of picoseconds. The results characterize macroscopic systems, provided that these systems are studied under equilibrium conditions, too. Three different systems were studied: two surfaces substituted with C6F and C8F molecules at a surface concentration of 2.06 molecules/nm^2 and one surface substituted with C8F molecules at 1.32 molecules/nm^2. The simulations aimed to address the influence of the length of the perfluoroalkyldimethylsilane molecules and their coating density on the interfacial free energy between water and the related surfaces. Although the alkylsilane molecules were randomly distributed on the surface, they were approximately arranged on a square lattice due to the relatively high packing

densities and to the crystal symmetry of α-quartz. The oxygen atoms which were not bonded to a fluorinated molecule were saturated with a hydrogen atom, forming hydroxyl groups. Each simulation cell was arranged in a slab geometry with periodic boundary condition (PBC) in the direction perpendicular to the coated surfaces. Thus, each simulation cell contained in fact two interfaces between water and the coated surfaces. The quartz layer was made up of 10×8×3 unit cells (which is approximately 5.28×4.60×1.94 nm³) and was oriented such that the external surfaces corresponded to the 100 crystallographic plane of α-quartz. PBCs were used parallel to the coated surfaces so that water felt an infinite surface, though periodic. The simulations were carried out using 6100 water molecules, so that the simulation domain dimension perpendicular to the interfaces was between 10.8-11.5 nm, depending on the density and on the length of the perfluoroalkyldimethylsilanes coating molecules. This dimension was chosen large enough so that the water mass density had its bulk value beyond the layers formed by the fluorinated molecules.

No dedicated force-field exists to describe the set of intermolecular interactions of the precise systems modelled in the present work. Although we chose not to perform specific optimizations of the related interaction potential parameters, we employed force-fields that have been used to study closely related systems. The non-bonded interactions in our simulations were modeled by means of Lennard-Jones and Coulomb potentials. Water was modeled with the SPC/E (Extended Simple Point Charge) model.[85] The intramolecular interactions within the silica crystal layer were modeled following a force-field developed to study the quartz-water interface.[86] The intra- and intermolecular interaction parameters for the fluorinated molecules were the parameters of the all-atom OPLS (Optimized Potentials for Liquid Simulations) force-field.[87],[88] The potential parameters to describe the intermolecular interactions between water, silica and the fluorinated molecules were obtained using the Lorentz-Berthelot mixing rules.[89] The OPLS force-field has already been employed together with the SPC/E water model to study the interfacial properties of water in the vicinity of perfluoroeicosane crystal surfaces,[90] while the force-field to model silica has been employed to describe the interactions with polystyrene chains.[91]

A cut-off radius of 1.375 nm to compute the non-bonded interactions was used. Electrostatic interactions were computed using the reaction field method with an infinite dielectric constant such that the electrostatic forces vanished at the cut-off distance and no long-range corrections to pressure were applied. The substituted quartz layers were first equilibrated during a few picoseconds in vacuum in order to relax the system to an equilibrium state. This process was found to have a sufficient level of randomness so that the two substituted surfaces present in each simulation

cell exhibited uncorrelated configurations of the fluorinated molecules. For each of the three studied cases, two substituted layers were used. Therefore, the study was conducted on four different interfaces between water and each of the coated quartz surfaces. After the surfaces were equilibrated in vacuum, a sample of water molecules pre-equilibrated at 298 K and 1 atm was put in contact with the surfaces. An additional period of 250 ps was used to equilibrate the interfacial systems before simulations were carried out during 500 ps to accumulate data that were used for analysis.

We performed thermodynamic integration calculations implemented in the phantom-wall algorithm[92] in order to compute the solid-liquid surface free energy (solid-liquid interfacial excess free energy per unit cross section area) of the interfaces described above. Details about the phantom-wall algorithm can be found elsewhere as the method has already been used in the context of solid-liquid surface free energy computations.[92],[93],[94] For the sake of reproducibility, it should be mentioned that the force curve necessary to carry out the thermodynamic integration in the free energy computations contained 28 state points. Each of these state points was characterized by a sampling time of 500 ps.

2.3   RESULTS AND DISCUSSION

First, we investigated the influence of nanoroughness on flat substrates. Exposure of the nitrogen-dried silicon or silica substrates to tetraethoxysilane vapor in the presence of ammonia and water formed a rough silica coating which is chemically bonded to the substrate. Ammonia is supposed to catalyze the silica synthesis according to the Stöber method.[83] SEM images (Fig. 2.2a) and SFM images (Fig. 2.3) of a coated silicon substrate showed that the topography of the silica coating consists of silica nanoasperities which are irregularly distributed on the surface. The asperities resemble spherical caps although some neighboring asperities partially grew together. The diameter of the nanoasperities can be as large as 25 nm after 24 h of CVD of TES (Fig. 2.2a). To relate the height and diameter of the nanoasperities to the absolute thickness of the silica layer, the thickness was measured independently. It increases almost linearly with time (Fig. 2.2b). After 24 h the thickness is circa 30 nm, slightly higher than the maximum diameter of the nanoasperities. Within the first few hours the height of the nanoasperities (scale bars, Fig. 2.3) equalizes the thickness of the silica layer. After 10 h CVD of TES, both are close to 10 nm. For much longer periods of CVD of TES the height of the nanoasperities remains well below the
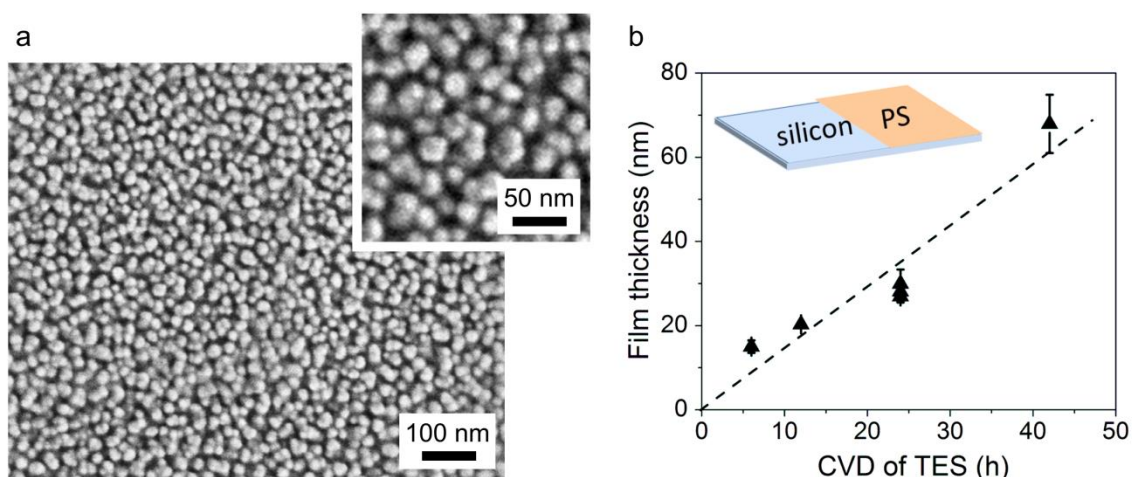
Figure 2.2: a) SEM image of a coated silicon substrate after 24 h chemical vapor deposition (CVD) of tetraethoxysilane (TES). b) Dependence of the height of the silica layer on the period of CVD of TES. Dashed line serves as a guide to the eye. Inset: sketch of a sample used to measure the film thickness. Silicon substrates were half dipped in a PS/THF solution. After removal, CVD of TES was carried out for various time periods. The PS shield layer was removed by calcination and the silica film thickness was measured by SFM.

thickness of the silica layer. This supports that first small islands form, the nanoasperities, which grow together with increasing period of CVD of TES (Volmer-Weber or Stranski–Krastanov growth).[95]

To quantify the nanoroughness of the coatings the root mean square (RMS) roughness was determined by SFM after different times of CVD on an area of 1 x 1 µm² on a coated silicon substrate (Fig. 2.3 and Table 2.1). Nucleation, growth, and coarsening of new nanoasperities cause that the roughness increases continuously. Whereas the bare silicon substrate (Fig. 2.3a) was measured to have a RMS roughness of 0.2 nm the growth of silica nanoasperities led to a RMS roughness of 1.3 nm after 10 h CVD of TES (Fig. 2.3b), of 2.2 nm after 24 h (Fig. 2.3c), and to a RMS roughness of 3.1 nm after 48 h CVD of TES (Fig. 2.3d). The measured RMS roughness is only qualitative as the depth of the valleys between neighboring particles cannot be measured owing to the finite tip size.
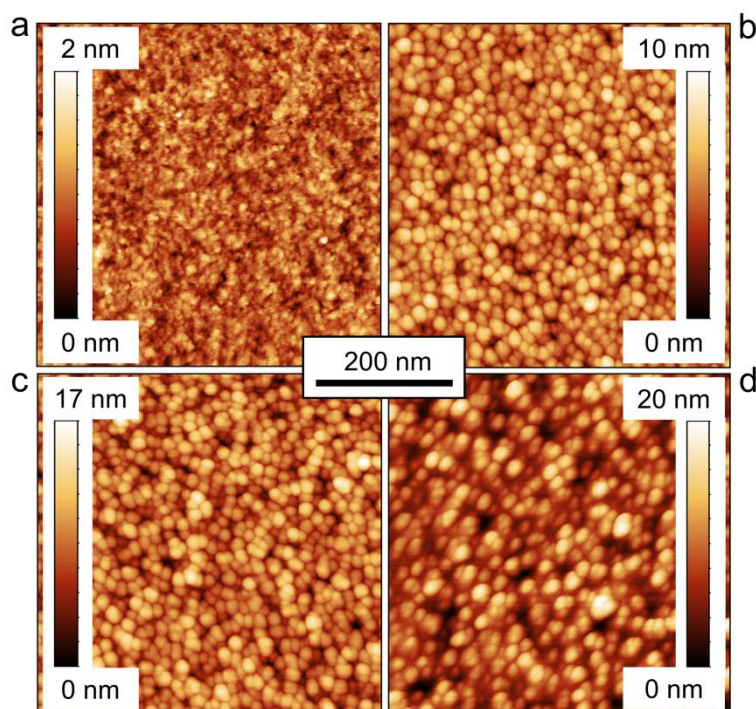
Figure 2.3: SFM images taken on (a) a bare silicon substrate, (b) after 10 h, (c) after 24 h, and (d) after 48 h CVD of TES, respectively.

Table 2.1: RMS roughness and static, advancing and receding contact angles (CA_{st}, CA_{ad} and CA_{rec} respectively) depending on the duration of CVD of TES on a silicon substrate (Experiment b). The hysteresis is the difference of the advancing and receding angle and the roughness factor r was calculated using the Wenzel equation.[5]

Time CVD of TES (h)	RMS (nm)	CA_{st}	CA_{ad}	CA_{rec}	Hysteresis	Roughness factor r
0	0.2	113° ± 1°	117° ± 1°	94° ± 2°	23°	1
10	1.3	117° ± 1°	120° ± 1°	96° ± 1°	24°	1.2
18	1.7	122° ± 1°	125° ± 1°	98° ± 2°	27°	1.4
24	2.2	143° ± 5°	149° ± 5°	113° ± 15°	36°	2.0
36	2.4	118° ± 1°	123° ± 1°	101° ± 3°	22°	1.2
48	3.1	124° ± 1°	129° ± 2°	97° ± 3°	32°	1.4

Changing the nanoroughness of a substrate affects its wetting properties. To quantify this, the static (CA_{st}), advancing (CA_{ad}), and receding contact angles (CA_{rec}) were determined after different reaction times of CVD of TES on a silicon substrate. To

decrease the surface tension of the substrates they were hydrophobized with a semifluorinated silane after the CVD process and before characterization. A monochlorosilane was applied having only one functional group (chlorine group) that can bind to the surface, forming a monolayer on top of the coating. Therefore, a monochlorosilane avoids a masking of the nanoroughness by formation of a multilayer due to crosslinking of the silane molecules. The static, advancing and receding contact angles and therefore the hydrophobicity of a substrate increased with increasing reaction time of TES until they reached a maximum value after circa 24 h CVD of TES (Table 2.1, Fig. 2.4). Then the contact angles decreased again. These measurements were repeated several times and in every case a maximum after circa 24 h CVD of TES was observed. The results of two experiments are depicted in Figure 4. The dependence of the roughness on the period of CVD of TES implies that the contact angle of a substrate can be tuned between approximately 110° and 145° by changing the reaction time of the CVD process. An increase of the static contact angle with increasing nanoroughness is proposed by Wenzel.[5] According to the Wenzel equation the contact angle of a rough compared to a smooth surface with the same chemical composition can be described as: $\cos \theta_W = r \cdot \cos \theta$.[5] θ stands for the static contact angle of the ideally flat and chemically homogeneous surface, the Young's contact angle,[1] and θ_W for the static contact angle of the nanorough surface. The roughness factor r is the ratio between the actual contact area beneath the droplet and the projected area. The different values of r were calculated using the measured static contact angles before and after different times of CVD of TES (Table 2.1). The silicon substrate was taken as flat substrate, although the silicon surface was not perfectly smooth. Corresponding to the contact angles, r increased with proceeding duration of CVD to a maximum value and decreased subsequently.

The Wenzel equation can only give a rough estimate of the contact angle of a rough substrate because it neither accounts for chemical inhomogenities nor for contact line pinning and hysteresis.[96] Pinning causes that the advancing contact angle always exceeds the static angle (Table 2.1). The difference between both, CA_{ad} - CA_{rec}, defines the contact angle hysteresis. If the surface is completely wetted by the solvent higher contact angles, i.e. increased roughness, are often accompanied by increased hysteresis.[19],[75] In line with this trend, also the hysteresis passes a maximum after 24 h CVD of TES (Table 2.1). This implies that the total contact area between water and semifluorinated silanes should pass a maximum too, or adhesion should decrease. This would imply that the total contact area decreases after 24 h of CVD of TES or tiny air pockets form. Contrary to the contact angle and the hysteresis, the RMS roughness increases continuously. Considering the RMS values, it need to be kept in mind that narrow valleys between almost touching nanoasperities cannot be resolved by SFM owing to the finite tip size (radius $\lessapprox$ 10 nm). Therefore, the RMS

values provide a lower estimate of the surface roughness. The RMS roughness does not directly correlate with the contact angles.
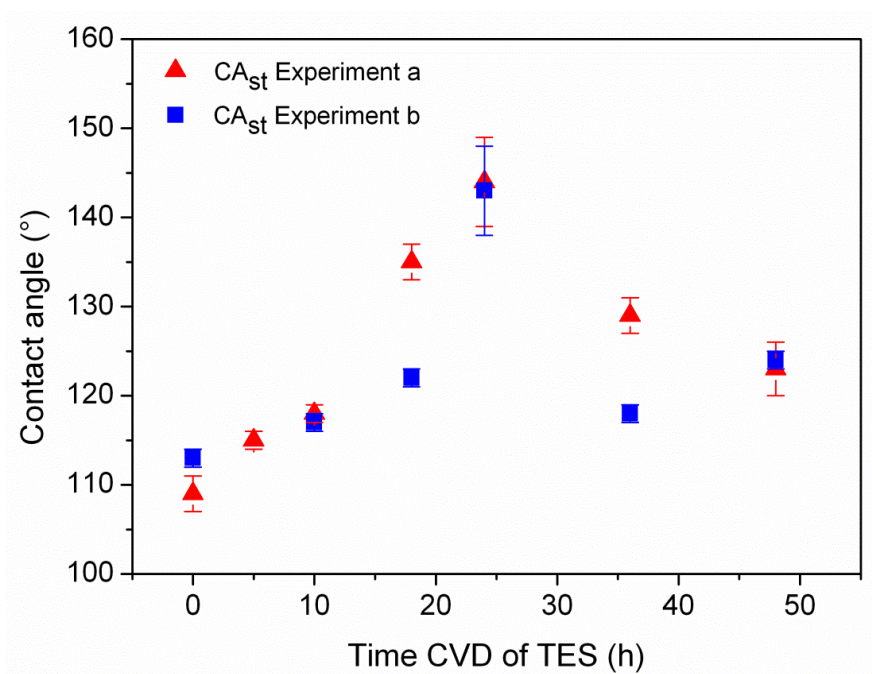

Figure 2.4: Static and advancing contact angles of water on a silicon substrate after different times of CVD of TES and hydrophobization with (1*H*,1*H*,2*H*,2*H*)-perfluorodecyldimethylchlorosilane.

This method of introducing nanoroughness can also be applied to superhydrophobic surfaces made of hybrid raspberry particles.[58],[76],[77] Layers of raspberry particles made by dip coating exhibit a roughness due to the irregular arrangement of the micrometer-sized raspberry particles (Fig. 2.6a-d) and a nanoscale roughness due to the rough silica shell of the particles (Fig. 2.5, left). Coating these films with silica in vapor phase decorated the raspberry particles with 5-25 nm sized silica nanoasperities and created particles with a roughness in three coexisting length scales, 880 nm sized PS particles, 100 nm sized silica hemispheres, 5-25 nm sized silica nanoasperities (Fig. 2.5, right, Fig. 2.6b-c,e-f). Besides, the additional silica layer improved the mechanical stability of the surface considerably by connecting neighboring particles via porous silica bridges with each other and to the substrate preventing detachment upon liquid contact.[60]

Figure 2.5: Sketch of coating raspberry particles with 5-25 nm sized silica nanoasperities making use of CVD of TES.
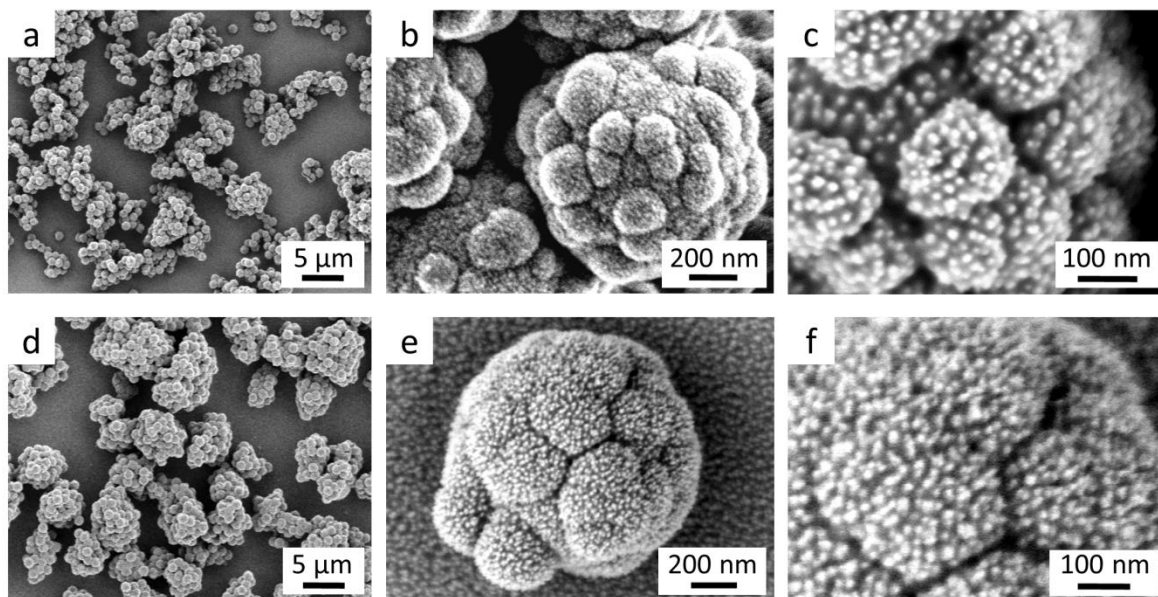
Figure 2.6: Roughness on three length scales. a), d) Roughness due to irregularly distributed micrometer-sized raspberry particles on a glass substrate, b), e) raspberry particles with rough silica shell , c), f) silica nanoasperities on top of the shell formed after 24 h CVD of TES. Images a - c show a superhydrophobic surface whose contact angles are listed in Tables 2.2-3. Images d - e show a surface with decreased tilting angle in spite of coating with silica nanoasperities by CVD of TES.

To study the effect of the nanoasperities on the superhydrophobicity of the films static, advancing, and receding contact angles (CA_{st}, CA_{ad} and CA_{rec} respectively), hysteresis and tilting angles (TA) were measured before and after chemical vapor deposition of tetraethoxysilane (Tables 2.2-3). The reaction time of the CVD process was either fixed to 10 h or to 24 h since already after 10 h of CVD of TES an increase of the contact angle was measured on flat substrates. With water droplets the static contact angles on the raspberry particle-coated films were found to be above 160° and the tilting angles below 1° for all samples independent of the deposition time of TES which means a water droplet could not be deposited onto the surface without observing it roll off immediately after removing the needle (Table 2.2). To reduce the

liquid repellency and gain more insight into the wetting properties and especially the influence of nanoasperities on contact angles diiodomethane (MI) and peanut oil, two solvents with lower surface tension (diiodomethane: γ_{MI}= 51 mN/m at 20 °C, peanut oil: γ_P = 35 mN/m at 20 °C) than water (γ_W = 72 mN/m at 20 °C), were used to decrease the contact angle according to Young's relation. In line with the decrease of the contact angles, the tilting angles increased compared to the TA of water (Tables 2.2-3). The hysteresis and tilting angles of diiodomethane decreased from originally 23° ± 1° to 15° ± 1° after 24 h CVD of TES (Table 2.3). However, no improvement of superhydrophobicity was found after 10 h chemical vapor deposition but the tilting angles even slightly increased from primary 5° ± 2° to 7° ± 2°. This might be due to the porous and fibrous structure of the silica nanoasperities which might induce penetration of liquid into nanocavities. Hence, a liquid droplet is pinned more strongly. After 24 h CVD the effect of the nanoroughness predominates over the pinning due to the porous structure. In case of peanut oil the contact angles increased significantly with increasing duration of the CVD process (Table 2.2). Whereas the film without CVD of TES was oleophilic (CA$_{st}$: 71° ± 8°) the CA$_{st}$ increased after 10 h to 125° ± 10° and after 24 h even to 145° ± 6°.[26]

However, also the morphology of the raspberry particles determines whether (super)hydrophobicity can be enhanced by chemical vapor deposition. The additional layer of the silica asperities increases the effective size of the silica hemispheres of the raspberry particles (Fig. 2.5, right). Hence, depending on the distance between the silica hemispheres on the PS-template the hemispheres may grow together, affecting the roughness of the particles. By adding more tetraethoxysilane in the first Stöber synthesis or by coating the composite particles with a thicker silica shell in the second Stöber synthesis the distance between the silica hemispheres decreases. In this case deposition of TES causes a smoothening of the raspberry particles (Fig. 2.6e-f) and the tilting angle increases. As mentioned above the structure of the deposited silica is supposed to be very loose and porous. High magnification SEM images revealed a kind of fibrous[60] or "hairy" morphology (Fig. 2.7a), providing nanocavities where solvent might penetrate. Due to the small dimensions of these cavities they cannot be maped by SFM. We suppose that they reach the Ångström range. To gain more insight into the constitution of this structure a silicon wafer which was treated with TES for 24 h was annealed to 500 °C and the RMS roughness was determined before and after annealing (Fig. 2.7b-c). The heat treatment caused a slight decrease of the RMS roughness by 10 %. This smoothing could be attributed to a compacting or densification of the silica caused by a transformation of ethoxy and silanol groups into siloxane groups through condensation reactions.[84] Additionally, it could rely on a rearrangement of the fibrous structure in order to minimize the surface energy. However, the decreased nanoscale roughness did not affect the macroscopic contact

and tilting angles within experimental accuracy (Table 2.3), likely because the decreased nanoroughness competed with a compactification of the porous material that prevented penetration of liquid into the cavities.

Table 2.2: Static contact angles (CA_{st}) and tilting angles (TA) of films made of raspberry particles measured before and after different durations of CVD of TES.

Time CVD of TES (h)	Liquid	CA_{st}	TA
0	Water	160° + 1°	< 1°
10	Water	160° + 1°	< 1°
24	Water	161° + 1°	< 1°
0	Peanut oil	71° ± 8°	> 90°
10	Peanut oil	125° ± 10°	> 90°
24	Peanut oil	145° ± 6°	> 90°

Table 2.3: Advancing contact angles CA_{ad}, receding contact angles CA_{rec}, hysteresis and tilting angles of raspberry particle-coated films measured before and after different times of CVD of TES.

Time CVD of TES (h)	Liquid	CA_{ad}	CA_{rec}	Hysteresis	TA
0	Diiodomethane	164° ± 2°	141° ± 3°	23° ± 1°	5° ± 2°
10	Diiodomethane	165° ± 1°	142° ± 2°	23° ± 1°	7° ± 2°
24	Diiodomethane	163° ± 2°	148° ± 1°	15° ± 1°	3° ± 1°
24*	Diiodomethane	160° ± 2°	146° ± 4°	14° ± 2°	3° ± 1°

Sample was annealed at 500 °C for 3 h after CVD of TES and before hydrophobization.
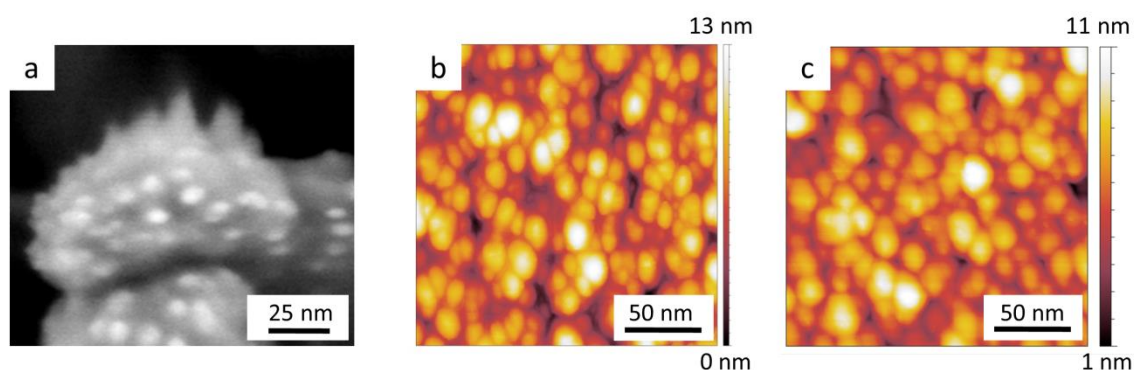
Figure 2.7: a) High resolution SEM image of a raspberry particle demonstrating the fibrous structure of the silica nanoasperities after 24 h CVD of TES (left). AFM images taken on a silicon wafer after 24 h CVD of TES (b) and after annealing the sample to 500 °C for 3h (c). CVD of TES resulted in nucleation and growth of nm-sized silica particles (RMS roughness of 2.2 nm). After annealing at 500 °C the RMS roughness decreased to 2.0 nm. The RMS roughness was determined on an area of 0.5 x 0.5 μm².

MOLECULAR DYNAMICS SIMULATIONS

MD simulations were carried out to gain microscopic insight into the role of the perfluorodimethylsilane coating molecules (C6F and C8F) regarding the surface hydrophobization process. The surface coating density of the perfluoroalkylsilanes cannot be determined experimentally. However, it affects the likeliness of penetration of liquid in nanocavities and consequently the contact angle and the contact angle hysteresis. It is therefore desirable to develop a detailed understanding of the influence of this parameter on the surface energy.

The simulations were employed to obtain the average water mass density distribution with respect to the distance to the quartz surface (Fig. 2.8). The dashed line represents the position of the upper silica atoms and indicates the approximate boundary of the quartz layer. The interval between 1 nm and 1.6-2.2 nm is occupied by the fluorinated molecules. The interface between water and the topmost fluorinated atoms is relatively sharp and the mass density of water reached its bulk value within a few ångströms. Although the water mass density distributions have a similar shape, they are shifted along the direction perpendicular to the interface depending on the length of the fluorinated molecules and on the coating density. The coating density is more important than the length of the fluorinated molecules to prevent water molecules to contact the quartz surface. On average, water molecules were located at the farthest distances from the quartz surface in the case of C8F (red

curve) and C6F (black curve) at 2.06 molecules/nm², while the shortest distances were observed in the case of C8F at 1.32 molecules/nm².
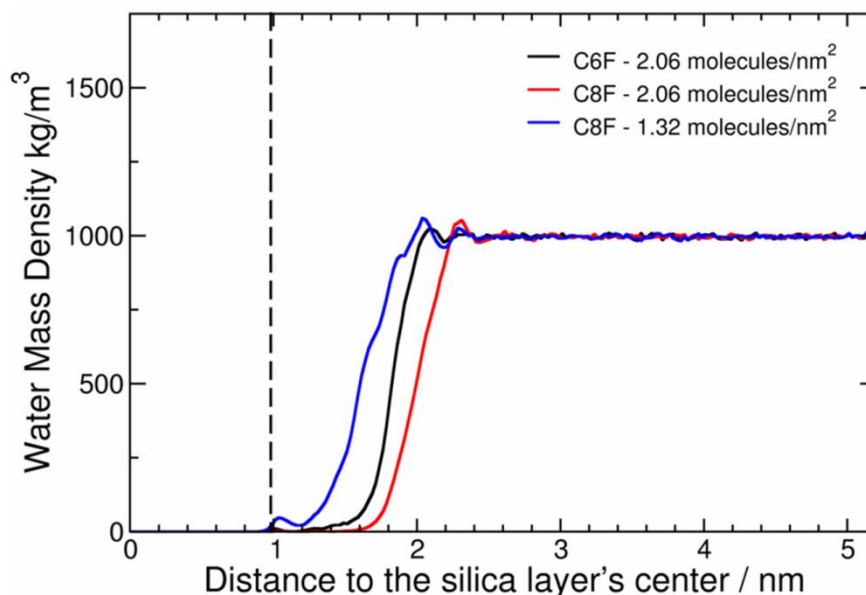
Figure 2.8: Average water mass density distribution with respect to the distance to the quartz layer center of mass. The black line corresponds to simulations with (1*H*,1*H*,2*H*,2*H*)-perfluorooctyldimethylsilane (C6F) at a surface density of 2.06 molecules/nm², the red line to simulations with (1*H*,1*H*,2*H*,2*H*)-perfluorodecyldimethylsilane (C8F) at a coating density of 2.06 molecules/nm² and the blue line to simulations with C8F at a coating density of 1.32 molecules/nm². The dashed line represents the location of the top silicon atoms of the quartz surface. A distribution was computed for each of the four interfaces at a given value of the coating density. Because all the related plots had a very similar shape, the four individual results for each of the three coated surfaces were averaged.

The probability for finding water molecules within the fluorinated layers is relatively low. However, in the case of the lowest coating density (blue curve), a slight maximum in the mass density distribution can be observed close to the quartz surface. We computed the orientation distribution of the fluorinated coating molecules in order to better understand the behavior of the water mass density distribution. The orientation of each of the fluorinated molecules is characterized by the angle between the vector joining the silicon atom and the end carbon atom of the fluorinated chain with the direction perpendicular to the quartz surface as indicated in the inset of Figure 2.9.
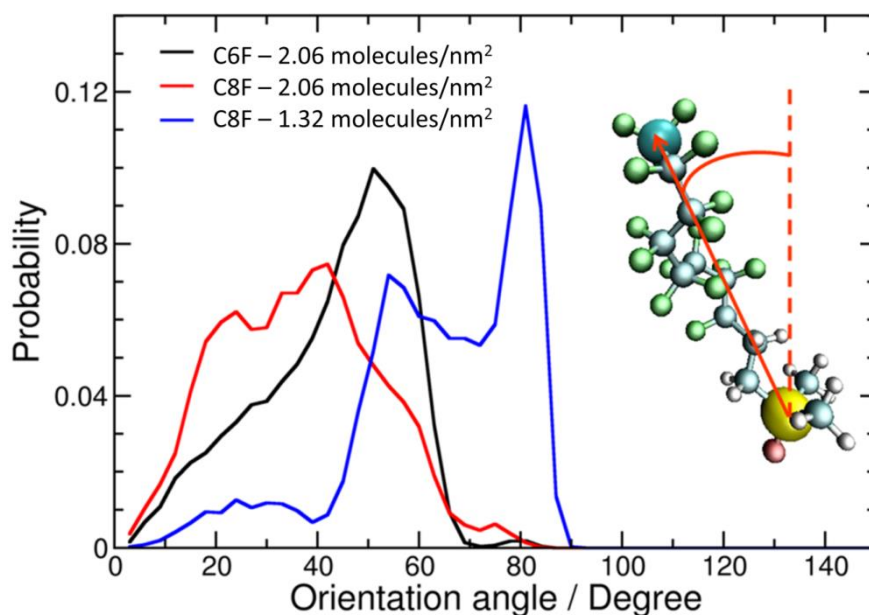
Figure 2.9: Orientation angle distribution of the angle formed by the vector between the silicon and end carbon atom of the fluorinated chain (red arrow on the right) and the direction perpendicular to the quartz surface (dashed line on the right). The red sphere represents a quartz oxygen atom to which a fluorinated coating molecule is grafted. Blue spheres stand for carbon atoms, green spheres are fluoride atoms, white spheres are hydrogen atoms and the yellow sphere represents a silicon atom. The average distributions of the orientation angles were calculated using the distribution of angles on each of the coated surfaces because the four respective distributions did not exhibit major differences in comparison with the average.

The smallest values of the orientation angle were obtained for the surface coated with C8F at 2.06 molecules/nm^2 (red curve). Because of weakened steric hindrance due to their shorter length, C6F molecules adopted orientations with a slightly larger average angle (black curve). In contrast, decreasing the coating density of C8F to 1.32 molecules/nm^2 had a major influence on the orientation of the molecules. A large proportion of C8F molecules had an orientation angle around 80 degrees and a small proportion an angle below 40 degrees (blue curve). The order of the average value of the orientation angle shown in Figure 2.9 explains the order followed by the distance of least approach of water to quartz in Figure 2.8. Moreover, the maximum of the water mass density distribution at a distance of 1-1.1 nm observed in case of C8F at 1.32 molecules/nm^2 indicates that the layer of fluorinated molecules is porous and cannot completely prevent water to directly interact with the quartz surface. This is supported by top views of two surfaces coated with C8F at both coating densities, documenting the porosity of the fluorinated layer at the lowest coating density (left) and the low orientation angles in the case of the highest coating density (right) (Fig. 2.10). At a density of 1.32 molecules/nm^2, water molecules avoid the hydrophobic

fluorinated chains. Therefore, the fluorinated chains strongly interact with the surface through electrostatic interactions between the electronegative fluorine atoms and the superficial positively charged hydrogen atoms of the silanol groups. Thus, the fluorinated molecules tend to lie on the silica surface with stretched conformations (Fig. 2.10). Such configurations are not possible for the high coating density, where steric hindrance between the fluorinated molecules prevents high orientation angles (Fig. 2.10).
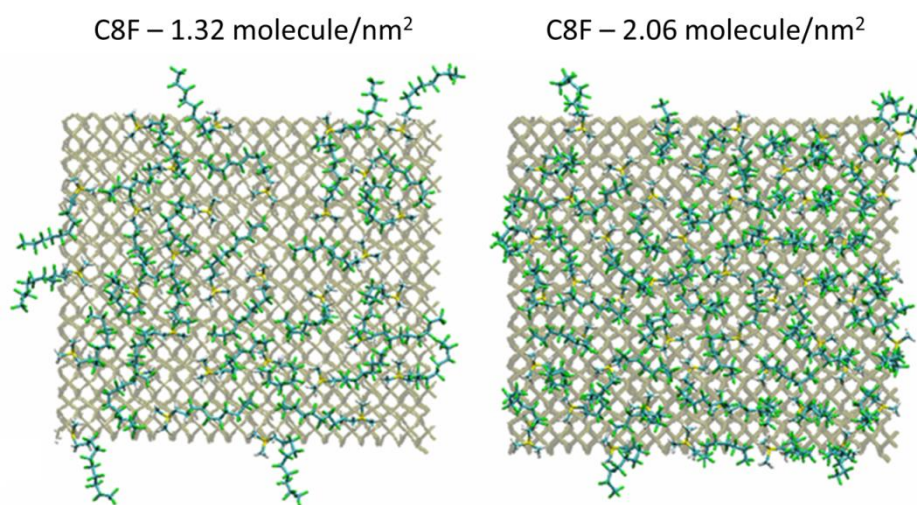
Figure 2.10: Top view of the fluorinated quartz surface for coating surface densities of 1.32 and 2.06 molecules/nm². The pictures were extracted from a snapshot where water molecules were removed for visual ease. The grey shaded structure represents the quartz structure. The green, blue, yellow and white lines represent the fluorine, carbon, silicon and hydrogen atoms from the perfluorosilanes, respectively.

In order to further characterize the interfaces between water and the hydrophobized surfaces, MD simulations were performed to compute the solid-liquid surface free energy of these interfaces by means of the phantom-wall algorithm.[92] These computations yield the difference in surface free energy γ_{SL} - γ_{ref} between the actual interface (water on fluorinated quartz) and a reference interface where water molecules interact with a planar unstructured weakly attractive surface whose surface free energy corresponds to the liquid-vapor surface tension of the water model (i.e. 59.5 mJ/m²).[94] Interfaces between water and the surfaces having identical coating densities (2.06 molecules/nm²) of C6F or C8F have similar surface free energies (Table 2.4). Increasing the density from 1.32 molecules/nm² to 2.06 molecules/nm² increased the surface free energy by approximately 30 %, indicating

that the coating density has a stronger effect on the interaction between the hydrophobized quartz surfaces and water than the length of the grafted molecules. This is in agreement with the spatial distribution of the water mass (Fig. 2.9).

Table 2.4: Thermodynamic properties of the interfaces between water and silica grafted surface with (1*H*,1*H*,2*H*,2*H*)-perfluorodecyldimethylsilane (C8F) and (1*H*,1*H*,2*H*,2*H*)-perfluorooctyldimethylsilane (C6F) at different surface coating densities.

Surface coating density	γ_{SL} - γ_{ref} (mJ/m²)	γ_{SL} (mJ/m²)
Water-C6F (2.06 molecules/nm²)	-27.8 ± 0.8	31.7 ± 0.8
Water-C8F (2.06 molecules/nm²)	-27.5 ± 0.8	32.0 ± 0.8
Water-C8F (1.32 molecules/nm²)	-34.8 ± 1.0	24.7 ± 1.0

It is reported that flat *n*-perfluoroeicosane crystalline surfaces are the lowest surface energy materials (γ_S= 6.7 mJ/m²) and yield contact angles of water droplets of 119°.[3],[97] Therefore, flat *n*-perfluoroeicosane crystalline surfaces define the lowest boundary of the surface energy and the highest possible contact angles as well as the highest γ_{SL} after coating with C8F at the largest possible surface density. Following Owens and Wendt[23] γ_{SL} can be estimated using

$$\gamma_{SL} = \gamma_S + \gamma_L - 2\sqrt{\gamma_S^d \gamma_L^d} - 2\sqrt{\gamma_S^p \gamma_L^p} \tag{2.1}$$

where γ_L is the surface free energy of the liquid and γ^d and γ^p refer to the dispersion and polar components of the surface free energies. Nishino *et al*. provided values of the surface free energies and their components mentioned above.[3] Using Equation 2.1 we obtain γ_{SL} = 42 mJ/m² in the case of the *n*-perfluoroeicosane crystalline surface. Our values of γ_{SL} are indeed below this limit. The study of Owens *et al*. provided surface free energies of PTFE which following Equation 2.1 lead to γ_{SL} = 36.3 mJ/m². It can be observed that this value compares very well with the highest values of γ_{SL} in Table 2.4. Moreover, the flat hydrophobized silica surfaces investigated in this study, showed contact angles θ of the order of 110°. This is comparable to the contact angle of water on PTFE. A good estimate of the order of magnitude of γ_{SL} is achieved by our simulations (Table 2.4). Thus, we are confident that our study captures the behavior of water in the vicinity of surface coated with perfluoroalkylsilanes at the molecular level. While considering the values of γ_{SL} and θ

in the case of PTFE and crystalline *n*-perfluoroeicosane, the contribution of γ_{SL}affect the contact angles more important than γ_S. Therefore, changes in the ratio γ_S/γ_L may be interpreted of changes of $\cos\theta$. The values of γ_{SL} in Table 2.4 show that the surface density of the perfluoroalkyldimethylsilanes has a noticeable influence on the contact angle. Indeed, the observed changes in γ_{SL} yield an increase of 5-7 degree in θ when the surface density is changed from 1.32 to 2.06 molecules/nm^2.

2.4   CONCLUSION

In summary, it can be concluded that the variations in surface free energy of water in contact with the coated quartz surfaces is more affected by the surface density of the perfluorodimethylsilanes than by the length of these molecules (provided that they are long enough). The surface density only weakly influences the structure of the fluid in the vicinity of the substrate. Nevertheless, the possibility for water molecules to probe close distances to the quartz surface when the coating density is decreased, has a strong influence on the interfacial free energy and noticeably reduces it. Such a feature preserves the hydrophobic nature of the coated surface. The observed decrease in free energy through reduction of the surface density of perfluoroalkyldimethylsilanes may represent an interpretation of the contact line pinning that is observed when insufficient coating densities are implemented. In experiments, the coating density depends on the number of binding sites for the fluorinated molecules and on the degree of nanoroughness. The number of binding sites per unit area depends on the number of silanol or ethoxy groups.[84] The influence of nanoroughness on the contact angle and contact angle hysteresis is twofold. If the surfaces are wetted by water, then nanoroughness increases the number of energetically disfavorable water-substrate contacts, causing an increase of the contact angle. Especially, if water penetrates in the pores of neighboring nanoasperities or semifluorinated molecules it increases pinning. However the likeliness for penetration also depends on the total energy balance. Therefore, if water sits on the nanoasperities nanoroughness can prevent that water penetrates between the pores, i.e. that water closely approaches the silica coating. In that case nanoroughness promotes superhydrophobicity.

2.5   ACKNOWLEDGEMENTS

3 CANDLE SOOT AS A TEMPLATE FOR A TRANSPARENT ROBUST SUPERAMPHIPHOBIC COATING

Xu Deng,[1,2] Lena Mammen,[1] Hans-Jürgen Butt,[1] and Doris Vollmer[1]

[1] Max Planck Institute for Polymer Research,

Ackermannweg 10, D-55128, Mainz (Germany)

[2] Center of Smart Interfaces, Technische Universität Darmstadt,
Petersenstrasse 32, D-64287, Darmstadt (Germany)

Coating is an essential step in adjusting the surface properties of materials. Superhydrophobic coatings with contact angles greater than 150° and roll-off angles below 10° for water have been developed, based on low energy surfaces and roughness on the nano- and micrometer scales. However, these surfaces are still wetted by organic liquids such as surfactant-based solutions, alcohols, or alkanes. Coatings that are simultaneously superhydrophobic and superoleophobic are rare. Herein, we designed an easily fabricated, mechanically resistant, transparent, long-term stable, and oil-rebounding superamphiphobic coating. A porous deposit of candle soot was coated with a 25 nm thick silica shell. The black coating became transparent after calcination at 600°C. After silanization the coating is superamphiphobic and remained so even after its top layer was damaged by sand impingement.

3.1 INTRODUCTION

A major goal in coating research is to design self-cleaning surfaces.[20],[98],[99],[100] Many surfaces in nature are superhydrophobic - for example lotus leaves.[18] Mimicking their surface morphology led to the development of a number of artificial super-hydrophobic surfaces,[15],[60] opening many applications in industrial and biological

processes.[101],[102],[103],[104],[105],[106] Microscopic pockets of air are trapped beneath the water drops.[7],[8],[26],[107] This composite interface leads to an increase in the macroscopic contact angle and a reduced contact angle hysteresis, enabling water drops to roll off easily, taking dirt with them. However, the addition of an organic liquid such as alcohol or oil, decreases the interfacial tension sufficiently to induce homogeneous wetting of the surface. Drops, initially resting on air pockets (Cassie state), pass the transition to complete wetting (Wenzel state).[8] No naturally occurring surface is known showing a contact angle θ of greater than 150° and roll-off angles below 10° for water and organic liquids. These superhydrophobic and superoleophobic surfaces are called superamphiphobic.[108]

In contrast to superhydrophobicity, the term "superamphiphobicity" is not uniquely defined in particular with respect to the liquid used.[37],[62],[109],[110] According to Young's equation, $\cos \theta = (\gamma_S - \gamma_{SL}) / \gamma_L$, the lower the surface tension the higher the tendency of a liquid to spread on a solid surface.[33],[110] Here, θ is the macroscopic contact angle, γ_S is the surface tension of the solid and γ_{SL} is the interfacial tension of the solid-liquid interface. For organic liquids ($30 \leq \gamma_L \leq 18$ mN/m) mainly van der Waals interaction act between the molecules. Therefore, $\gamma_S - \gamma_{SL}$ is positive and on planar surfaces $\theta < 90°$. Similarly, the contact angle on rough surfaces depends on the surface tensions, because roughness amplifies the wetting properties.

Furthermore, the key factors for superamphiphobicity are not clear yet. For water repellency, surface roughness and low surface energy are essential.[8] To fabricate superamphiphobic surfaces overhangs, re-entrant geometry, or convex curvature is also important.[33],[34],[35],[37],[62],[109],[110] Incomplete understanding of the importance and the complex interplay between these three key parameters – surface roughness, low surface energy and topography – has so far made it difficult and expensive to fabricate superamphiphobic surfaces. Tuteja *et al.* showed that careful design of the topography of a surface allows to construct surfaces with a contact angle for hexadecane close to 160°, although the flat surface was oleophilic.[33],[37] They explained their exceptional oil repellency by overhang structures and re-entrant geometry.

3.2 RESULTS AND DISCUSSION

Here we demonstrate a simple way to make robust, transparent, superamphiphobic coatings. The surface to be coated, in our case a glass slide, is held above a flame of a

paraffin candle (Fig. 3.1A). Deposition of a soot layer immediately turns the glass black. Scanning electron microscopy reveals that the soot consists of carbon particles with a typical diameter of 30-40 nm, forming a loose, fractal-like network (Fig. 3.1B-C).[111] A water drop gently deposited on the surface shows a contact angle above 160° and rolls off easily, proving the surface's superhydrophobicity.[6] However, the structure is fragile as the particle-particle interactions are only physical and weak. When water rolls off the surface, the drop carries soot particles with it until almost all of the soot deposit is removed and the drop undergoes a wetting transition (Movie S3.1).
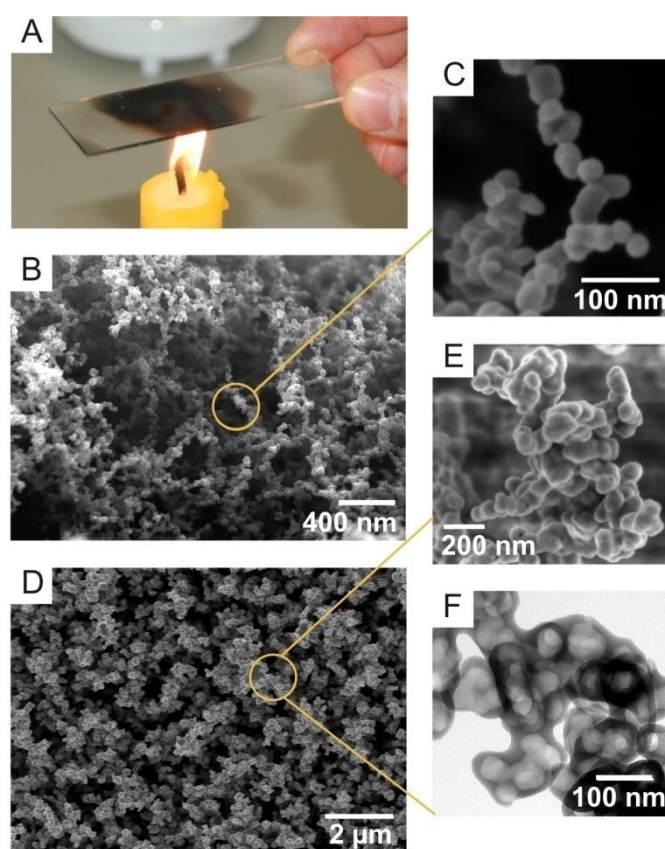
Figure 3.1: Morphology of porous structure. (A) Photograph depicting sample preparation. A glass slide is held   in the flame of a candle until a few μm thick soot layer is deposited. (B) Scanning electron microscope (SEM) image of the soot deposit. (C) High resolution SEM image showing a single particle chain made up of almost spherical carbon beads of 40±10 nm diameter. (D) SEM image of the deposit after coating with a silica shell (see Figure S3.2 for a cross section of the deposit). (E) High resolution SEM image of a cluster after removing the carbon core by heating for 2 h at 600 °C. (F) High resolution transmission electron microscopy image of a cluster after calcination, revealing the silica coating with holes that were previously filled with carbon particles. The silica shell is 20 ± 5 nm thick.

Inspired by the promising morphology of soot, we developed a technique to coat the soot layer with a silica shell making use of chemical vapor deposition (CVD) of tetraethoxysilane (TES) catalyzed by ammonia. The soot-coated substrates are placed in a desiccator together with two open glass vessels containing tetraethoxysilane (TES) and ammonia, respectively (Fig. S3.1). Similar to a Stöber reaction, silica is formed by hydrolysis and condensation of TES. The shell thickness can be tuned by the duration of CVD. After 24 h the particles are coated by a 20 ± 5 nm thick silica shell (Fig. 3.1D-E). Calcinating the hybrid carbon/silica network at 600°C for 2 h in air causes combustion of the carbon core (Fig. 3.1F) and a decrease in the shell thickness, while the layer keeps its roughness and network texture. Only isolated chains of particles, which are not linked in the network, broke during calcination (Fig. 3.1B).

To reduce the surface energy the hydrophilic silica shells were coated by a semifluorinated silane by chemical vapor deposition. After fluorination a water drop placed on top of the coating formed a static contact angle of 165° ± 1° (Fig. 3.2A), with a roll-off angle lower than 1°. Owing to the extremely low adhesion of the coating, with water it was difficult to deposit water drop, because they immediately tended to roll off (Movie S3.2). When drops of organic liquid were deposited, the static contact angles ranged from 154° for tetradecane up to 162° for diiodomethane, (Fig. 3.2B, Table 3.1, and Fig. S3.3). The maximal roll-off angle was only 5°, even for tetradecane with a surface tension of 26 mN/m.
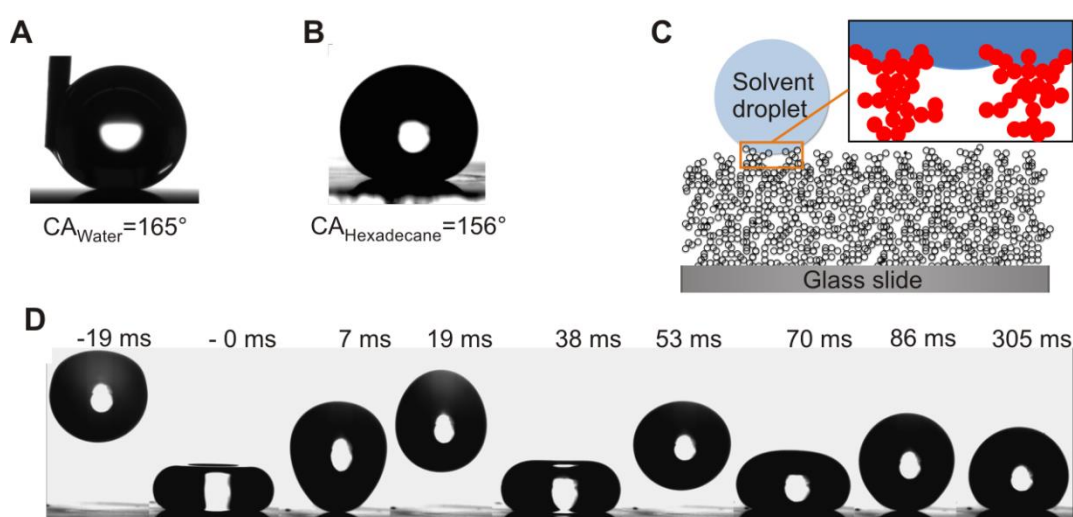
Figure 3.2: Superamphiphobicity of the surface. A 2 μL water drop (A) and 5 μL hexadecane drop (B) deposited on the surface possess a static contact angle of 165°±1° and 156° ± 1°, respectively. (C) Cartoon of a liquid drop deposited on the fractal-like composite interface. (D) Time resolved bouncing of a 5 μL hexadecane drop on a superamphiphobic surface. Just before impinging the drop's kinetic energy exceeds its interfacial energy by 2.4 i.e. the Weber number is 2.4.[112]

Table 3.1: Comparison of the static contact angle (SCA) and roll-off angle of drops with different surface tension, deposited on a flat fluorinated glass substrate and on a superamphiphobic coating.

| Liquid	Surface tension (mN/m)	Flat surface SCA	Superamphiphobic surface SCA	Roll-off angle
Water	72.1	108° ± 1°	165° ± 1°	1° ± 1°
Diiodomethane	50.9	91° ± 1°	161° ± 1°	2° ± 1°
Ethylene glycol	47.3	89° ± 1°	160° ± 1°	2° ± 1°
Peanut oil	34.5	70° ± 1°	158° ± 1°	4° ± 1°
Olive oil	32.0	69° ± 1°	157° ± 1°	4° ± 1°
Hexadecane	27.5	64° ± 1°	156° ± 1°	5° ± 1°
Tetradecane	26.5	54° ± 1°	154° ± 1°	5° ± 1°

Hexadecane drops impinging with a velocity of up to at least v = 1 m/s did not penetrate into the layer. The drop's kinetic energy was transformed into vibrational energy allowing the drop to rebound twice, before it underwent damped oscillations and finally rested on the surface in the Cassie state (Figs. 3.2D and S3.4-5, Table S3.1).[39],[112],[113] The coating retained its superamphiphobicity even after impinging of at least thousands of water drops (Fig. S3.6) or flushing the coating with water for several hours. Its self-cleaning properties for water and alkane were verified by depositing drops of either liquid on a superamphiphobic layer and monitoring the taking up of contaminants (Fig. S3.7).

For applications on glass surfaces such as goggles, touch screens, or difficult-to-access windows, the superamphiphobic coating needs to be thermally stable, transparent, and mechanically robust. To quantify the thermal stability, the coatings were annealed at temperatures up to 450°C for 1 h. The static contact and roll-off angle remained constant up to 400°C (Fig. 3.3A). Annealing at even higher temperatures decomposed the fluorosilane. The silica network remained almost unaltered until annealing up to 1000°C (Fig. S3.8). Annealed coatings can recover their superamphiphobicity after repeating CVD of a fluorosilane. After calcinations of the black carbon template the silica network has a shell thickness well below the wavelength of light. Such thin shells are highly transparent, as verified by UV-VIS (Fig. 3.3B). The transmittance of a 3 µm thick coating is reduced by less than 10 % compared to pristine glass for a wavelength above 500 nm. This transparency is reflected in the easy readability of the letters underneath the coated glass plate and

its superamphiphobicity is depicted in the high contact angle for a wide variety of liquid drops (Fig. 3.3C).
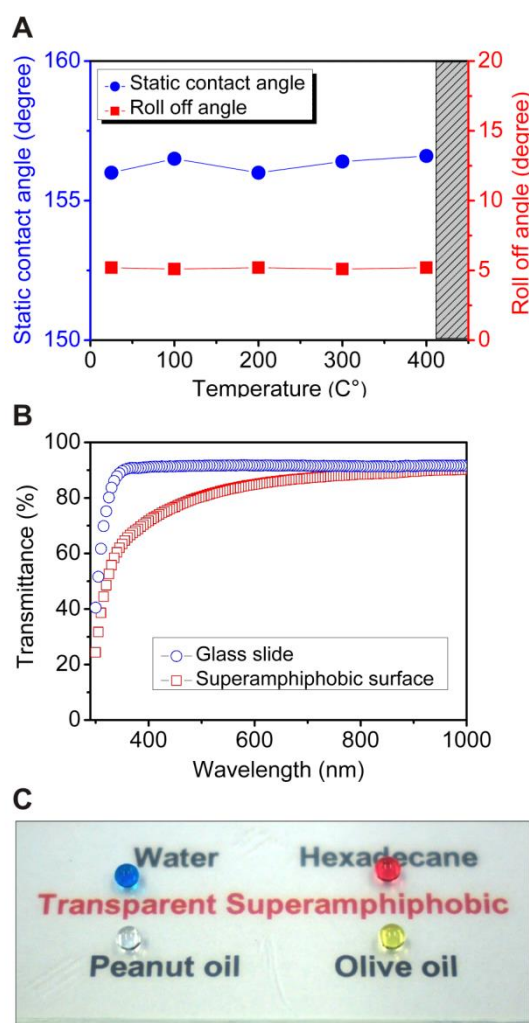
Figure 3.3: Thermal stability and light transmittance of a superamphiphobic surface. (A) Static contact and roll-off angle of hexadecane measured after annealing the samples for 1 h at various temperatures. The surface loses its superamphiphobicity after annealing at temperatures above 400 °C due to thermal degradation of the fluorosilane (shadow area). (B) UV-Vis transmittance spectra of a 3 μm thick superamphiphobic surface compared to pristine glass. (C) Photograph of dyed water (γ_L = 72.1 mN/m; blue), peanut oil (γ_L = 34.5 mN/m; white), olive oil (γ_L = 32.0 mN/m; yellow), and dyed hexadecane drop (γ_L = 27.5 mN/m; red) deposited on a superamphiphobic glass slide. The coated slide was placed on labeled paper.
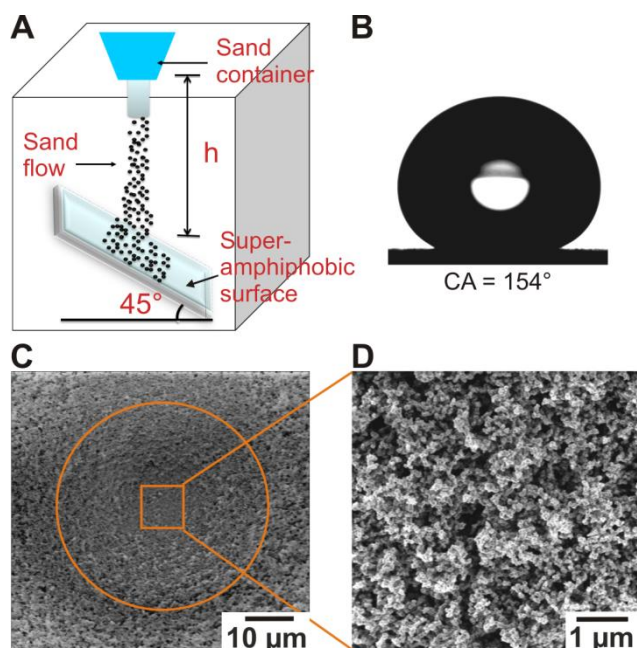
Figure 3.4: Mechanical resistant quantified by sand abrasion. (A) Schematic drawing of a sand abrasion experiments. (B) Hexadecane drop deposited on the coating after 20 g sand abrasion from 40 cm height. The 100 to 300 μm sized grains have a velocity of 11 km/h just before impingement. After impingement drops rolls off after tilting the substrate by 5°. (C) SEM image of a spherical crater (orange circle) after sand abrasion. (D) SEM image of the surface topography inside the cavity.

In outdoor applications superamphiphobic surfaces need to survive harsh conditions. To investigate the mechanical resistance, water drop impacting and sand abrasion tests were performed.[114] Sand grains, 100 to 300 μm in diameter impinged the surface from a height of 10 ~ 40 cm, corresponding to an impinging energy of 1-90×10^{-8} J per grain (Fig. 3.4A). The silica shells are not sufficiently robust to completely sustain sand impact. A cave formed underneath the impacting area (Fig. 3.4C). However, zooming into the cave revealed an almost unaltered sub-micrometer morphology (Fig. 3.4D). Owing to the coating's self-similarity, the surface kept its superamphiphobicity until the layer was removed after extended impact. The mechanical durability depends on the amount of sand impinging per unit of time and area, the size of the grains, the height of fall, and the thickness of the silica shell. The mechanical stability increases with the thickness of the silica shell, but at the expense of the coating's transparency.[114] The surface kept its superamphiphobicity for 5 min sand abrasion from a height of 25 cm (2 m/s). (Movie S3.3).

The presented coating is built of a fractal-like assembly of nano-spheres. With increasing duration of CVD of TES or annealing above 1100°C the necks between particles fill with silica and more rod-like shapes evolve, which reduces the

superamphiphobicity (Fig. S3.8, Fig. S3.10). This can be understood from Nosonovsky's prediction that convex small-scale roughness can provide a sufficient energy barrier against wetting,[38],[110] thus rendering superamphiphobicity possible. A spherical shape should provide a higher energy barrier against wetting than a rod-like shape (Fig. S3.8, Fig. S3.10).

3.3   CONCLUSION

Our easy to fabricate oil and water repellent coating is made from soot encased by a silica shell. The coating is sufficiently oil repellent to cause rebounding of impacting drops of hexadecane. Even low surface tension drops of tetradecane roll off easily when tilting the surface by 5°, taking impurities along. The surface keeps its superamphiphobicity after annealing at 400 °C. The coating is transparent and can be applied to a variety of heat resistant surfaces, such as aluminum, copper, or stainless steel.

3.4   ACKNOWLEDGEMENTS

3.5   SUPPLEMENTARY INFORMATION

### MATERIALS AND METHODS

MATERIALS

Tetraethoxysilane (TES) (Acros Organics, 98 %), ammonia (VWR, 28 %), (1H,1H,2H,2H)-perfluorooctyltrichlorosilane (Sigma Aldrich, 97 %), Milli-Q water, diiodomethane, ethylene glycol, penaut oil (commercial), olive oil (commercial), hexadecane and tetradecane were used without further purification.

CHARACTERIZATION

The morphology of the soot particles and the coating were characterized by Scanning Electron Microscopy (low voltage LEO 1530 Gemini, Germany, and SU8000, Hitachi, Japan). The samples were prepared on a silicon wafer and investigated without further treatment. After calcination the hollow silica networks were imaged by Transmission Electron Microscopy (FEI, 200 kV). Static, advancing, receding, and roll-off angles were measured with a contact angle meter, Dataphysics OCA35 (Data Physics Instruments GmbH, Germany). Transmission was measured using an ultraviolet-visible spectrometer (Lambda 900, Perkin Elmer) in double-beam mode, using an uncovered glass slide as a reference. High speed movies were taken with a high speed camera (Photron, Fastcam SA1).

METHODS

Chemical vapor deposition of TES: The soot-coated substrates (glass or silicon) were placed in a desiccator together with two open glass vessels containing about 2 mL of tetraethoxysilane (TES) and aqueous ammonia solution, respectively (Fig. S3.1). The desiccator was closed again and chemical vapor deposition (CVD) of TES was carried out for 24 h, if not stated otherwise. Similar to a Stöber reaction[83] silica is formed by hydrolysis and condensation of TES catalyzed by ammonia.[60]
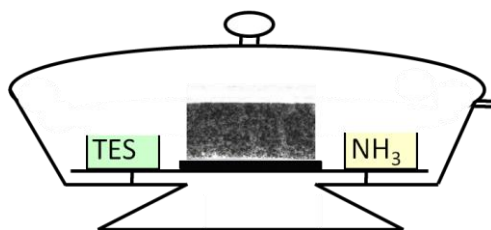

Figure S3.1: Sketch of a desiccator together with the soot-coated substrate (middle) and two glass vessels, containing tetraethoxysilane (TES) and ammonia solution (NH$_3$), respectively.

Silica shells prepared by the Stöber reaction are nano-porous. During calcination, carbon (generally a polymer) cores thermally degrade and carbon dioxide diffuses through the silica shell.[84],[115],[116] After calcination of the fractal-like carbon/silica network at 600°C for 2 h in air, the hydrophilic silica coating is hollow. To transform it into a superamphiphobic coating chemical vapor deposition (CVD) of a

semifluorinated silane on the films was performed. Therefore, the coated substrate and an open glass vessel containing about 0.1 mL of silane were put in a desiccator for 3 h. To increase the vapor pressure of silane the desiccator was evacuated for a few minutes. Afterwards the vessel containing the silane was removed from the desiccator and vacuum was applied for one hour to remove unreacted silane residues.

The thickness of the coating increases with the amount of deposited soot. The average soot density is independent of height, i.e. the porous layer is uniform. The homogeneity of the deposition is reflected in the sharpness of the soot – air interface (Fig. S3.2). SEM images of the cross section of the coating underpin the coating's self-similarity.
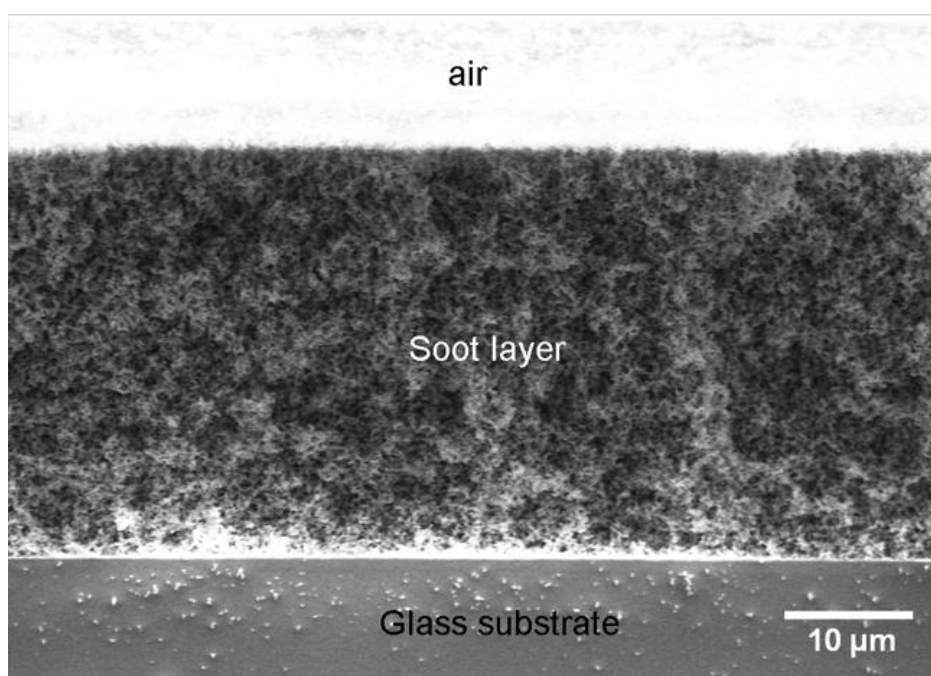

Figure S3.2: SEM image of a cross section of a superamphiphobic film. After holding the glass substrate for 25 s in a candle flame 33 ± 3 µm thick soot was deposited. For mechanical stability the soot layer was coated with 20 ± 5 nm thick silica and annealed at 600 °C for 2 h.

CONTACT ANGLE HYSTERESIS

The advancing and receding contact angles were measured by titrating 3 µl (10 µl) water (hexadecane) to a 3 µl (5 µl) drop and removing the solvent afterwards (Fig. S3.3). The data were analyzed using Image Pro Plus (Media Cybernetics). The contact angles depend on the choice of the baseline. Due to the roughness of the coating the

substrate always appears a bit blurred, making a precise location of the three-phase contact line difficult. The data were evaluated using Image Pro Plus, because this image analysis and processing software offers the option to enhance the contrast, thereby reducing the error in determining the baseline. Water drops possess contact angles above 160° and show low hysteresis, $\theta_A - \theta_R = (165° \pm 1°) - (163° \pm 1°) \approx 2°$ (Fig. S3.3A). Both the advancing and receding contact angle for drops of hexadecane are slightly lower ($\theta_A = 158° \pm 1°$, and $\theta_R = 152° \pm 1°$). Still the hysteresis is small, $\theta_A - \theta_R \approx 6°$ proving the coating's superamphiphobicity.
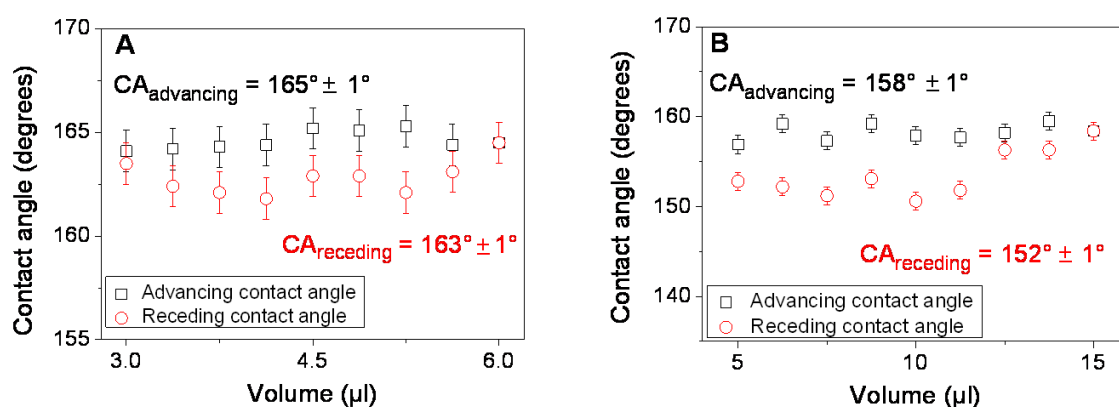
Figure S3.3: Advancing and receding contact angles for water (A) and hexadecane (B).

HEXADECANE DROP IMPACT

The impact of hexadecane drops was investigated at various velocities. The falling height varied between 4 mm and 30 cm. Figure S3.4 shows images of hexadecane drops 1 ms after lifting off. For heights of fall up to 5 cm the drops completely rebounded. This corresponds to an impact velocity of 1 m/s and a Weber number of $We = \rho R v^2 / \gamma = 23$, where ρ is the density, R the radius of the drop, v its impact velocity, and γ the liquid-air surface tension. The contact time of the drop with the coating increased from 10 ms (0.4 cm drop height) to 14 ms (5 cm). Impinging from 8 cm height left a small satellite droplet on the surface. The size of the satellite droplet increased with the height of fall. The corresponding impact velocities, Weber number, and area of the pinned satellite droplet on the coating are listed in Table S3.1.
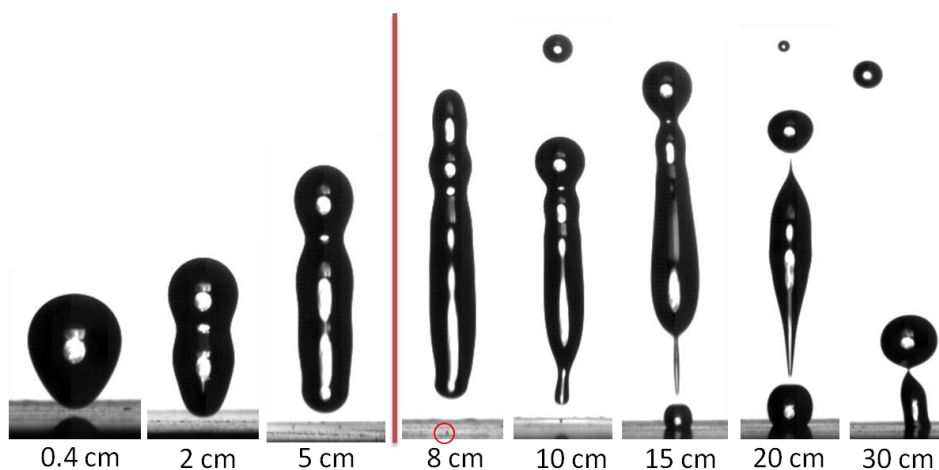
Figure S3.4: Snapshots of 5 µl hexadecane drops after impinging on a superamphiphobic surface from different heights of fall. The images were taken 1 ms after lifting off. The red line marks the height of fall, separating the region of complete rebound and partial pinning.

Table S3.1: Height of fall, impact velocity v, Weber number We, and contact area of the pinned satellite drop on the coating. Drop radii: $R = 0.85$ mm, surface tension of hexadecane: $\gamma = 27.5$ mN/m, density: $\rho_{HD} = 0.77$ g/mL, Weber number: $We = \rho R v^2/\gamma$.

Height of fall (cm)	Impact velocity (m/s)	Weber number	Pinning area (mm²)
0.4	0.3	2	0
2	0.6	10	0
5	1	23	0
8	1.3	37	0.001
10	1.4	47	0.004
15	1.7	69	0.61
20	2.0	96	1.5
30	2.4	138	1.8

Figure S3.5 shows details of the rebound of a 5 µL hexadecane drop impinging on a superamphiphobic surface at a velocity of 1.4 m/s. After the drop hit the surface at time t = 0 s, it first expanded (t = 0.93 ms), retracted (t = 7.6 ms) and then rebounded (t = 27.2 ms). The drop considerably deformed and ejected satellite drops. At the bottom of the elongated drop, a tiny satellite drop formed that stuck to the surface. This pinned satellite drop is marked by the white circle. However, this pinning is reversible. While the hexadecane drop re-impacted the surface at t ≈ 60 ms the pinned satellite drop merged with the original drop. The full drop bounced back (t = 70.1 ms), which proves the repellency of the surface to low interfacial tension liquids like hexadecane.
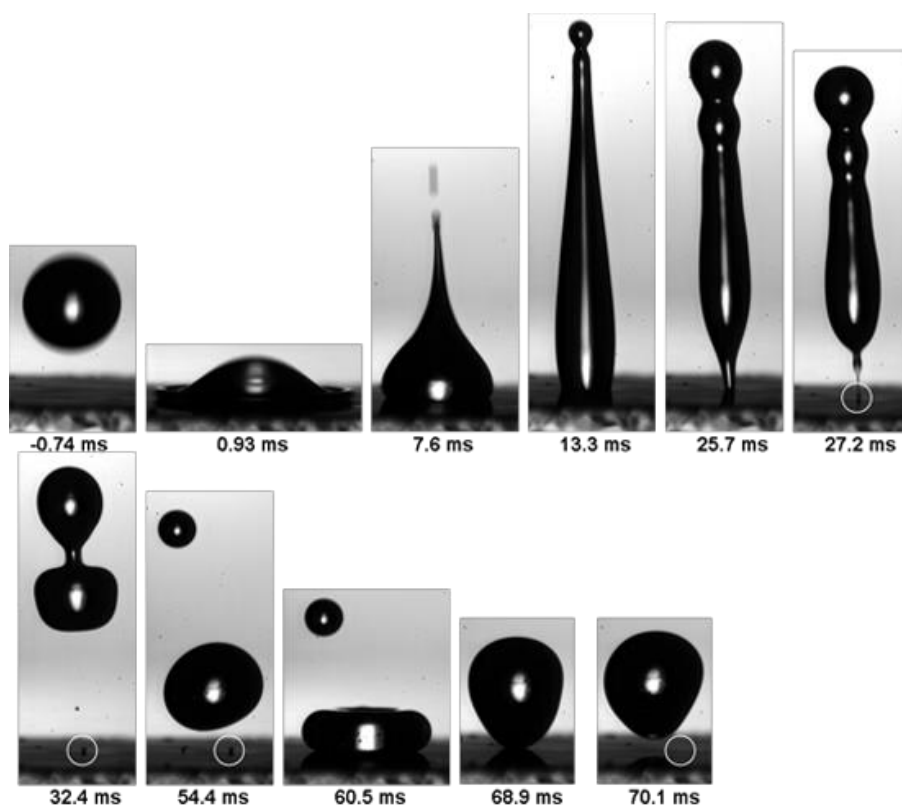
Figure S3.5: Details of the rebound of a 5 μL hexadecane drop impinging on a superamphiphobic surface at a velocity of 1.4 m/s.

DROP IMPACT RESISTANCE

The durability of the coating towards long-term drop impact was tested, letting water drops impinge a 5 μm thick coating from 1 cm and 10 cm, respectively (Fig. S3.6). For a falling height of 1 cm (impact velocity of 0.44 m/s) the coating did not show hints of altering after 360 000 drop impacts, i.e. the coating remained superamphiphobic. After impinging of 12000 water drops from 10 cm height (1.4 m/s) the coating lost its superhydrophobicity.
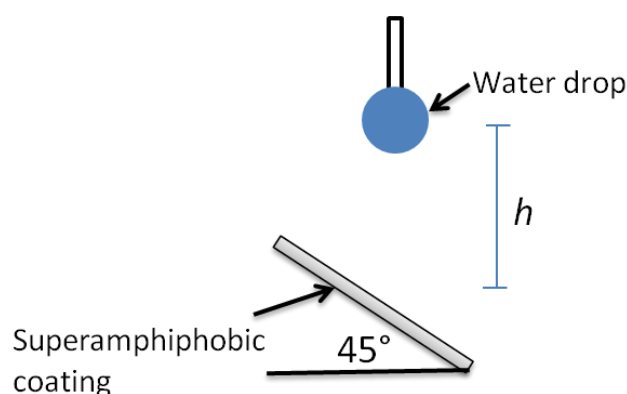
Figure S3.6: Sketch of the setup to test the coating's long term resistance against drop impact. 1 mm sized water drops impinged a 5 μm thick coating from a falling height of 1cm and 10 cm, respectively. The substrate was tilted by 45° and fixed above a sink to ensure water drain off.

SELF-CLEANING

Sand (white dots in Fig. S3.7) polluted superamphiphobic coatings were rinsed by water and hexadecane. Both solvents enwrapped the sand and took it away while the drops rolled off the surface.
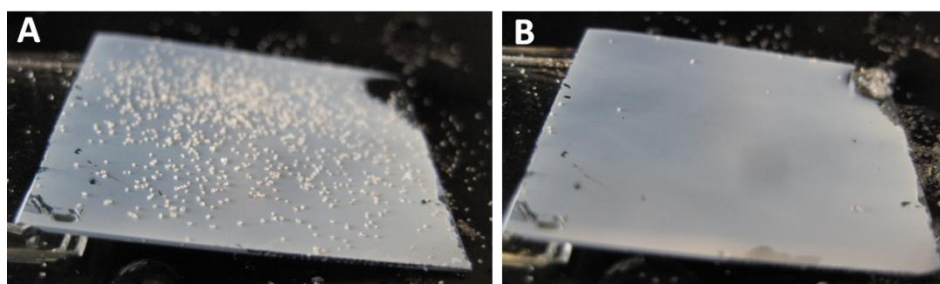
Figure S3.7: Sea sand polluted superamphiphobic surface (A) before and (B) after hexadecane drops took up the contaminants encountered on its way.

TEMPERATURE STABILITY

The static contact and roll-off angle remained unchanged after heating up to 400°C for 1 h (Fig. 3.3A). Heating the coatings at even higher temperatures decomposed the fluorosilane, causing that the coating lost its superamphiphobicity. The silica network turned hydrophilic. Superamphiphobicity can be recovered by CVD of a fluorosilane. Annealing the coating at 1100°C caused onset of sintering. This is reflected in a

smoothening of the silica strings (Fig. S3.8B). Still, the coating kept its self-similarity (Fig. S3.8A). After CVD of a fluorosilane the sintered layer remained superhydrophobic but lost its superamphiphobicity (Fig. S3.8C-D).
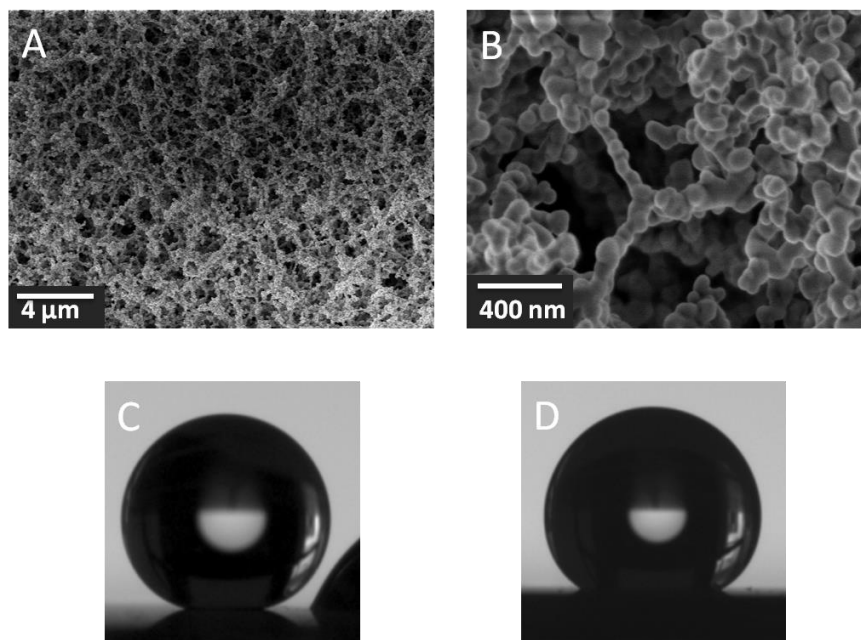
Figure S3.8: (A, B) SEM images taken after annealing an initially superamphiphobic coating at 1100°C for two hours. After CVD of a fluorosilane the contact angles with water (C) and hexadecane (D) were 163° (roll-off angle: 2°) and 149° (roll-off angle > 60°), respectively.

TRANSPARENCY OF THE COATING

The transparency of the coating depends on its thickness as well as on the thickness of the silica shells (Figs. S3.9-10). The coating's transmittance most pronounced decreased at short wavelengths. Whereas the transmittance of 1 μm thick coatings closely resembled those of pristine glass, 45 μm thick coatings showed 50 % transmittance only for wavelengths above 500 nm. The transmittance strongly decreased with the thickness of the silica shells (Fig. S3.10B). Recently, Retsch *et al*. calculated the dependence of the transmittance of hollow silica spheres on particle size and shell thickness.[117] They observed a pronounced dependence of the transmittance on the shell thickness in line with our observations.

1 μm thin coatings are still superhydrophobic, showing an unchanged SCA with water of 165° and a roll-off angle of ≈ 1°. Hexadecane drops show a slightly reduced SCA of 150° and an increased roll-off angle of 25°.
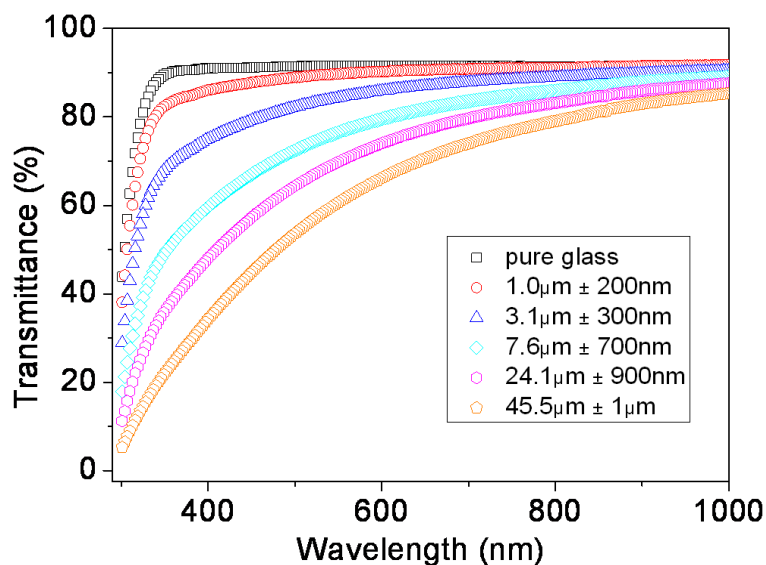
Figure S3.9: UV-VIS transmittance spectra of coatings of different thickness. The average thickness of the coating increased 1 μm to 45 μm (top to bottom). The black squares show the wavelength dependent transmittance of pristine glass. CVD of TES was performed for 24 h on all coatings.

SAND IMPACT RESISTANCE

For the sand abrasion test 20 g of commercial sand (diameter: 100 μm to 300 μm) impacted the surface from a height between 5 and 40 cm, while the substrate was held at 45° to the horizontal surface. The mechanical stability increased with the thickness of the silica shell, which increased with the duration of CVD of TES. Sand abrasion tests of the coating were performed after 1 day, 2 days, and 3 days of CVD of TES. After 3 days CVD of TES the coating can stand 5 minutes impact of 100 to 300 μm sized sand grains, impacting at a velocity of 8 km/h (25 cm), details in Table S3.2. Compared to these large particles, aerosol particles have radii below 10 μm.[118] Taking smaller grains should strongly increase the impact duration or impact velocity, due to decreased impact energy.[60] A predictive description of the coatings mechanical stability is not yet available because breakage depends on sample history,[119] as well as on details of the fractal-like silica network, such as local density, shell thickness, angles between neighboring strings, etc. Thicker coating can provide longer damage resistance, both, against drop and sand impact.

Thick shells are mechanically more stable, but less transparent (Fig. S3.9B). After 3 days of CVD of TES the fractal pearl necklace-like morphology of the silica strings smoothened and the strings turned more rod-like (Fig. S3.10). The average string-string distance decreased as did the coating's superamphiphobicity. After 3 days of

CVD of TES the hexadecane drops showed a SCA of 145° and a roll off angle of 40°. The contact and roll-off angle remained unchanged for water.
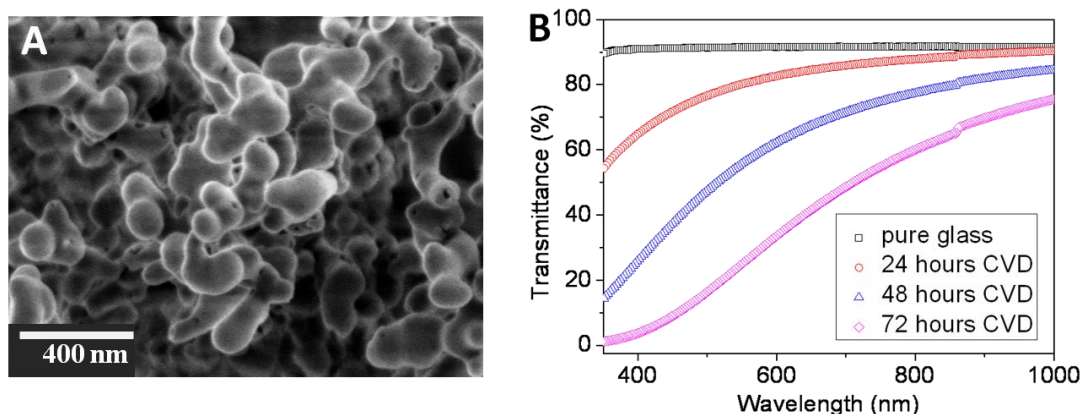
Figure S3.10: (A) SEM image of the coating after performing CVD of TES for 72 hours. (B) Transparency of an 8 μm thick silica porous film after different times of CVD of TES.

Table S3.2: Dependence of the duration of CVD of TES on the thickness of the silica shells, the coatings transparency at a wavelength of 500 nm, and impact velocity$_{SA}$ of the sand grains. The thickness of the coating was taken to be 8 μm for all samples. At the given impact velocities$_{SA}$ the coating's superamphiphobicity lasted for 5 min sand abrasion.

Time of CVD of TES	Thickness of silica shell	Transparency	Impact velocity$_{SA}$
24 hours	20 ±5 nm	77 %	1.4 m/s
48 hours	35 ±5 nm	47 %	1.7 m/s
72 hours	60 ±10 nm	17 %	2.2 m/s

DAMAGE TOLERANCE

The coating did not lose its superamphiphobicity after the top layer has been damaged by sand or drop impact. Many superhydrophobic surfaces don't show damage tolerance, because if the coating's top layer is destroyed water contacts a less rough or a high energy surface.[120] In case of a high energy surface, these hydrophilic patches can act as adhesion points, increasing the roll off angle of a deposited drop or even inducing a Cassie-to-Wenzel transition. Likely, the damage tolerance of the fractal-like coating is caused by the small fractional area of the damaged silica network, $f_3 = f_{flat,silica}$.

The Cassie-Baxter equation for a damage surface can be rewritten as:

$$\cos \theta_{\text{Cassie}} = f_1 \cos \theta_{\text{air}} + f_2 \cos \theta_{\text{flat,fluorosilane}} + f_3 \cos \theta_{\text{flat,silica}}.$$

f_i is the fractional area of air, fluorinated silica, and silica and $f_1 + f_2 + f_3 = 1$.

Inserting $\cos \theta_{\text{air}} = -1$ and $f_1 = 1 - f_2 - f_3$ in the Cassie-Baxter equation, it reads:

$$\cos \theta_{\text{Casssie}} = -1 + f_2 \left(1 + \cos \theta_{\text{flat,fluorosilane}}\right) + f_3 \left(1 + \cos \theta_{\text{flat,silica}}\right).$$

For sufficiently small f_3, the contact angle remains high even if $\cos \theta_{\text{flat,silica}}$ is low.

Movie S3.1: A water drop (volume: 9 µL water, height: 5 cm, impact velocity: 1 m/s) impinging a superhydrophobic coating made of candle soot (without CVD of TES). During impact the drop took soot particles along from the impacted area.

Movie S3.2: A µL-sized water drop gently deposited on a superamphiphobic glass. The movie documents the excellent water repellency of the coating and its low adhesion to water. The advancing and receding contact angles were almost identical ($\theta_A - \theta_R \approx 2°$). The low adhesion is supported by the negligible deformation of the drop while detaching.

Movie S3.3: The movie shows a dry sand abrasion test on a transparent superamphiphobic surface. 20 g sand is falling from a height of 40 cm. The 100 to 300 µm sized sand grains have a velocity of 2.8 m/s just before impinging the surface. After abrasion, the surface remains superamphiphobic. Deposited water or hexadecane (see main text) drops easily roll off.

4   HOW SUPERHYDROPHOBICITY BREAKS DOWN

Periklis Papadopoulos,[1] Lena Mammen,[1] Xu Deng,[1,2] Hans-Jürgen Butt,[1] and Doris Vollmer[1]

[1] Max Planck Institute for Polymer Research,

Ackermannweg 10, D-55128, Mainz (Germany)

[2] Center of Smart Interfaces, Technische Universität Darmstadt,
Petersenstrasse 32, D-64287, Darmstadt (Germany)

A droplet deposited or impacting on a superhydrophobic surface rolls off easily, leaving the surface dry and clean. This remarkable property is due to a surface structure which favors the entrainment of air cushions beneath the drop, leading to the so called Cassie state. The Cassie state competes with the Wenzel (impaled) state, where the liquid fully wets the substrate. To utilize superhydrophobicity, impalement of the drop into the surface structure needs to be prevented. In order to understand the underlying processes we image the impalement dynamics in three dimensions by confocal microscopy. While the drop evaporates from a pillar array, its rim recedes via step-wise depinning from the edge of the pillars. Before depinning, finger-like necks form due to adhesion of the drop at the pillar's circumference. Once the pressure becomes too high, or the drop too small, the drop slowly impales the texture. The thickness of the air cushion decreases gradually. As soon as the water-air interface touches the substrate, complete wetting proceeds within milliseconds. This visualization of the impalement dynamics will facilitate the development and characterization of superhydrophobic surfaces.

4.1   INTRODUCTION

Many surfaces in nature, including several plant leaves,[18] legs of the water striders,[20] and the wings of some insects[121],[122] are superhydrophobic. They display apparent contact angles with water greater than 150° and low contact angle

hysteresis.[18],[20],[121],[122] Tilting a superhydrophobic surface by a few degrees is already sufficient for a drop to overcome adhesion, roll off and remove dirt.[18],[20],[121],[122] This has stimulated extensive research to design artificial superhydrophobic surfaces. A variety of techniques are developed, often stimulated by mimicking natural surfaces.[73],[99],[123],[124],[125],[126] Prospective applications include self-cleaning and anti-fouling surfaces[18],[60],[99],[122] and textiles,[127],[128] membranes for oil-water separation,[129] and drag reduction in microfluidics.[75] Superhydrophobic coatings can enhance[130] or reduce[131] adsorption of cells or proteins. Minute amounts of proteins or biomolecules can be deposited on arrays of micropillars, offering promising routes to sensitive high-throughput analysis on lab-on-chip benches.[132] Patterned superhydrophobic coatings provide new strategies to guide drops[133] or to tune drop adhesion.[134] Nanocrystals can be deposited[135] and grown[136] on the tips of micropillar arrays. For all these applications the robustness of a coating against complete wetting is crucial.

To fabricate a superhydrophobic surface two key features are required: a low surface energy of the material and a topography with roughness on the nano- and microscale. In this case, air can be entrained when placing a sessile drop on top, which leads to the low adhesion. In this so called Cassie or fakir state the drop rests on top of the asperities of the rough substrate (Fig. 4.1B). As proposed by Cassie and Baxter[8],[137] a water drop on a partially wetted surface should adopt an apparent contact angle θ^{app} given by the weighted sum $\cos\theta^{\mathrm{app}} = f\cos\theta - (1-f)$.[8],[75],[138],[139],[140] Here f denotes the fractional area of contact of water with the solid. θ is the contact angle on a flat surface of the same material. In the following, we distinguish between the macroscopically observed apparent contact angle and the material contact angle. The apparent contact angle is the one observed by eye or with a low-resolution microscope. It relates to a length scale much larger than the microstructures forming the superhydrophobic layer, thus typically larger than 10 μm. The material contact angle is the contact angle formed by the liquid on a smooth surface. It is derived by extrapolating the liquid shape on the 10 nm – 2 μm scale to the interface. The actual material contact angle at the contact line θ_{CL} has to be between the advancing and receding ones: $\theta_{\mathrm{R}} \leq \theta_{\mathrm{CL}} \leq \theta_{\mathrm{A}}$. The Cassie state competes with the Wenzel (impaled) state, where the drop follows the topography of the surface and no air is entrapped.[30],[141] The apparent contact angle in the Wenzel state can be almost as high as the one in the Cassie state.[5] However, the two wetting states differ in the contact angle hysteresis, which is much lower in the Cassie state.[7] Since the Cassie state minimizes the adhesion and the roll-off angle, the term Cassie state is often used as synonym for superhydrophobicity.[129]

The Cassie-to-Wenzel transition can be triggered by vibrations,[142] squeezing,[126] impact,[112] rapid deceleration,[143] application of an electric field,[144] or evaporation.[112],[145],[146],[147],[148] Different impalement scenarios have been discussed. For situations, where inertia is negligible, the two most important ones are depinning and sagging.[7],[107],[143],[145],[147],[148],[149],[150],[151],[152] In depinning the three phase contact line, or briefly contact line, unpins from the edge of the asperity.[153] Then the contact line slides down the pillar wall, beginning the transition to a fully wetted state. In the sag-mechanism the underside of the liquid surface sags until it reaches the substrate.[145] The Cassie-to-Wenzel transition takes place as soon as the lowest point of the meniscus touches the bottom surface.[7],[149] To simplify the discussion, we discriminate between the *contact line* on the microscopic and the *rim* on the macroscopic length scale.

Despite well-defined model systems, the transition dynamics is still poorly understood due to difficulties in monitoring the temporal evolution of the air cushion and the liquid-air meniscus between the asperities with sufficient special resolution.[154] Even the time scale of the impalement transition remains unclear. So far most detailed information was obtained by high speed video microscopy[132],[149] and scanning electron microscopy.[140],[150] However, neither of these techniques provides quantitative 3-dimensional information. Detailed insight in the transition dynamics would sharpen the fundamental understanding of superhydrophobicity and be constitutive to optimize the robustness of superhydrophobic coatings. Here, we study the Cassie-to-Wenzel transition of water drops evaporating on arrays of hydrophobic micropillars (Fig. 4.1A). The transition dynamics and especially the evolution of the thickness of the air cushions are monitored by laser scanning confocal microscopy (briefly confocal microscopy). The shape of the water-air cushion interface between the pillars and up to 200 µm above the substrate is imaged. Thus, we can measure both the macroscopic contact angle and the variation of the microscopic angle at the pillars. By varying the geometry of the substrate we observe the impalement transition in both depinning and sagging modes.

4.2   RESULTS AND DISCUSSION

Cassie-to-Wenzel transition. A fluorescently labeled water drop is left to evaporate on a labeled array of PDMS pillars (Fig. 4.1). The superposition of the fluorescence and reflection images accurately depicts the morphology of the water-air and pillar-air interfaces (Fig. 4.1C-D). Vertical sections of a drop in the Cassie state (Fig. 4.1C)

show two well separated horizontal reflections between neighboring pillars. They result from light reflected at the PDMS-air and air-water interfaces. The space in between (black regions) is filled with air. The height difference of the two reflections denotes the thickness of the air cushion. As water evaporates the apparent contact angle decreases. The rim is pinned and the drop remains in the Cassie state (Fig. 4.1E). Only when the apparent contact angle reaches $\theta^{app} = 128°$, the drop suddenly wets the space between the pillars (Movie S4.1). The absence of reflection, supported by the fluorescence images of water and PDMS, proves the complete wetting of pillars, without entrained air (Fig. 4.1D).
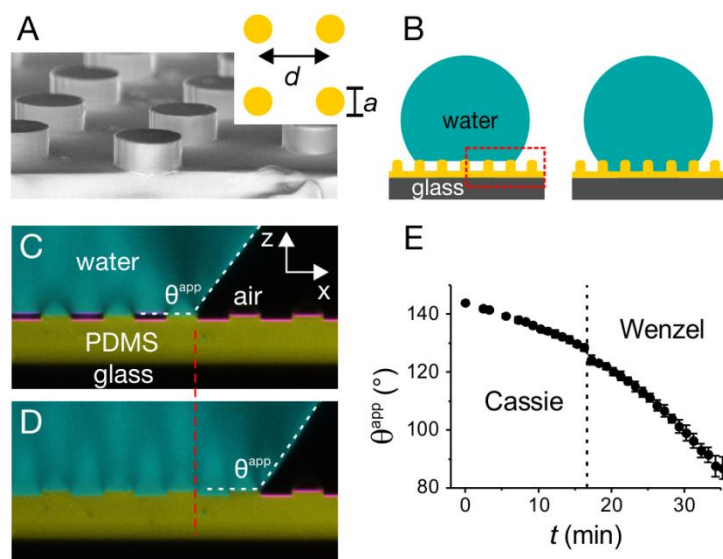
Figure 4.1: Model superhydrophobic surfaces. (a) Scanning electron microscopy image of a microstructured PDMS surface. Dimensions of the pillars: center-to-center distance d = 40 μm, diameter a = 20 μm, and height h = 5 μm, giving f_{PDMS} = 0.2. (b) Sketch of a drop deposited on the substrate in the Cassie (left) and Wenzel (right) state. (c) Typical confocal microscopy image of a vertical section of a water drop rim just before and (d) just after the Cassie-to-Wenzel transition induced by evaporation. Fluorescent emission from water and PDMS is shown in cyan and yellow, respectively, and reflection in magenta. (e) Change of the apparent contact angle θ^{app} with time.

The Cassie-to-Wenzel transition is accompanied by a decrease of the apparent contact angle by 3°. The rim jumped outwards so that the volume of the drop V was conserved. Assuming a spherical cap shape with radius R the contact radius b is (Fig. S4.1):

$$b = R \sin \theta^{\mathrm{app}} = \left(\frac{3V}{\pi}\right)^{1/3} \frac{\sin \theta^{\mathrm{app}}}{(\cos^3 \theta^{\mathrm{app}} - 3 \cos \theta^{\mathrm{app}} + 2)^{1/3}} \qquad (4.1)$$

A jump of θ^{app} from 128° to 125° leads to an increase of b by 4.7 %. The actual rim of the drop resembles an octagon with rounded edges.[155] The maximum radius of the contact area jumps from 960 to 1000 μm. This increase of 4.2 % is close to the calculated value. The contact line remains pinned during further evaporation, while the contact angle decreases continuously.

Sag impalement. To analyze the kinetics of the Cassie-to-Wenzel transition in more detail, we employ microarrays with larger height and spacing between the pillars. Although PDMS pillars are frequently used,[112] high PDMS pillars easily deform under capillary forces. Therefore, we use stiffer SU-8 pillars for these experiments. Figure 4.2 shows a typical drop in the Cassie state. Since we did not fluorescently label the water in this case, the surface of the drop is detected from reflections. The almost spherical drop rests on 37 pillars. More than one hundred horizontal sections of the reflection of light vertically spaced by 0.25 μm are combined in a 3-dimensional image (Fig. 4.2B). The mean curvature of the drop $1/R$ is governed by the Laplace pressure $P = 2\gamma/R$, where $\gamma = 72$ mN/m is the surface tension of water. Flattening of the drop by gravity is small since the radius of the drop $R < 1$ mm is much smaller than the capillary length of 2.7 mm.

To quantify the decreasing thickness of the air cushion h_{air} during evaporation we extracted contour plots of the water-air interface (Fig. 4.2C). The variation of h_{air} along the main axis and the diagonal is included (Fig. 4.2D). The lowest height h_{min} is located at the center of each square, whereas a saddle point is formed along the main axis. The minimum of h_{air} along the main axis is almost 2 μm higher than the minimal height of the air cushion along the diagonal. From the respective variation of h_{air} the contact angle of water at the contact line θ_{CL} can be derived (Fig. S4.2). It is maximal along the diagonal. This is the material contact angle, which can vary in the range $\theta_{\mathrm{R}} - 90° \leq \theta_{\mathrm{CL}} \leq \theta_{\mathrm{A}}$ according to Gibbs' criterion, if measured from the vertical.[155] In this case is $\theta_{\mathrm{CL}} = 106°$ just after deposition of the drop.

As evaporation proceeds, the curvature of the drop decreases and the Laplace pressure increases. The Laplace pressure of the drop is extracted from the mean curvature of the surface by fitting the water-air interface coordinates with a 2-dimensional function (Fig. S4.3). The water-air interface below the drop sags downwards, the air cushion decreases and the contact angle θ_{CL} increases (Fig. 4.2E-F). The water-air interface remains pinned, since the large pillar spacing prevents θ_{CL}

from exceeding the advancing material contact angle, $\theta_A = 115°$ (Fig. 4.2F).[154] The evolution of the 3-dimensional shape of the water-air interface is shown in Movie S4.2. At the first contact of the drop with the substrate i.e. $h_{min} = 0$, the drop spontaneously wets the full surface within milliseconds. The Laplace pressure just before the transition is 250 Pa.
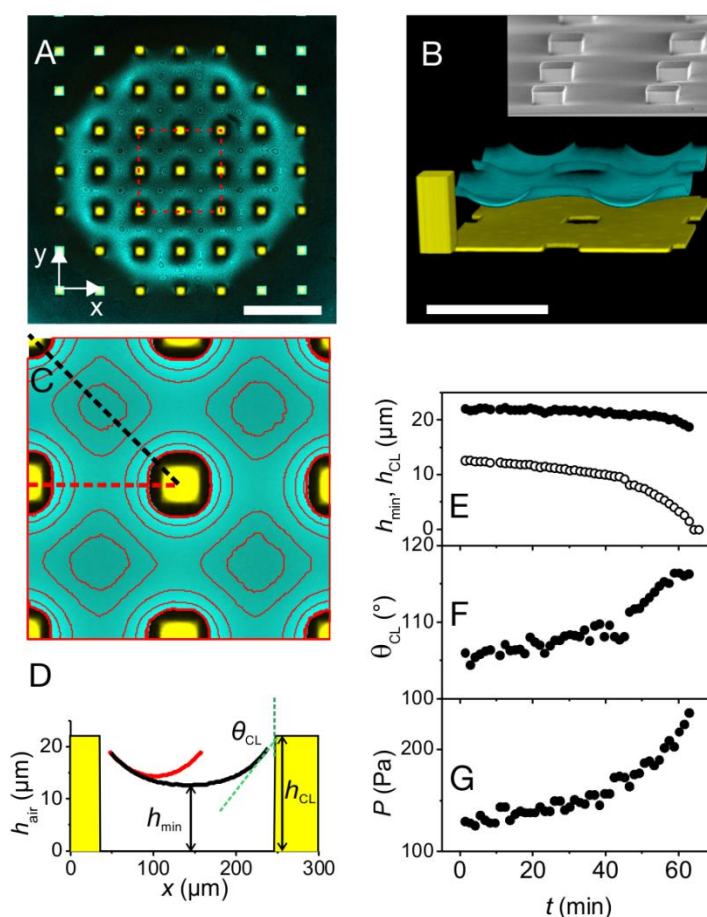
Figure 4.2: Cassie-to-Wenzel transition via sagging. (a) Reflection from the water-air cushion interface (blue) of a droplet deposited on the microstructured surface composed of SU-8 pillars (yellow squares) taken by confocal microscopy (bar = 400 μm). This horizontal section through the drop is taken 2 μm below the pillar surface. Dimensions of the pillars: $d = 200$ μm, $a = 50$ μm, and $h = 23$ μm. (b) 3-dimensional image of the reflection of light from the SU-8–air and air–water interfaces (bar = 100 μm). An artificial pillar is shown for comparison (Movie S4.2). The z-axis is 5× magnified. Inset: SEM image of the pillars. (c) Contour plot of the thickness of the air cushion. The minimum thickness h_{min} is located at the center between 4 pillars. Contour lines corresponding to h_{air}= 19 μm, 17 μm, 15 μm and 13 μm are shown. (d) Variation of the thickness of the air cushion along the diagonal (black) and main axis (red). The two axes are marked in (c). The contact angle θ_{CL} obtained from extrapolating the thickness of the air cushion to the edge of the pillars is indicated. (e) Change of h_{min} (hollow circles) and the thickness of the water-air cushion at the three phase contact line h_{CL} (solid circles) with time. (f) Change of θ_{CL} and (g) Laplace pressure P with time.

Depinning impalement. With decreasing inter-pillar distance it becomes more likely that θ_{CL} exceeds its maximum value θ_A before the water-air interface touches the substrate. The snapshot in Figure 4.3A shows the beginning of a depinning impalement (Movie S4.3). Depinning does not proceed simultaneously from all pillars but depends on detailed differences of the surface structure at the edge of the pillars. During impalement the size of the drop and accordingly the pressure hardly change. Gradually, the curvature of the water-air interface beneath the drop increases (Fig. 4.3B-C). Therefore, θ_{CL} varies between pillars. The contact line slides downward with an average speed of 0.5 µm/s until the drop touches the bottom surface and wets the whole substrate spontaneously. This velocity corresponds to the rate at which the drop evaporates. The radius of curvature of the drop decreases at roughly 0.7 µm/s close to the transition.
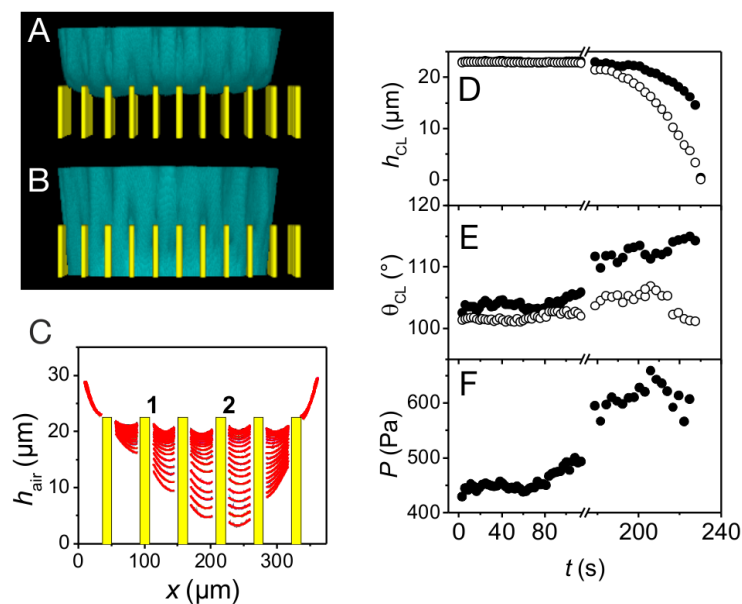
Figure 4.3: Cassie-to-Wenzel transition via depinning. (a) 3-dimensional image of a fluorescently labeled water drop on an array of SU-8 pillars (d = 20 µm, a = 5 µm, h = 5 µm, z-axis is 10× magnified). A 3-dimensional image (300×300×20 µm³) was recorded every 0.90 s. For better visualization we replace the microscopic data of the fluorescently labeled pillars by artificial pillars (Fig. S4.4). (b) The same drop after the collapse of the Cassie state. (c) Profiles of the thickness of the air cushion measured along a diagonal and passing through the center of the drop. Profiles are measured every 3s (d = 40 µm, a = 10 µm, h = 23 µm). (d) Change of the height of the contact line at the sidewalls of the two pillars marked in (c): **1** (solid circles) and **2** (hollow circles). (e) Change of the microscopic contact angle θ_{CL} during evaporation; position **1** (solid circles) and **2** (hollow circles) and (f) Laplace pressure P with time.

Simulations of drop collapse showed that the drop tends to acquire an overall spherical shape, outside and inside the substrate and impalement does not cause a jump of the drop rim.[154] Indeed, if impalement proceeds via depinning, it does not need not to be accompanied by a jump of the rim (Fig. 4.3B, Movie S4.3). According to our observations the rim jumps if the receding angle of the Cassie state exceeds the advancing angle of the wetted (Wenzel) state, which depends on the height and shape of the pillars. Therefore a jump of the contact line is more likely if the Cassie-to-Wenzel transition proceeds via sagging than via depinning.

Contact angle hysteresis.   Finally, we discuss whether a drop in the Cassie state always shows a low contact angle hysteresis. This would imply that a surface which keeps drops in the Cassie state is superhydrophobic.[153] However, even for the array with 200 μm pillar-pillar distance (Fig. 4.2, solid fraction f = 6 %) the drops show a high roll-off angle of $\alpha = 17°$ (Movie S4.4). The reason for the high roll-off angle becomes clear when watching the rim of a drop more closely as water evaporates (Fig. 4.4). Immediately after deposition, the drops are almost spherical although pinning at the edges of a few pillars is visible (Fig. 4.4A). As water evaporates the drop depins step-wise from the top of the pillars (Movie S4.5). Tiny water droplets are left on the top of the pillars (Movie S4.6).[132],[135] The time between successive depinning events varies between less than a second and 10 min. When the bottom surface of the drop gets into contact with the substrate the whole drop spontaneously undergoes a Cassie-to-Wenzel transition. The contact line jumps outward (Fig. 4.4B-C). Part of the air remains trapped at the backside of the pillars with respect to the flow profile (Fig. 4.4C, inset). Thus, from the position of the bubbles with respect to the pillar the first contact can be localized. The size of the bubbles continuously decreases by diffusion through the water phase until after about 10 minutes the bubbles disappeared.
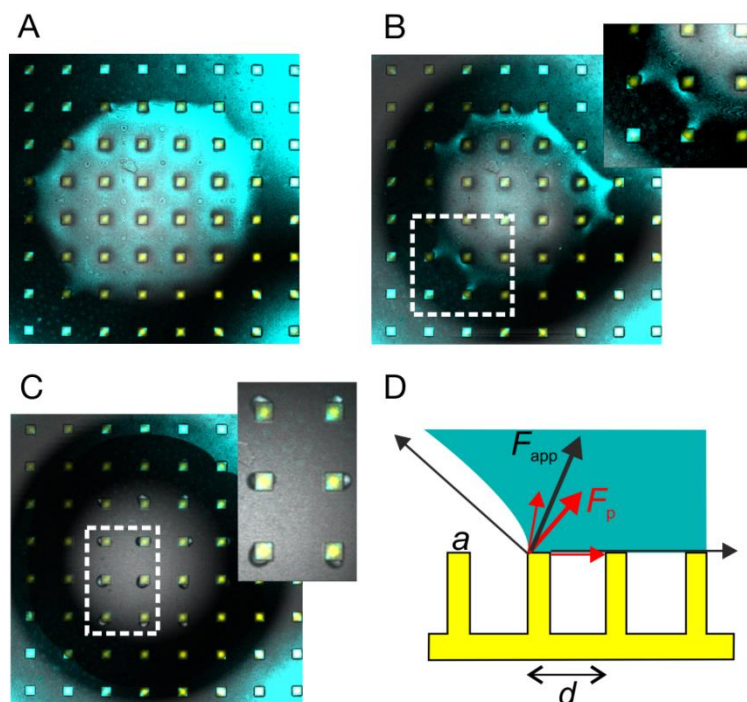
Figure 4.4: Drop depinning during evaporation. (a) Superposition of transmission (bluish) and the reflection from the drop-air cushion interface (cyan) on SU-8 pillars (yellow) ($d = 200$ µm, $a = 50$ µm, $h = 25$ µm) just after deposition. (b) Rim of the drop just before the impalement transition. Inset: Pinning-induced necks of the drop. (c) Horizontal section recorded just after the impalement transition. Inset: air bubbles are visible at the backside of the pillars. (d) Macroscopic pinning force F_{app} at the receding part of the drop rim (black arrows). Its horizontal component must be equal to the sum of horizontal components of pinning forces F_P at the pillars (red arrows). It is assumed that the mean curvature of the drop is zero.

The images show that wetting is dominated by pinning rather than thermodynamic equilibrium. The Cassie-Baxter equation cannot be valid since the drop is in a metastable state. Choi *et al.* suggested a modified Cassie-Baxter equation to calculate the advancing and receding contact angles. Their model is based on the calculation of the local maxima and minima of the interfacial energy.[140] For the receding contact angles on discrete pillars the solid areal fraction is essentially replaced by the solid line fraction. Reyssat *et al.* followed a geometric approach to estimate the receding contact angle, based on the equivalence of macroscopic and microscopic pinning forces.[156]

With θ_{CL} measured at each pillar by confocal microscopy the apparent contact angle can be calculated from the following balance of forces: the macroscopic horizontal component of the interfacial force at the rim per unit length is $F_{app,h} = \gamma (1 + \cos \theta^{app})$ (Fig. 4.4D). This force is made up of the force of the individual pillars.

Microscopically, each pillar supports a horizontal component of the pinning force of $\gamma\, a \cos\theta_R$ at the rear side and nearly γa at the front side (for large drops $\theta_{CL} \approx 90°$, Figs. 4.2-3) until just before depinning. If the contact line is pinned this leads to

$$\gamma d (1 + \cos\theta^{\text{app}}) = \gamma\alpha(\cos\theta_R + 1) \ \Rightarrow \cos\theta^{\text{app}} = \frac{a}{d}(\cos\theta_R + 1) - 1$$

with respect to a movement along the main axis. With d = 200 µm, a = 50 µm, and θ_R= 85° we get θ^{app} = 137°. This compares well to the measured value of 135°. Our approach can take the finite size of a drop and variations of the contact line into account. The horizontal pinning force per pillar is 3.9 µN.

This pinning force also provides an estimate for the roll-off angle α. Therefore we compare the pinning force to the force caused by the weight when tilting the plate.[156] The component of the weight of the drop parallel to the surface is $F_\parallel = V\rho g \sin\alpha$. Setting both forces equal leads to a roll-off angle α of

$$V\rho g \sin\alpha = n\gamma\alpha(\cos\theta_R + 1) \ \Rightarrow \sin\alpha = \frac{n\gamma a}{V\rho g}(\cos\theta_R + 1).$$

Here n is the numbers of pillars holding the drop. With a drop volume V = 6 µL the roll-off angle is α = 4° for n = 1 and 19° for n = 5. The latter is more plausible for a drop of this size (Figs. 4.2-3), hinting that for larger drops the roll-off angle is affected by simultaneous depinning from several pillars. Consequently, a stable Cassie state and a high apparent contact angle do not necessarily imply a low roll-off angle and superhydrophobicity.

4.3   CONCLUSION

We image the collapse of the Cassie state for a series of model surfaces. By confocal microscopy details of the impalement dynamics are resolved. In particular, the evolution of the thickness of the air cushion can be recorded in three dimensions. Depending on the geometry, impalement can extend over several minutes. The downward velocity of the meniscus is related to the evaporation rate. When the drops recede we observe single depinning events and the formation and the breakage of finger like necks. Calculated apparent receding contact and roll-off angles agree well with the measured data. We expect that confocal microscopy will become a standard technique to characterize superhydrophobic surfaces, since this time resolved 3-dimensional information can be gained for every transparent substrate.

4.4   MATERIALS AND METHODS

LITHOGRAPHY

Microarrays consisting of flat-top cylindrical pillars made of PDMS (Fig. 4.1A) and rectangular pillars made of SU-8 photoresist (Fig. 4.2A-B) were fabricated using lithography (Supplementary Methods). Both were arranged on glass in a square lattice of center-to-center distance d. The corresponding surface fractions are

$$f_{\text{PDMS}} = \frac{\pi}{4} \left(\frac{a}{d} \right)^2 \text{ and } f_{\text{SU}-8} = \left(\frac{a}{d} \right)^2. \text{ Here } \alpha \text{ denotes the diameter (PDMS) or edge}$$

length (SU-8), respectively (Fig. 4.1A, inset, Fig. 4.2A-B). The surface of the SU-8 pillars was coated with a semifluorinated silane to decrease the surface energy. Advancing and receding contact angles for water on flat parts of the surface were $\theta_A = 112 \pm 2°$, $\theta_R = 70 \pm 10°$ on PDMS and $\theta_A = 118 \pm 2°$, $\theta_R = 85 \pm 5°$ on SU-8. Hydrophobic perylenemonoimide dye (PMI, emission maximum at $\lambda_{\text{PMI}} = 540$ nm) was added to uncrosslinked PDMS or SU-8.[155] Water-soluble perylenediimide, (WS-PDI) was used to dye the water because of its negligible interfacial activity.

LASER SCANNING CONFOCAL MICROSCOPY

To visualize the Cassie and Wenzel state and to record the impalement dynamics, we deposited 7 μL water drops on the micro-patterned surfaces (Fig. 4.1B). The confocal microscope used (Leica TCS SP5 II – STED CW) has five detectors with adjustable spectral regions, which allowed us to simultaneously measure fluorescence from water and PDMS or SU-8, as well as the reflected light from the interfaces (Fig. 4.1C-D).[155] To verify that the results are not influenced by the dye[157],[158] some measurements were repeated with pure water in reflection mode. A dry objective (40×/0.85) was used since it allows to accurately measure the optical path length in air i.e. the thickness of the air cushion. The image resolution was about 0.25 μm and 1.0 μm in the horizontal and vertical directions, respectively, except for areas closer than about 0.1d to the edges of the pillars. The coordinates of the water-air interface are extracted by fitting reflection or fluorescence profiles along the z-axis with a Gaussian or sigmoidal function, respectively, with accuracy better than 0.3 μm.

4.5 ACKNOWLEDGEMENTS

4.6 SUPPLEMENTARY INFORMATION

FABRICATION OF PDMS PILLARS

The microstructures consisted of PDMS pillars arranged in a square lattice on glass. The PDMS pillars were prepared by soft-molding of poly(dimethylsiloxane) (PDMS, Sylgard 184, Dow Corning) on SU-8 patterned templates that were hydrophobised with (1H,1H,2H,2H)-perfluorooctyltrichlorosilane. PDMS was fluorescently labeled with PMI dye that was mixed with PDMS and the crosslinker (0.05 mg/mL).[159] The blend was poured onto the template and covered with a cover slip (170 μm thick). The sample was heated up and kept at 90°C for 4 h. Finally, the cover slip with the attached PDMS pillars was slowly removed from the template.

FABRICATION OF SU-8 PILLARS

The pillar structures were made by photolithography using a SU-8 photoresist (Microchem, Newton MA, USA). Glass slides with a thickness of 170 μm were cleaned with acetone in an ultrasound bath and dried in a vacuum oven (Heraeus) at 170 °C. The SU-8 2025 (or SU-8 2005) photoresist was first mixed with the hydrophobic N-(2,6-diisopropylphenyl)-3,4-perylenedicarboxylic acid monoimide (PMI) dye at a concentration of 0.05 mg/mL. Then the mixture was spin-coated on the glass slides. The substrates were then soft baked at 95 °C for 4 min and allowed to cool down slowly for 1 h. Then they were exposed to UV light (mercury lamp at 350 W) for 35 s (or 30 s) using a Karl-Suss mask aligner and baked at 95°C for 4 min. The substrates were cooled down slowly for 12 h and finally developed with a SU-8 developer (Microchem, Newton MA, USA) and rinsed with 2-propanol. To hydrolyze the surface of SU-8 and create OH groups the surfaces were treated with 1M HCl and 0.1 M NaOH overnight at room temperature. Finally, the surfaces were hydrophobized with

(1*H*,1*H*,2*H*,2*H*)-perfluorooctyltrichlorosilane by chemical vapor deposition. The thickness of the films was 23 μm or 5 μm as verified by scanning electron microscopy and confocal microscopy.

CONTACT ANGLE MEASUREMENTS

Contact angle measurements were performed with a contact angle meter, Data Physics, OCA35. Static contact angles were measured depositing a liquid droplet of 6 μL on the surface. Advancing and receding contact angles were measured using a sessile droplet of 5 μL, with the needle in it, and then subsequently increasing and decreasing the liquid volume at a rate of 1 μL/s.

INTERFACIAL TENSION

Interfacial tension was measured following the Wilhelmy plate method using a platinum plate with a DCAT11 tensiometer (DataPhysics Instruments GmbH).

SCANNING ELECTRON MICROSCOPY (SEM)

The morphology of the substrates was characterized by SEM with a LEO 1530 Gemini (Zeiss, Oberkochen, Germany) at low operating voltages (0.5-1.4 kV). The samples were not modified before measurement.

CONFOCAL MICROSCOPY

A Leica TCS SP5 II – STED CW inverted confocal microscope with five detectors was employed. The spectral ranges could be freely varied, allowing the measurement of the emission from different dyes and the reflected light from the interfaces simultaneously. Hydrophobic *N*-(2,6-diisopropylphenyl)-3,4-perylene dicarboxylic acid monoimide dye (PMI)[160] was added to PDMS or SU-8. For water, various hydrophilic dyes were tested. Most dyes tend to adsorb at the water-PDMS or water-air interface, changing the interfacial tensions. Water-soluble *N*,*N'*-(2,6-diisopropylphenyl)-1,6,7,12-tetra(1-methylpyridinium-3-yloxy)-perylene-3,4,9,10-tetracarboxylic acid diimide tetramethane-sulfonate[161] (WS-PDI) was the most hydrophilic dye. The high efficiency of WS-PDI in water arises from the

diisopropylphenyl groups that hinder stacking and the high hydrophilicity of pyridinium salt. 0.1 mg/mL is sufficient to image the dyed water drop by laser scanning confocal microscopy. At these concentrations the dye hardly changes the surface tension γ of water. At a concentration of 0.1 mg/mL (0.06 mM) in water, the surface tension of the solution was 71 mN/m, only slightly lower than that of pure water γ_L = 72 mN/m (γ_L = 72 mN/m at 0.05 mg/mL and γ_L = 70 mN/m at 0.2 mg/mL). The emission maximum of PMI in PDMS is at λ_{PMI} = 525 nm and for WS-PDI in water at $\lambda_{WS\text{-}PDI}$ = 590nm i.e. well above that of PMI, so the overlap in fluorescence from dyed PDMS and water was minimal.[159] To excite the dyes two wavelengths were used: PMI was excited using the argon line at 488 nm; WS-PDI was excited using the 561 nm wavelength of a DPSS laser.
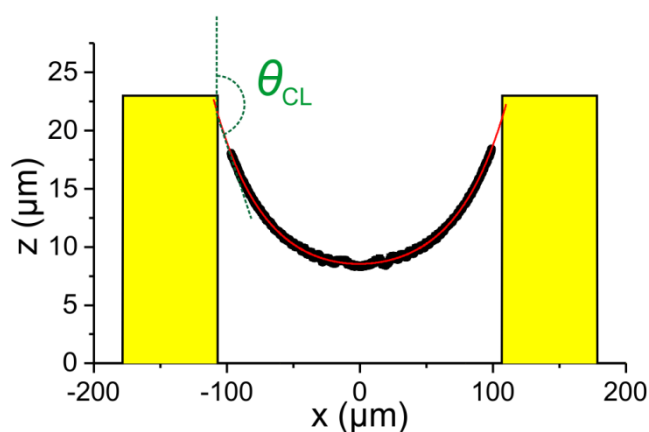
Figure S4.1: Measurement of the contact angle θ_{CL}. The profile of the air cushion can be determined up to 0.05 d from the sidewall of a pillar. The high refractive index of the pillars (n = 1.6) prevents to measure the profile of the water-air interface closer to the walls. The profile along a diagonal of the quadratically arranged pillar arrays is fitted with the empirical equation $h_{air} = \alpha \cos h\, x/b$ and is extrapolated to the edge of the pillars. The tangent at the edge with respect to the vertical yields the contact angle.
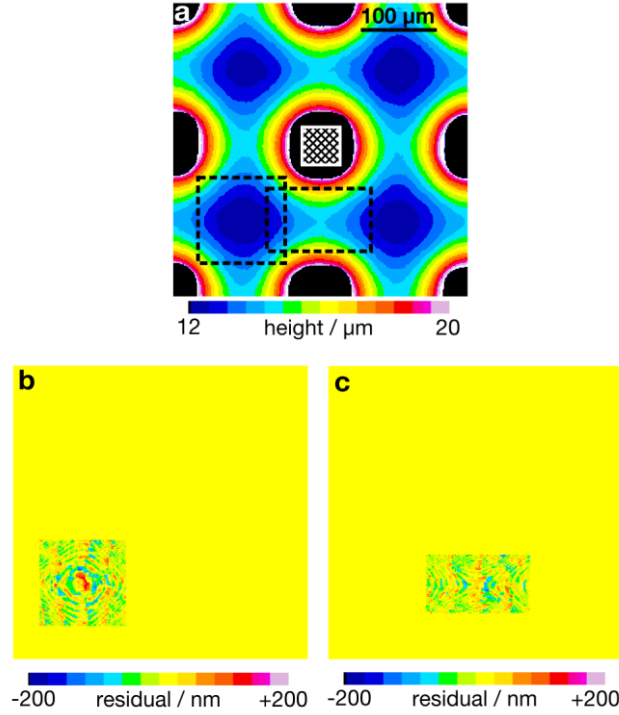
Figure S4.2: Calculation of the Laplace pressure of a drop deposited on an array of pillars. (a) Contour plot of the height h_{air} of the air cushion. The mean curvature H ($= 1/R$ for spherical drops) is equal at every position of the water-air interface, since a deformation of the drop due to gravity can be neglected. The areas enclosed in dashed rectangles are fitted with a function $h(x, y)$ that is the sum containing terms x^n, y^n, $x^n y^m$ up to the 6th order. The mean curvature is calculated at the center of each rectangle:

$$H = \frac{h_{xx}\left(1 + h_y{}^2\right) + h_{yy}\left(1 + h_x{}^2\right) - 2\,h_{xy}\,h_x\,h_y}{2\,(1 + h_x{}^2 + h_y{}^2)^{3/2}},$$

where h_{ij} denotes the partial derivative of h with respect to i, j. Evaluation of the curvature at the points of highest symmetry minimizes the error in the calculation. The curvatures calculated around the minimum and the saddle point are 0.87 ± 0.05 mm^{-1} and 0.79 ± 0.10 mm^{-1}, respectively. They are equal within the accuracy of the measurements. The fit around the minimum is used in all cases in the manuscript. (b) Residual of the fit around the minimum and (c) the saddle point.
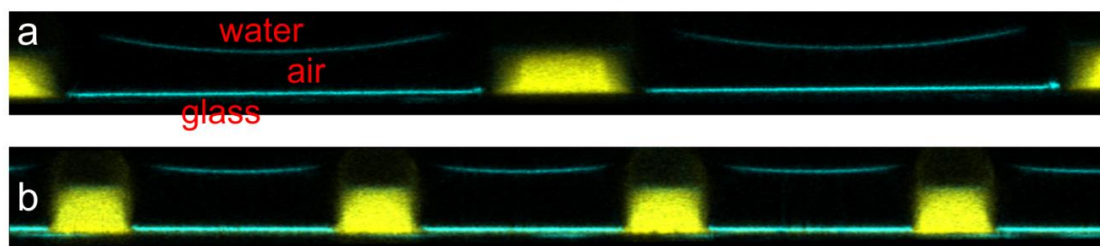
Figure S4.3: Index of refraction: Vertical images taken by laser scanning confocal microscopy of drops deposited on arrays of pillars. The reflection (cyan) and fluorescence of the PDMS pillars (yellow) are measured along the main axis: (a) a = 50 μm, d = 200 μm, h = 23 μm, (b) a = 25 μm, d = 100 μm, h = 23 μm. To accurately depict the height of the air cushions (n = 1.0) a dry objective was used. However, therefore the refractive index of objective did not match those of SU-8 (n = 1.6, data from MicroChem, Newton MA, USA). The pillars appear shorter by a factor of 1.6 i.e. they appear to have a height of about 15 μm. Refraction from the pillars defocus the laser beam and the reflection of light near the edge of the pillars, so the shape of the water-air cushion cannot be determined closer than 0.05 d from the pillars. Since the height of the pillars is known from SEM, we inserted artificial pillars to avoid confusion.

Movie S4.1: The movie is compiled of 2-dimensional images taken by laser scanning confocal microscopy. It shows vertical sections through an evaporating water drop deposited on PDMS pillars. The dimensions of the pillars are: diameter a = 20 μm, height h = 5 μm, and pillar-pillar distance d = 40 μm. the images are recorded at a frame rate of 1 frame/min. Fluorescent emission from water and PDMS is shown in cyan and yellow, respectively, and reflection in magenta. The sensitivity of the fluorescence detector was adjusted during the measurement to correct for the increasing dye concentration in water.

Movie S4.2: 3-dimensional movie showing the reflection of light from the SU-8-air and air-water (cyan) interface. A pillar is shown for comparison. The z-axis is 5× magnified for clarity. The distance between pillars is d = 200 μm and their height h = 23 μm.

Movie S4.3: Time resolved 3-dimensional movie of the depinning impalement transition. A drop was deposited on a pillar array. The same drop is viewed along the main axis (top) and the diagonal (bottom). Wetting of the substrate does not cause a jump of the rim. One 3-dimensional image was recorded every 0.9 s. The dimensions of the SU-8 pillars are: a = 5 μm, d = 20 μm, h = 5 μm. The z-axis is 10× magnified.

Movie S4.4: Roll-off of a 6 μL sized drop deposited on an array of SU-8 pillars. The dimensions of the SU-8 pillars are: a = 50 μm, d = 200 μm, h = 23 μm. The stage was tilted at a rate of 0.6 °/s.

Movie S4.5: Evolution of the rim of a drop and the impalement transition. The reflection of the water-air cushion interface (cyan), fluorescence from the pillars (yellow) and transmission (gray) are shown. After wetting of the substrate micrometer sized air bubbles are left at the backside of the pillars with respect to the flow direction. In course of time the size of the bubbles continuously decreased. After about 10 minutes the bubbles disappeared. Wetting of the substrate is accompanied by a jump of the rim. The dimensions of the SU-8 pillars are: a = 50 μm, d = 200 μm, h = 23 μm. Frame rate: 1.5 frames/s.

Movie S4.6: Droplets remain on top of pillars after depinning (top right). The dimensions of the SU-8 pillars are: a = 50 μm, d = 200 μm, h = 23 μm. Frame rate: 1.5 frames/s.

Movie S4.7: Contact angle measurement setup. The stage is tilted at a speed of 0.6°/s. Tilting the stage caused increasing deformations of the drop (6 μL) due to gravity. After tilting the stage by 17° the drop rolled-off from the micropillar array. The dimensions of the SU-8 pillars are: a = 5 μm, d = 20 μm, h = 23 μm. Since the glass slide is only partially covered with SU-8 pillars the drop sticks as soon as it left the microstructured surface.

5   FUNCTIONAL SUPERHYDROPHOBIC SURFACES MADE OF JANUS MICROPILLARS

Lena Mammen,[1] Karina Bley,[1] Periklis Papadopoulos,[1] Frank Schellenberger,[1] Noemí Encinas[1], Hans-Jürgen Butt,[1] Clemens K. Weiss,[1,2] and Doris Vollmer[1]

[1]Max Planck Institute for Polymer Research,

Ackermannweg 10, D-55128, Mainz (Germany)

[2]University of Applied Sciences Bingen,

Berlinstrasse 109, D-55411 Bingen, Germany

We demonstrate the fabrication of superhydrophobic surfaces consisting of micropillars with hydrophobic sidewalls and hydrophilic tops, referred to as Janus micropillars. Therefore we first coat a micropillar array with a mono- or bilayer of polymeric particles, and merge the particles together to shield the top faces while hydrophobizing the walls. After removing the polymer film, the top faces of the micropillar arrays can be selectively chemically functionalised with hydrophilic groups. The Janus arrays remain superhydrophobic even after functionalisation as verified by laser scanning confocal microscopy. The robustness of the superhydrophobic behaviour proves that the stability of the entrapped air cushion is determined by the forces acting at the rim of the micropillars. This insight should stimulate a new way of designing super liquid-repellent surfaces with tunable liquid adhesion. In particular, combining superhydrophobicity with the functionalisation of the top faces of the protrusions with hydrophilic groups may have exciting new applications, including high-density microarrays for high-throughput screening of bioactive molecules, cells, or enzymes or efficient water

condensation. However, so far chemical attachment of hydrophilic molecules has been accompanied with complete wetting of the surface underneath. The fabrication of superhydrophobic surfaces where the top faces of the protrusions can be selectively chemically post-functionalised with hydrophilic molecules, while retaining their superhydrophobic properties, is both promising and challenging.

5.1   INTRODUCTION

Controlling the wetting[162] of solid surfaces is of great interest in many fields, including microfluidics,[163],[164],[165] spray painting and coating,[166],[167] fog harvesting,[168] textile industry,[127] and the deposition of pesticides on plant leaves.[73] A step towards this goal has been the fabrication of superhydrophobic, superhydrophilic, and hydrophilic-superhydrophobic patterned surfaces.[73],[169],[170],[171] Superhydrophilicity can be achieved by a material with a rough surface topography and high surface energy.[172] Decreasing the surface energy can render the surface superhydrophobic. Superhydrophobicity is defined by an apparent contact angle of water with the surface above 150° and a roll-off angle below 10°[32],[72] for drops of approximately 10 μL volume. Water drops roll off with little friction. This low adhesion is caused by air trapped between the drop and the substrate. The superhydrophobic state must be distinguished from the "Wenzel state", in which the substrate is fully wetted by the liquid.[5]

Arrays of hydrophobic micropillars are models for superhydrophobic surfaces.[13],[72],[146],[149],[173] A drop of water placed on such an array is only in contact with the top faces of the micropillars. The equilibrium apparent contact angle, θ_{app}, of water on such surfaces has been calculated by minimizing the free energy of a drop assuming that the drop is in its global thermodynamic equilibrium. This assumption results in the Cassie-Baxter equation:[8] $\cos \theta_{app} = f (\cos \theta + 1) - 1$, where f is the fraction of the solid surface in contact with water and θ is the Young's contact angle on a flat surface of the same material. The Cassie-Baxter equation leads to the requirement of a low-energy surface, i.e. a hydrophobic surface. Therefore, it was unclear whether a selective chemical post-functionalisation of the top faces of superhydrophobic surfaces with hydrophilic molecules would be possible. Thus, the fabrication of superhydrophobic surfaces where the top face of each protrusion can be selectively chemically post-functionalised with hydrophilic molecules while retaining their superhydrophobic properties is both promising and challenging and has not been achieved yet.

Few strategies have been reported for creating hydrophilic spots with typical diameters of a few hundred microns on an otherwise superhydrophobic surface.[12],[170] These methods include microcontact or inkjet printing,[174] photomasking,[175] top-down lithography[176] and polymer deposition from solution.[177] Water drops are confined to these hydrophilic spots while also wetting the underlying substrate. Furthermore, these post treatments are often harsh (UV), produce large pattern sizes (photomasking or printing), or are accompanied by the dissolution of the hydrophilic molecules used for functionalisation (e.g., lipids, polymers) into the drop under investigation.[136] Varanasi fabricated micropatterned surfaces *via* microcontact printing using a polydimethylsiloxane stamp.[178] Part of the top faces can also be hydrophilized by evaporation or by pulling a drop over the surface. Depinning is accompanied by leaving tiny drops behind. If its mother drop contains non-volatile components these can alter the surface properties locally.[14]

Here, we introduce a method for the fabrication of transparent superhydrophobic micropillars with fluorinated hydrophobic sidewalls and functional hydrophilic silica tops, i.e., Janus micropillars. We functionalised the top of each micropillar by chemically binding molecules of different hydrophilicities. The micropillar arrays were highly transparent, which enabled us to use laser scanning confocal microscopy to verify the existence of air cushions that separated the substrate from water. We demonstrate that superhydrophobicity in the arrays of Janus micropillars is maintained and show that the stability of the air cushions is determined solely by the properties of the hydrophobic rim of each micropillar, not by the hydrophilicity or chemical nature of the top faces of the micropillars.

5.2 METHODS

FABRICATION OF SILICA-COATED SU-8 PILLARS

The flat-top cylindrical micropillars were fabricated by photolithography using a SU-8 photoresist and arranged on a glass slide in a square lattice.[179] The micropillars were fluorescently labelled by first mixing the photoresist with a hydrophobic N-(2,6-diisopropylphenyl)-3,4-perylenedicarboxylic acid monoimide (PMI) dye[180] at a concentration of 0.05 mg/mL. The substrates were coated with silica by treatment with an O_2 plasma for 30 s (at an O_2 flow rate of 7 sccm), followed by immersion in a solution of tetraethoxysilane (1.82 mL) and ammonium hydroxide (28 % in water, 4.2 mL) in ethanol (50 mL) for 2-3 h. Afterward, the substrates were rinsed with ethanol

and dried in a N_2 stream. Because SU-8 swells slightly in organic solvents, such as tetrahydrofuran, we observed some cracks in the silica shell after the washing step for PS removal (see below). These defects could be prevented by exposing the substrates to an O_2 plasma (at an O_2 flow rate of 7 sccm) for 1 h before decoration with the particles. The plasma penetrated the silica shell and removed an outer layer of SU-8, creating free space for swelling.

MONOLAYER CRYSTALLIZATION PROCEDURE

The PS particles were synthesised by soap-free emulsion polymerisation of styrene.[58] The average diameter of the spherical and almost monodisperse particles was 1.1 μm or 1.4 μm (SEM). Highly ordered particle monolayers were prepared by self-assembly at the air-water interface of a Langmuir trough (242 cm^2) using Milli-Q water (with a resistivity of 18.2 MΩcm) as a subphase. Prior to use, the micropillar substrates were exposed to an Ar plasma for 4 min (at an Ar flow rate of 5 sccm) to remove any adhering organic impurities and stored in ethanol. The substrates were immersed into the subphase and placed on a holder parallel to the air-water interface. The particle dispersion (1.5 wt% in ethanol) was added dropwise *via* a tilted glass slide that was partially immersed in the subphase. After 15 min, the monolayer was compressed at a speed of 2 cm/min until a compact monolayer formed. This result manifested as an increase of the simultaneously recorded pressure. Thereafter, the particles were deposited on the substrates by lowering the water level, i.e., a "surface-lowering transfer". The particle micropillar arrays were fabricated by exposing the particle-decorated micropillars to an O_2 plasma for 30 s (at an O_2 flow rate of 7 sccm) and then coated with a thin silica shell as previously described.

FABRICATION OF JANUS (PARTICLE) PILLARS

To form a film of PS particles, the particle-decorated micropillar arrays were exposed to toluene vapour for 1 h (to form Janus micropillars) or 40 min (to form Janus particle micropillars). The substrates were placed in a desiccator containing a vessel (with a 5 cm opening) filled with toluene. The substrates were then placed in a vacuum chamber to remove any solvent residues. After the sidewalls were hydrophobised (see below), the PS film was removed by thorough washing with THF, dichloromethane, methanol, ethanol, and Milli-Q water.

HYDROPHOBISATION

The micropillar sidewalls and micropillar arrays were hydrophobised using the chemical vapour deposition of 1*H*,1*H*,2*H*,2*H*-perfluorooctyldimethylchlorosilane.[181]

SPPS PROTOCOL FOR GALA SYNTHESIS

Fmoc-Lys(Mca)-OH, Fmoc-Lys-(Dnp)-OH, all Fmoc-protected ʟ-amino acids and preloaded resin (Fmoc-Gly-Wang resin, 100–200 mesh, loaded with 0.30 mmol/g of Gly) for SPPS were purchased by Novabiochem (Merck). The purity of the commercial amino acids was > 98 %. N-[(1H-Benzotriazol-1-yl)(dimethylamino)methylene]-N-methyl-methanaminium hexa-fluoro-phosphate N-oxide (HBTU, Novabiochem), ethyl cyanoglyoxylate- 2-oxime (Oxyma Pure, Merck, > 98 %), N,N-iisopropylethylamine (DIEA, Fluka, > 98 %), trifluoroacetic acid (TFA, Acros, 99 %), triisopropylsilane (TIS, Alfa Aesar, 99 %), N-methyl-2-pyrrolidone (NMP, BDH, 99 %), piperazine (Merck, > 99 %), fluorescein-5(6)-isothiocyanate (FITC, Sigma-Aldrich, > 90 %) and all solvents were used as received.

The peptide sequences were prepared using standard solidphase Fmoc chemistry with a microwave assisted automated peptide-synthesizer (Liberty, CEM). The parameters used for coupling and deprotection steps are mentioned below and relate to 0.1 mmol of peptide. Coupling was achieved under 300 s of microwave heating, with a temperature reaching and stabilizing at 75 °C after around 90 s, with Oxyma Pure as an activator (5 equivalents), DIEA as a base (10 equivalents) and amino acid (5 equivalents). Then a first deprotection stage of 30 s (temperature reaching around 50 °C at the end) followed by a second cycle for 180 s (temperature 75 °C) with a 20 wt% solution of piperazine in DMF was applied to remove the Fmoc protection group. The resin was washed 3 to 5 times between each coupling or deprotection step. Cleavage of peptide from the resin was performed using a mixture of TFA/TIS/H_2O (95 %/2.5 %/2.5 %) for 15 h at ambient temperature. After filtration, the peptides were precipitated and centrifuged three times in cold diethyl ether, and dried in a vacuum.

FUNCTIONALISATION WITH FITC OR GALA

The silica tops of the Janus micropillar arrays were amino-functionalised by dipping the substrate into a solution of aminopropyl-triethoxysilane (46 μL) in dry toluene (20 mL) for 1 h. The substrate was then rinsed with fresh toluene, dichloromethane,

and ethanol. The substrate was functionalised with FITC by immersion into a solution of FITC (39 mg) in acetone (10 mL) for 1.5 h, followed by thorough rinsing with fresh acetone, dichloromethane, and ethanol.[182] The silica tops were functionalised with the fluorescently labelled GALA peptide by being dipped overnight into a solution of dibenzylcyclooctyne-N-hydroxysuccinimide ester (DBCO-NHS ester, 0.1 mg/L) in dimethylsulphoxide (DMSO, 5 mL), followed by washing with fresh DMSO and Milli-Q water. The DBCO-modified substrate was then immersed overnight in a solution of azide-functionalised GALA (0.1 mg/L) in DMSO (5 mL), followed by thorough rinsing with fresh DMSO and Milli-Q water. The fluorescently labelled GALA was synthesised using standard Fmoc SPPS protocols using a CEM Liberty microwave-assisted solid phase peptide synthesiser. The FITC was introduced at the N-terminus of the peptide by Fmoc-Lys(FITC)-OH, which was synthesised following a protocol by Fuchs et al.[183] All of the other Fmoc-amino acids, including Fmoc-Lys(N_3)-OH, were commercially available. The identity of the peptide was confirmed using 1H-NMR (Bruker Avance 300), HPLC (Hewlett-Packard, Agilent), and MALDI-TOF-MS (Bruker-Daltonics).

INSTRUMENTS AND CHARACTERIZATION

The pillar arrays and particles were characterized by scanning electron microscopy (SEM) using a LEO 1530 Gemini instrument (Zeiss, Oberkochen, Germany) at low operating voltages (0.7-2 kV). The pillar arrays and their contact angles with water were imaged by inverted laser scanning confocal microscopy (LSCM, Leica, TCS SP5 II – STED CW) by applying glass substrates with a thickness of 170 μm. The LSCM has a horizontal resolution of about 250 nm and a vertical resolution of about 1μm. The spectral ranges could be freely varied, allowing the measurement of the emission from different dyes and the reflected light from the interfaces simultaneously. Water was labelled fluorescently with Alexa Fluor 488 at a concentration of 0.1 mg/mL. The dyes (PMI and Alexa Fluor 488) were excited using the Ar line at 488 nm). For treating the surfaces with Ar or O_2 plasma a FEMTO plasma cleaner was used (Diener electronic, power: 15 W). Contact angle measurements were performed with a contact angle meter (DataPhysics; OCA35). Static contact angles were measured depositing a liquid droplet of 4 μL on the surface. Advancing contact angles were measured using a sessile droplet of 4 μL, with the needle in it, and subsequently increasing the liquid volume at a rate of 0.5 μL/s. Roll-off and receding angles were measured depositing a droplet of 5 μL and tilting the substrate at a rate of 2°/s. They were determined in the moment when the droplet detaches from the first outermost pillar.

SURFACE AREA FRACTION IN THE NANO-CASSIE STATE

The structure is made of a square array of cylindrical pillars with diameter d, height h, and pitch P (Fig. 5.1). The particles have radius r and form a close-packed monolayer. Each particle occupies an area in the horizontal plane of $\approx 2\sqrt{3}r^2$. Thus the number of particles on top of one pillar is about $N_t = \pi d^2/(8\sqrt{3}r^2)$. Assuming that water forms a contact angle of $\theta = 120°$ with the surface of the nanoparticles, the area of each particle that is wetted is $A_1 = 2\pi r^2(1 + \cos\theta)$ at zero applied pressure.
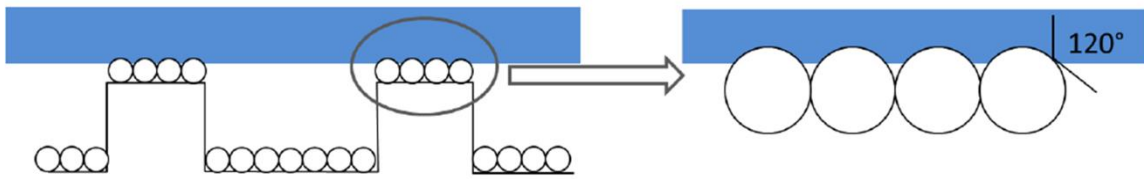
Figure 5.1:   Sketch of micropillars decorated with particles.

Considering a large water drop deposited on the surface, the wetted area per pillar is

$$A_w = N_t\, 2\pi r^2(1 + \cos\theta) = \pi d^2/(8\sqrt{3}r^2)\, 2\pi r^2(1 + \cos\theta) = \pi^2 d^2/(4\sqrt{3})\,(1 + \cos\theta).$$

$$(5.1)$$

The total area (of the substrate and liquid-air interface) per pillar is

$$A_t = P^2 - N_t\pi r^2 \sin^2\theta + A_w. \tag{5.2}$$

Thus the wetted area fraction for the Cassie-Baxter equation is

$$f = \frac{(\pi^2 d^2/4\sqrt{3})(1 + \cos\theta_m)}{P^2 - (\pi^2 d^2 \sin^2\theta/8\sqrt{3}) + (\pi d^2/4\sqrt{3})(1 + \cos\theta_m)} \approx \frac{\pi^2 d^2(1 + \cos\theta)}{P^2 4\sqrt{3}} \tag{5.3}$$

This fraction is independent of the size of particles.

5.3   RESULTS AND DISCUSSION

Flat-top cylindrical SU-8 micropillars with different diameters *d*, pitches *P*, heights *h*, and surface fractions were prepared on glass substrates using photolithography.[179] After the epoxy-based photoresist surface was treated with an O_2 plasma, a Stöber reaction[83],[181] was performed to coat the micropillars with an approximately 70 nm thick silica shell (Figs. 5.2a and 5.3a). The silica layer increased the mechanical stability of the micropillars. Some micropillar arrays were hydrophobized after coating with a silica shell (Fig. 5.2a). Most of the silica-coated micropillar arrays were decorated with a monolayer of hexagonally arranged polystyrene (PS) particles. These samples were either used to investigate the influence of the overhangs on the wetting properties (Figs. 5.2b, 5.3b and 5.4) or to protect the top face during the modification of the sidewalls (Figs. 5.2c and 5.3c). To coat the top faces of micropillars with particles the substrates were put into a Langmuir trough.[184] A drop of the dispersion was deposited at the air-water interface to induce the formation of a self-assembled monolayer of particles. Then, the water level was lowered, and the micropillar tops and bottoms were homogeneously decorated. This method can be applied to decorate small as well as large micropillars with a well-defined monolayer of particles. Only occasionally, a few particles can be found at the sidewalls. This can happen if the monolayer was compressed slightly too fast or too much (Fig. 5.4). The particles at the bottom of the substrates will not affect the wetting behaviour as long as the drop stays in the Cassie state. One part of the
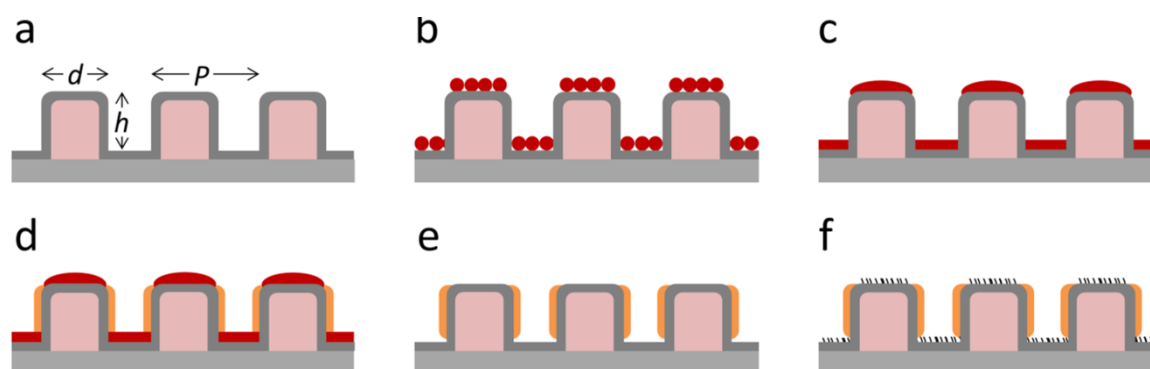
Figure 5.2: Concept: to fabricate functional Janus micropillar arrays, (a) the top faces of the micropillars were decorated with (b) one or more self-assembled monolayers of polymeric particles in a Langmuir trough. This covers and protects the top face after the particles were merged into a film by exposure to saturated toluene vapour (c), and the walls of the micropillars were chemically modified (d). After removing the protective polymer film (e) the top faces can be functionalized (f). The dimensions shown are not to scale.

particle pillars was hydrophobized and the remaining part was subsequently exposed to saturated toluene vapour. The adsorbed toluene softened the PS particles such that they formed a homogeneous film (Figs. 5.2c and 5.3c) that completely protected the micropillar tops while the sidewalls were hydrophobised with the semifluorinated silane 1*H*,1*H*,2*H*,2*H*-perfluorooctyldimethylchlorosilane to decrease the surface energy (Fig. 5.2d). The PS film was subsequently washed away, leaving the micropillars with hydrophobic sidewalls and hydrophilic top faces, which are known as Janus micropillars (Figs. 5.2e and 5.3d) The exposed silica surface of the micropillar tops could then be selectively modified either to precisely control the hydrophobic-hydrophilic characteristics or to enable the attachment of specific molecules (Fig. 5.2f).
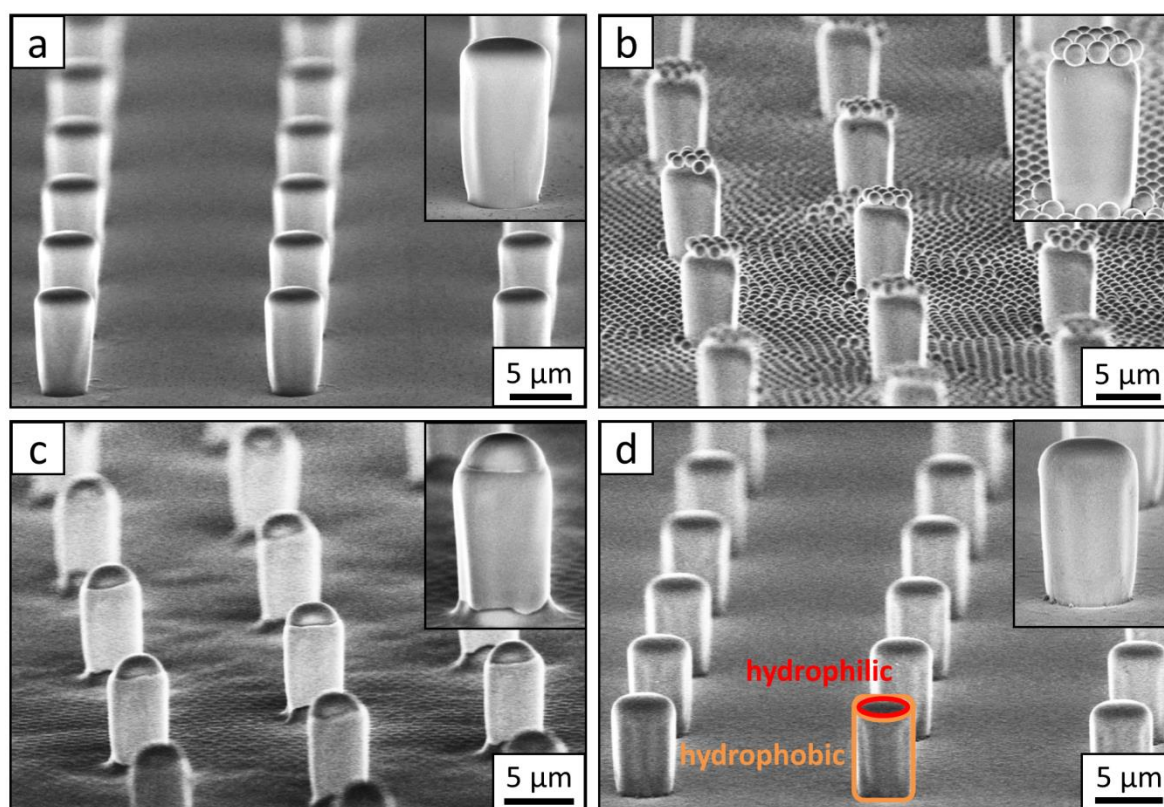
Figure 5.3: Scanning electron microscopy (SEM) images of a micropillar array after each step of the Janus micropillar fabrication technique. (a) Silica-coated SU-8 micropillars, (b) PS particle-decorated micropillars, (c) PS film-masked tops of micropillars and (d) Janus micropillars with hydrophilic silica tops (shown as a red-rimmed area). The insets show a pillar at higher magnification. The dimensions of the micropillars are d = 4 μm, P = 20 μm, h = 9 μm, and f = 3 %.

We first investigated the wetting behaviour of fully fluorinated micropillars with a smooth top surface (Fig. 5.3a, termed "P"), fully fluorinated micropillars coated with a monolayer of particles (Fig. 5.3b-c, termed "PP") and micropillars with a hydrophilic silicon oxide top surface and hydrophobic walls (Fig. 5.3d, termed "JP"). The flat-top (P) and particle-coated (PP) micropillar arrays with low surface fractions, f = 5-6 %, exhibited a roll-off angle, α, and hysteresis in the contact angle, $\Delta\theta = \theta_A - \theta_R$, that was less than or equal to 10° (Table 5.1). The apparent advancing contact angle, θ_A, was roughly the same for all surfaces, with a value of 155-159°. Low roll-off and high advancing and receding angles were better achieved with small structures. Micropillar arrays (P, PP) with higher surface fractions, f = 20-23 %, exhibited significantly higher roll-off angles and contact angle hysteresis, where α attained values up to 32° and $\Delta\theta$ attained values up to 27° (Table 5.2). However, the advancing angle remained always well above 150°.
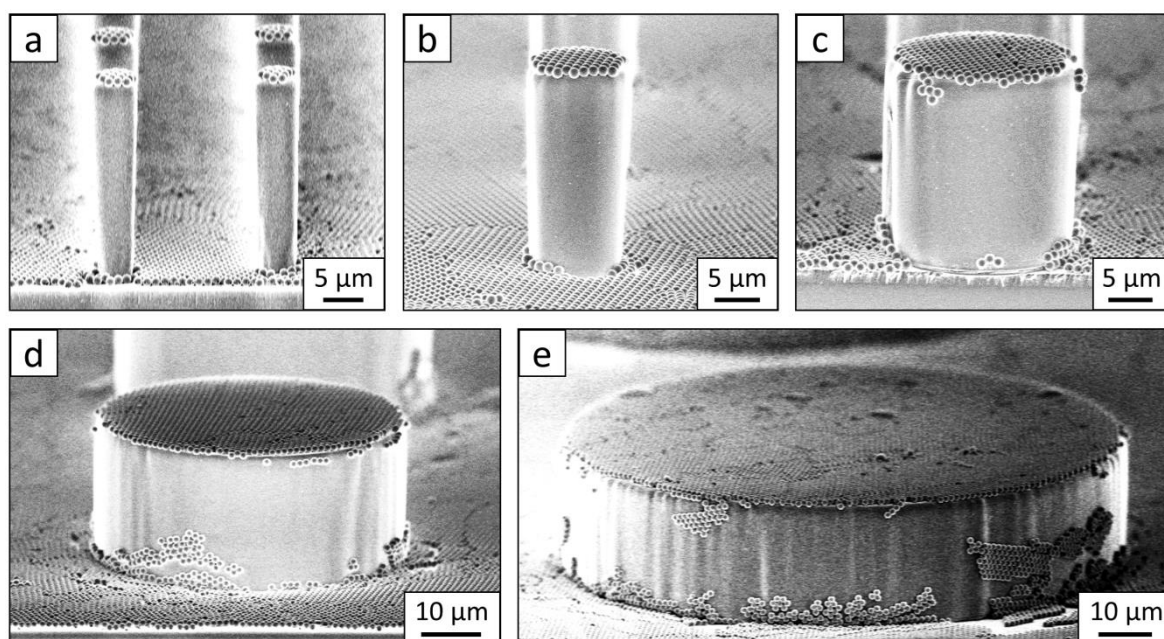
Figure 5.4:   SEM images of particle-coated micropillars of varying diameters: 6 μm (a), 11 μm (b), 22 μm (c), 53 μm (d), and 105 μm (e). The height of the micropillars is h = 23 μm.

To verify that despite the large roll-off angles the drops were still separated from the substrate by an air cushion, we imaged the drops using laser scanning confocal microscopy (LSCM).[179] For this purpose, we labelled the SU-8 micropillars with a hydrophobic perylene-monoimide-based fluorophore (PMI).[180] A water soluble perylene-diimide-based dye (WS-PDI) was added to the water phase. We

simultaneously recorded the light reflected from the interfaces. The superposition of the fluorescent (cyan and yellow) and reflection (red) images showed the morphology of the water–air and micropillar–air interfaces with a horizontal resolution of ≈ 250 nm and a vertical resolution of ≈ 1 μm. Indeed, the air cushion (black) separating the drop (cyan) and the substrate was clearly visible (Fig. 5.5a-c). The same result was found for the fully fluorinated micropillar arrays and the micropillar arrays with hydrophilic top surfaces (Fig. 5.8b). Notably, all drops were well separated from the substrate by an air cushion, proving that they remained in

Table 5.1: Comparison of the wetting behaviour of flat-top micropillar (P) and particle-coated micropillar (PP) arrays with low surface fraction f and of varying dimensions (i.e., diameter d and pitch P). Listed are the apparent advancing and receding contact angles, θ_A and θ_R, the hysteresis $\Delta\theta$, and the lateral and diagonal roll-off angles α and $\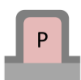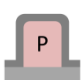alpha_D$. The height of the micropillars is h = 23 μm. The standard deviation was calculated from five independent measurements, each. The surface fraction of the particle-decorated micropillars was calculated according to eqn (5.3). For comparison we measured the apparent contact angles of an equally treated flat SU-8 surface after coating with a silica shell and hydrophobization; θ_A(flat) = 124° ± 2°, and θ_R(flat) = 85° ± 5°.

	$d/\mu m$	$P/\mu m$	f %	θ_A	θ_R	$\Delta\theta$	α	α_D
P	6	21	6	156° ± 1°	149° ± 1°	7°	6° ± 1°	5° ± 1°
PP	6	21	6	157° ± 1°	152° ± 1°	5°	4° ± 1°	4° ± 1°
P	11	41	6	157° ± 1°	148° ± 1°	9°	6° ± 1°	6° ± 1°
PP	11	41	5	156° ± 1°	150° ± 1°	6°	6° ± 1°	4° ± 1°
P	26	102	5	157° ± 2°	147° ± 2°	10°	9° ± 1°	9° ± 2°
PP	26	102	5	156° ± 1°	147° ± 1°	9°	8° ± 1°	7° ± 2°
P	54	208	5	155° ± 1°	145° ± 1°	10°	11° ± 2°	10° ± 2°
PP	54	208	5	157° ± 1°	148° ± 2°	9°	8° ± 2°	8° ± 1°

Table 5.1: Comparison of the wetting behaviour of flat-top micropillar (P) and particle-coated micropillar (PP) arrays with higher surface fraction f and of varying dimensions (i.e., diameter d and pitch P). Listed are the apparent advancing and receding contact angles, θ_A and θ_R, the hysteresis $\Delta\theta$, and the lateral and diagonal roll-off angles α and α_D. The height of the micropillars is h = 23 µm. The standard deviation was calculated from five independent measurements, each. The surface fraction of the particle-decorated micropillars was calculated according to eqn (5.3).

	d/µm	P/µm	f %	θ_A	θ_R	$\Delta\theta$	α	α_D
P	11	21	22	157° ± 1°	139° ± 1°	18°	20° ± 2°	19° ± 1°
PP	11	21	19	157° ± 1°	142° ± 1°	15°	15° ± 1°	14° ± 2°
P	22	41	23	156° ± 1°	139° ± 1°	17°	21° ± 2°	20° ± 1°
PP	22	41	23	157° ± 1°	142° ± 1°	15°	17° ± 1°	14° ± 1°
P	53	106	20	156° ± 1°	137° ± 2°	19°	23° ± 2°	21° ± 3°
PP	53	106	19	157° ± 2°	139° ± 2°	18°	21° ± 1°	18° ± 1°
P	105	207	20	155° ± 1°	128° ±2°	27°	32° ± 2°	29° ± 4°
PP	105	207	18	155° ± 1°	135° ± 1°	20°	24° ± 1°	19° ± 1°

the Cassie state (Tables 5.1 and 5.2). The "Cassie state" refers to a configuration in which the drop is separated from the substrate by an air cushion but the roll-off angle can exceed 10°.[8],[140] This verifies that the Cassie state does not necessarily correspond to superhydrophobic behaviour.

The additional particle layer on top of the micropillars reduced the roll-off angle and the contact angle hysteresis (Tables 5.1 and 5.2). We attribute this result to the overhangs formed by the spheres (Fig. 5.3b, inset), which should enhance superhydrophobicity.[33],[185] The overhangs produced a so-called "nano-Cassie state"[30] in which air was trapped between the micropillars ("micro-Cassie state")
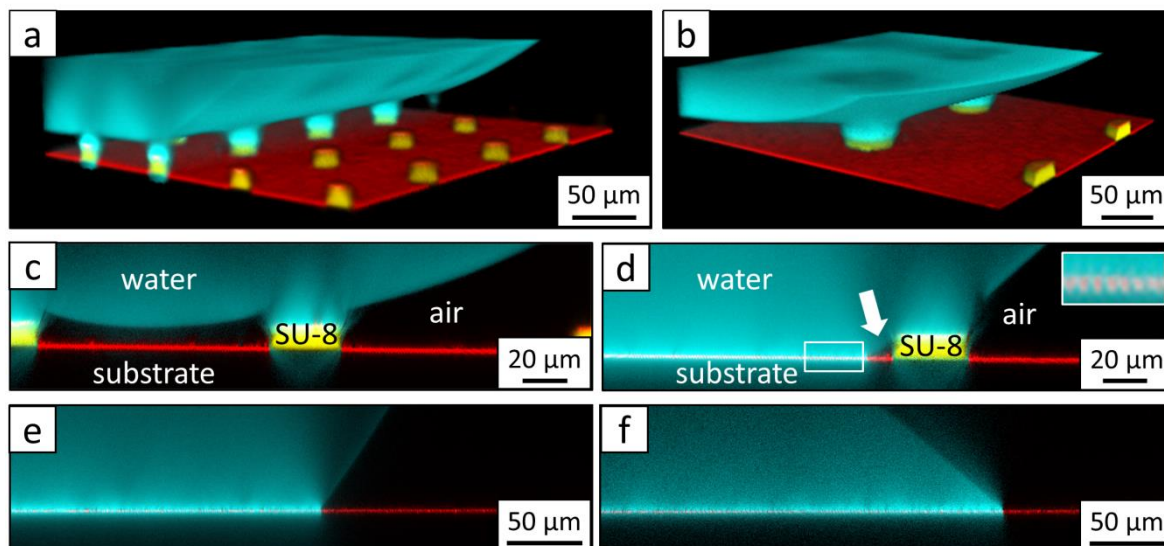
Figure 5.5: (a and b): 3D laser scanning confocal microscopy (LSCM) images of a sessile water drop (cyan) on particle micropillars (yellow) with (a) d = 26 μm and P = 102 μm and (b) d = 54 μm and P = 208 μm; both water and SU-8 micropillars were dyed, where the emission wavelengths of the dyes were well separated to enable simultaneous detection; the water-soluble perylene-diimide-based dye (WS-PDI) was not interfacially active,[141] and the light reflected at the substrate-air interface (red) was simultaneously recorded. The 3D images were obtained by superposing the fluorescence and reflection images; (c and d): vertical section through a water drop resting on an array of particle micropillars (d = 54 μm and P = 208 μm) (c) in the micro- and nano-Cassie states and (d) in the micro-Wenzel and nano-Cassie states. A small air bubble remained at the side of the pillar (d, white arrow); the inset in d (white square) illustrates that the "nano-air pockets" (red spots) were stable even in the micro-Wenzel state; red: reflected light at the air-glass and air-SU-8 interface; white: reflections at the glass-water interface; the reflective indices are as follows: n_{air} = 1.0, n_{water} = 1.33, n_{glass} = 1.46, and n_{SU-8} = 1.6.

and in the interstitials of the particles. This nano-air layer could be imaged by recording the reflection of light from the water-air interface (red line and spots in Fig. 5.5d-f). To test whether the nano-air layer is also stable for a pure particle layer on a glass substrate we measured the reflected light for an advancing and receding drop; θ_A (monolayer) = 125° ± 1°, θ_R (monolayer) = 39° ± 3°. In both cases the nano-air layer remained stable (Fig. 5.5e-f). For the particle-coated micropillar arrays a hierarchy of Cassie states was observed. The nano-Cassie state remained stable even after the drop was forced into the "micro-Wenzel state" (Fig. 5.5d). The transition to the micro-Wenzel state was caused by an evaporation-induced increase in the Laplace pressure. The particle layer on top of the pillars locally induced a nano-Cassie state which reduced line pinning. This resulted in the increase in the receding contact

angle, θ_R, of up to 7° and a decrease in the roll-off angle, α, of up to 10° (Tables 5.1 and 5.2).

The hydrophilic tops of the micropillars did not significantly affect the advancing contact angle, whereas the receding angle varied. The apparent advancing contact angle did not depend on the surface chemistry of the top faces of the micropillars. This result demonstrates that the apparent advancing contact angle was determined by contact line pinning at the sides of the micropillars, in accordance with the Gibbs criterion[154] (Fig. 5.6a).
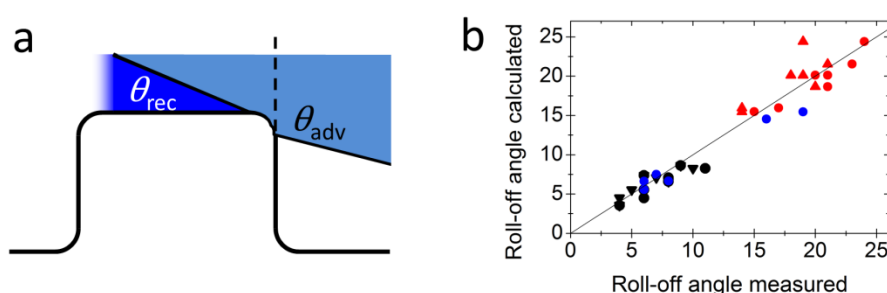
Figure 5.6:   Roll-off angles: (a) schematic of the water deposition on a micropillar, (b) comparison of experimentally determined roll-off angles and roll-off angles calculated using the El-Sherbini equation; black triangles: P, f = 3-6 %, black spheres: PP, f = 20-23 %, blue spheres: P, f = 3-6 %, red triangles: JPP, f = 3-6 %, and red spheres: JP, f = 3-6 % (Tables 5.1-3); the black symbols indicate superhydrophobic surfaces, and the red symbols indicate surfaces in the Cassie state.

In contrast, the apparent receding contact angle depended on the surface chemistry and the shape of the three-phase contact line of the micropillars. On the receding side, the three-phase contact line had to slide over the top face of a micropillar, which was hindered on a hydrophilic surface relative to a hydrophobic surface. Therefore, the contact angle hysteresis increased with the area fraction and the hydrophilicity of the micropillars.

To further support the hypothesis that the force per unit line rather than thermodynamics determined the macroscopic wetting behaviour, we related the contact angle hysteresis to the observed roll-off angles. The roll-off angle was obtained by balancing the surface tension force around the periphery of the drop with the gravitational force, $\rho g V \sin \alpha$. Here, ρ is the density of the liquid, g = 9.81 m/s², and V is the volume of the drop. This force balance yields $\rho V g \sin \alpha = k \gamma w \, (\cos \theta_R -$

$cos\ \theta_A$)[179], where w is the width of the apparent contact area. The width for such high contact angles is difficult to observe in a sliding experiment. Therefore, we calculated the width from the droplet volume and the receding contact angle. For small drops that have a spherical cap shape, geometrical considerations yield $w = (24V/\pi\beta)^{1/3} sin\ \theta$ with $\beta = (1 - \cos\theta)^2(2 + \cos\theta)$.[186] The constant k depends on the precise shape of the droplet just before it begins to slide. Values of k between $4/\pi$ and 2.0 have been reported for flat surfaces.[186],[187] The observed value of $k = 2.0$ (Fig. 5.6b) indicates that each individual micropillar exhibited strong contact line hysteresis[132], probably because of the formation of liquid microbridges.[179],[188] The hysteresis was only low at a macroscopic scale.
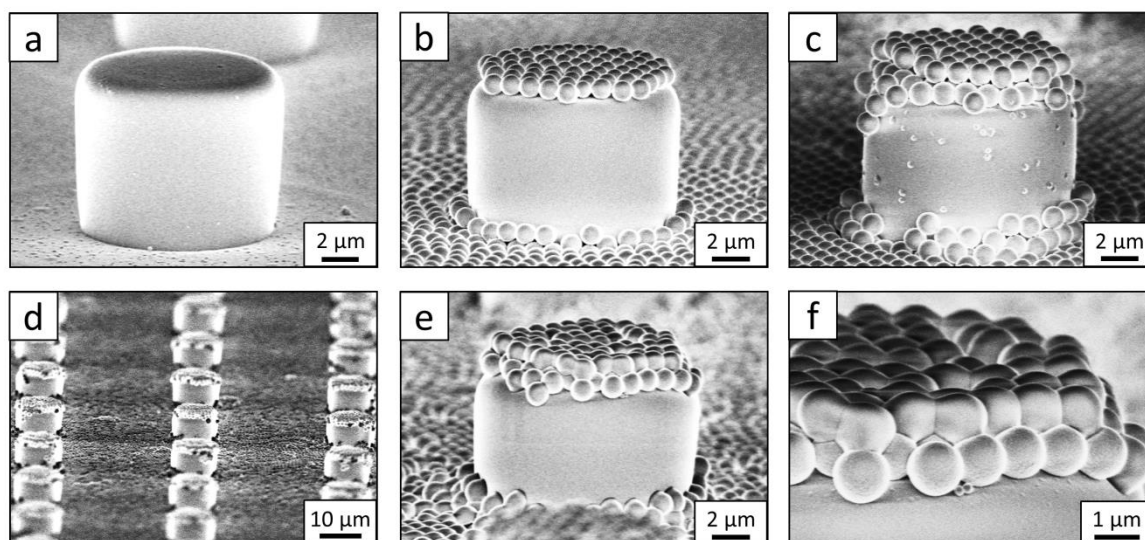
Figure 5.7: SEM images of silica-coated SU-8 micropillars. (a) Silica-coated SU-8 micropillar, (b) particle micropillar, (c-f) particle micropillars that are decorated with an additional layer of PS particles before (c) and after (d-f) exposure to toluene vapour (dimensions: d = 11 μm, P = 40 μm, and h = 9 μm).

So far, we have shown two functions of the particle layer: on the one hand, polymeric particles can be merged together to shield the top faces of the pillars while hydrophobising the walls. On the other hand the particles induce overhangs and thereby increase the stability of the Cassie state. Aiming to combine both functions, we proceeded as follows: first, a monolayer of PS particles was deposited onto the micropillar arrays. Next, the particle-decorated micropillars were coated with a silica shell (Fig. 5.7a and b). This prevents swelling of the PS particles during further treatment. Then, a second monolayer of PS particles was deposited on top of the
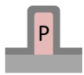
micropillars (Fig. 5.7c). The pillar arrays, now decorated with two layers of particles, were exposed to toluene vapour. This induced film formation of the topmost particle layer while the underlying layer could not swell due to its coating with a silica shell (Fig. 5.7d-f). After the sidewalls were hydrophobized the PS film was removed by thorough washing with different solvents resulting in Janus particle-covered micropillars with silica top faces. The increased stability of the Cassie state was reflected in the decreased roll-off angle and the increased contact angles (Tables 5.1 and 5.2). To increase the robustness of the Cassie state, it was important that the hydrophilic domain did not extend beyond the rim of the micropillar but was well restricted to its top face.
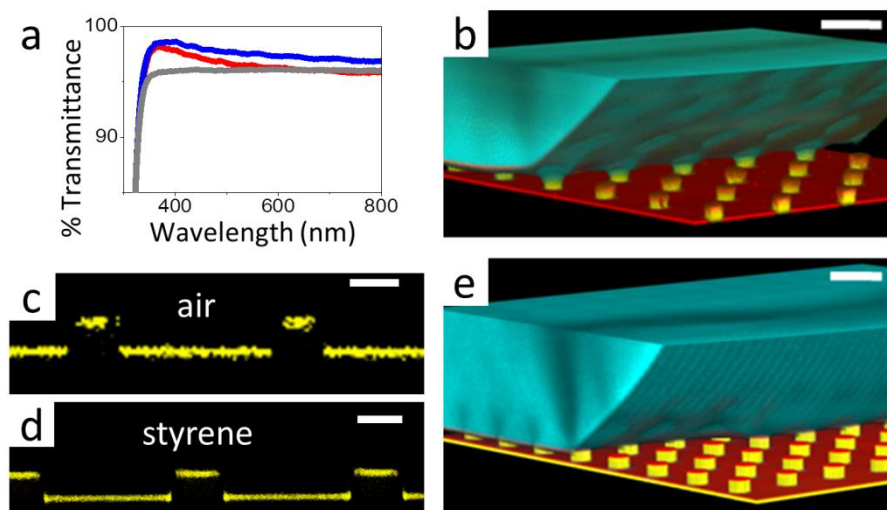
Figure 5.8: Functionalised micropillar arrays. (a) Transmittance spectra of Janus micropillars (blue line: Janus micropillars with d = 4 µm, red line: Janus micropillars with d = 11 µm, and grey line: bare glass substrate). Enhanced light transmission, particularly at short wavelengths, was caused by reduced reflectivity;[55] (b) 3D LSCM image showing a sessile water drop deposited onto Janus micropillars (d = 11 µm, P = 40 µm, and h = 9 µm); the silica micropillar tops were selectively functionalised with (c) the fluorescently labelled peptide, GALA, and (d and e) fluorescein-5-isocyanate (FITC), as verified by LSCM in fluorescence mode (c and d); the FITC-modified micropillars were wetted with styrene to minimise reflections at the substrate surface. (e) The functionalised substrates remained in the Cassie state; white scale bars: 20 µm.

To demonstrate that the silica top faces of can be chemically functionalised by hydrophilic molecules (Fig. 5.2f), we functionalised the tops of the micropillars with the fluorophore fluorescein-5-isothiocyanate (FITC) and a fluorescently labelled 30-

Table 5.2: Wetting properties of pillar (P), Janus pillar (JP), particle pillar (PP) and Janus particle pillar (JPP) arrays of different dimensions (h = 9 μm).

Sample	d / μm	P / μm	f %	θ_{ST}	θ_A	θ_R	$\Delta\theta$	α
P	4	20	3	155° ± 1°	159° ± 1°	151° ± 2°	8°	6° ± 2°
JP	4	20	3	153° ± 1°	156° ± 1°	148° ± 1°	8°	8° ± 1°
P	11	40	6	154° ± 1°	159° ± 1°	149° ± 1°	10°	7° ± 1°
JP	11	40	6	150° ± 1°	156° ± 1°	141° ± 1°	15°	19° ± 1°
PP	11	40	5	155° ± 1°	158° ± 1°	149° ± 1°	9°	6° ± 1°
JPP	11	40	-	151° ± 1°	157° ± 1°	142° ± 2°	15°	16° ± 2°

amino-acid-long synthetic peptide with a glutamic acid-alanine-leucine-alanine (GALA) repeat that has been developed for drug and gene delivery.[189],[190] In both cases, the silica top surface was first functionalised with amino-propyl-triethoxysilane. FITC was directly bound to the amine groups.[182] The GALA repeat was attached using a strategy based on azide-alkyne click chemistry. The amine groups were first coupled to the active ester dibenzylcyclooctyne-*N*-hydroxysuccinimide (DBCO-NHS ester). Then, the fluorescently labelled GALA, equipped with an azide group, was introduced during the synthesis using azido-*ε*-lysine and was bound to the DBCO-modified surface. UV-Vis spectroscopy of the Janus micropillar arrays on glass slides revealed excellent transparency that exceeded even that of a bare glass substrate (Fig. 5.8a). The hydrophilisation of the top faces did not change the advancing contact angle within experimental accuracy (Table 5.3). However, the receding contact angle slightly decreased and the roll-off angle increased, hinting towards increased adhesion. The 3D laser scanning confocal microscopy images demonstrated that a sessile water drop deposited onto an array of Janus micropillars remained in the Cassie state (Fig. 5.8b). The fluorescence images indicate that no GALA (Fig. 5.8c) or FITC molecules (Fig. 5.8d) were attached to the micropillar sidewalls. In contrast, strong fluorescence was observed at the top faces of the micropillars and at the bottom of the substrate. To ensure that the detected

light was not based on reflections at the solid-air interface, we wetted the FITC-modified Janus micropillars with styrene. The refractive indices of styrene ($n_{styrene}$ = 1.55) and SU-8 (n_{SU-8} = 1.6) are well matched. Hence, the detected light originated solely from the emissions of the attached FITC molecules (Fig. 5.8d). The deposited water drop remained in the Cassie state proving the robustness of the Cassie state after chemical modification of the top faces (Fig. 5.8e).

5.4   CONCLUSIONS AND COMMENTS

The apparent advancing contact angle of water and the stability of the Cassie state are determined by the walls of the micropillars, and not by the top faces. The apparent receding contact angle decreases when the top faces are hydrophilised, due to increased pinning of the receding contact line. To increase the receding contact angle, mono- and bilayers of particles were deposited on top of the micropillars. These particles induce a nano-Cassie state and facilitate the sliding of the receding edge of a water drop by breaking the contact line.

This decoupling of the apparent advancing and receding contact angles enables the fabrication of macroscopically superhydrophobic arrays of micropillars with locally hydrophilic silica top surfaces. The silica top surface of the micropillars allows for facile and versatile functionalisation by a variety of different coupling chemistries. The results offer new perspectives in surface-tension-confined microfluidics,[163],[169],[171],[191] cell-water condensation,[192] slip reduction,[193],[194] or drop impact.[195],[196] Here, we design superhydrophobic microarrays with up to 250 000 hydrophilic spots per square centimetre. The diameters of the hydrophilic spots of the Janus micropillars are in the size range of the cell diameters; therefore, the developed strategy has potential applications, e.g., a cell or single bacteria could be attached and immobilised on the top of each micropillar to investigate cell-cell communication, cell growth and proliferation.[197] Notably, the observation that hydrophilic top surfaces do not affect the robustness of the Cassie state implies that the Cassie state corresponds to remarkable damage tolerance. This result explains why superhydrophobic surfaces that are exposed to strong friction still can exhibit high contact angles.[198]

5.5   ACKNOWLEDGEMENTS

6   TRANSPARENT AND AIRTIGHT SILICA NANO- AND MICROCHANNELS WITH UNIFORM TUBULAR CROSS-SECTION

Lena Mammen*, Periklis Papadopoulos*, Kathrin Friedemann, Stefanie Wanka, Daniel Crespy, Doris Vollmer*, and Hans-Jürgen Butt*

Max Planck Institute for Polymer Research,

Ackermannweg 10, D-55128, Mainz (Germany)

Experimental results on a template-assisted technique to fabricate uniform nano- and microchannels are presented. Different template materials, polystyrene and poly(vinyl alcohol) electrospun and spider silk fibres were coated with silica. After calcination mechanically stable and transparent channels with uniform tubular diameter were obtained. The diameters ranged between 150 nm and 4 μm, depending on the size of the fibre template. By coating crossed fibres we prepared connected channel junctions that were solvent- and airtight. The channels and junctions remained tight even when applying a pressure above 3 bar as verified by laser scanning confocal microscopy. The flow of liquids in the channels was monitored and described by the Lucas-Washburn equation. We varied the viscosities and surface tensions of the liquids and measured the filling velocities over a distance of several millimeters as well as very close to the channel entrance. The late stage of capillary filling can be well-described by the Lucas-Washburn equation. The early stage was slower than predicted. We attribute the delayed filling to the velocity dependence of the contact angle and modeled the filling behaviour by dynamic wetting theories.

6.1   INTRODUCTION

Nano- and microchannels are widely used for controlled and targeted material transport. Applications include   fluidic delivery systems, cell and particle separation[199], drug release[200] and sensing (gas- and biosensors). For many applications it is sufficient or even desirable to have channels of few 10 μm in diameter. To miniaturize microfluidic devices, well-defined channels of sub-1 μm diameters are desirable. In particular, cylindrical airtight channels are essential for fundamental studies of capillary filling, diffusion, or transport phenomena.[65],[66],[201] Various techniques are used to prepare continuous tubular nano- and microchannels[202], such as coaxial electrospinning[203],[204],[205],[206], template-assisted methods[207],[208],[209],[210],[211]   including template wetting[212], chemical vapour deposition[213],[214], or mechanical pulling[215]. These methods expanded the ability to produce nano- and microchannels of different sizes and from different materials and allowed fundamental studies of flow in confinement.[216] However, it is still challenging to fabricate nanochannels with a defined, homogeneous diameter in an efficient and scalable process without compromising tightness. Coaxial electrospinning allows fabrication of microchannels in a continuous process. However, achieving a controlled and constant diameter and wall thickness over the entire length is demanding.[217],[218] Problems include breakup of the jet, instability of the core, porous walls, and varying cross-sections along the channel. In template-assisted wetting of porous material, e.g. porous alumina, by polymer melts or polymer solutions the length of the channels is limited to a few 100 μm. Complete filling of the tubes forms another problem.[212]

Nano- and microfluidic channels should be (1) tight, to avoid leakage and evaporation; (2) uniform in diameter over the entire length, to have a uniform flow velocity and pressure gradient and be able to quantify flow; (3) solvent-resistant; (4) transparent, to be able to observe transport. Here, a simple template-assisted method to fabricate well-defined silica nanochannels is presented, focusing on channels with a diameter between 150 nm and a few μm. To demonstrate the general applicability of the method, we coated electrospun polymer (Fig. 6.1) and natural spider silk fibres (Fig. 6.2) with silica. After thermally removing the template, solvent- and airtight channels and channel junctions are obtained. The tightness of the channels and junctions was proved with confocal miscroscopy by combining the transmission, reflection and fluorescence mode. Besides, we monitored the filling kinetics of liquids with different surface tensions and viscosities and compared it to theory. The transparency, tightness, and well-defined diameter make the channels well-suited model systems to investigate the flow in nano- and microchannels. Here, we focused

on the origin of the initial deviations of the filling velocities from the Lucas-Washburn equation.   It is still under debate whether these deviations result from prewetting,[219],[220] a velocity dependent contact angle,[216] inertial effects,[219] or turbulence[221] To gain further insight we varied the channel diameter and used different solvents. Our data support that the initial deviations can be attributed to a velocity dependent contact angle. This was verified by modeling the velocity dependence of the contact angle by molecular-dynamics and hydrodynamic theory.

6.2   MATERIALS AND METHODS

MATERIALS

Poly(vinyl alcohol) (PVA) (M_w = 125 kg/mol, 88 mol% hydrolysis) was purchased from Polysciences Inc. Polystyrene (PS) (M_w = 250 kg/mol), tetraethoxysilane (TEOS) (98 %) and castor oil were purchased from Acros Organics, tetrahydrofuran (THF) (99.9 %) and ammonium hydroxide (28 % in water) from VWR International, dimethylformamide   (DMF)   (p.a.)   from   Fluka,   (1H,1H,2H,2H)-perfluorooctyltrichlorosilane, ethanol absolute and isopropanol from Sigma Aldrich, glycerol from Carl Roth, and Alexa Fluor 488 from Life Technologies. N-(2,6-diisopropylphenyl)-3,4-perylenedicarboxylic acid monoimide (PMI) was prepared according to the literature.[180] All chemicals were used as received. Milli-Q water was obtained from a Millipore purification system operating at 18.2 MΩ.

INSTRUMENTS AND CHARACTERIZATION

The morphology and diameters of the fibres and channels were characterized by scanning electron microscopy (SEM) using a LEO 1530 Gemini instrument (Zeiss, Oberkochen, Germany) at low operating voltages (0.4-3 kV). The surface morphology was analyzed by scanning force microscopy with a VEECO Dimension 3100. The filling velocities were imaged by confocal laser scanning microscopy (CLSM, Leica, TCS SP5 II - STED CW) at a temperature of 23 ± 1 °C and relative humidity of 30 ± 5 % applying glass or quartz substrates with a thickness of 170 μm or 200 μm, respectively. Castor oil was fluorescently labelled with PMI, water and glycerol with Alexa Fluor 488 at a concentration of 0.01 g/mL, respectively. The surface tension of castor oil was measured following the Wilhelmy plate method, using a platinum plate cleaned with a Bunsen burner, with a DCAT11 tensiometer (DataPhysics Instruments

GmbH). The dynamic viscosities of castor oil and the aqueous glycerol solutions were determined with a micro Ubbelohde viscometer. All other values were taken from literature. For treating the surfaces with oxygen plasma a FEMTO plasma cleaner was used (Diener electronic, Power: 10 W, oxygen flow rate: 0.5 sccm). The indium tin oxide (ITO) layer was sputtered with an Edwards Auto 500 thermal sputter coater.

ELECTROSPINNING OF POLY(VINYL ALCOHOL) AND POLYSTYRENE FIBRES

For this work poly(vinyl alcohol) (PVA) nanofibres (Fig. 6.1a-b) and polystyrene (PS) microfibres (Fig. 6.1c-d) were produced. The PVA solution was prepared by dissolving 100 g/L PVA in water and stirring the solution at 85 °C until PVA completely dissolved. The fibres were electrospun by employing a constant flow rate of 2 µL/min (Harvard Apparatus PHD 2000 syringe pump), a voltage of +10 kV and a tip-collector distance of 13.7 cm (tip ID: 0.5 mm) with a commercial platform (Electrospin Cabin Dual Voltage, IME Technologies). PS fibres were produced with the same set-up from solutions of PS in THF or THF/DMF mixtures (1:1; w:w), with a concentration of 235 g/L and 242 g/L, respectively. The solutions were fed at a flow rate of 5 µL/min. Fibres were obtained by applying a voltage of +25 kV and a tip-collector distance of 12.2 cm. All fibres were directly electrospun on glass slides or silicon wafers. To avoid a detachment of the PS fibres they were fixed to the substrate by coating them with a thin silica shell (20-30 nm) by chemical vapour deposition of TEOS.[59],[60] Therefore, the PS fibre-coated substrates (glass or silicon) were placed in a desiccator for 24 h
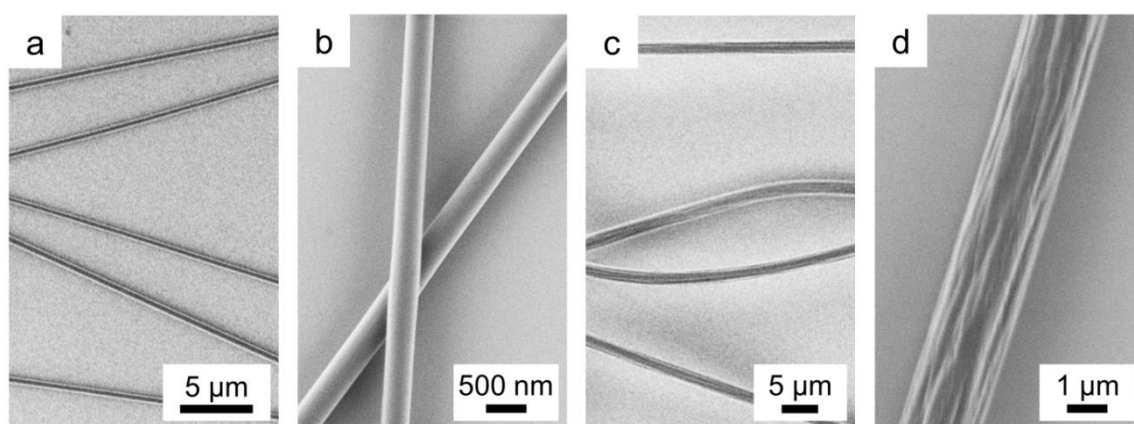
Figure 6.1: a) - c) Electrospun polymer fibres: Poly(vinyl alcohol) (PVA) nanofibres with an average diameter of (a) 180 nm and (b) 380 nm. c), d) Polystyrene microfibre with an average diameter of 2 µm.

together with two open glass vessels containing 1 mL of TEOS and 1 mL of aqueous ammonia (28 %), respectively.

Spider silk templates

The spider silk fibres were drawn mechanically from the abdominal spinnerets of immobilized but fully awake orb-weaver spiders using an apparatus similar to those of Vollrath *et al.*[222]. They were separated into the single strands (Fig. 6.2b-c) under an optical microscope. The single strands of major ampullate (dragline) or minor ampullate silk were then wrapped around a glass or silicon slide. To avoid rupturing of the strands by the sharp edges of the glass or quartz slides, the edges were coated by PS making use of dip coating.
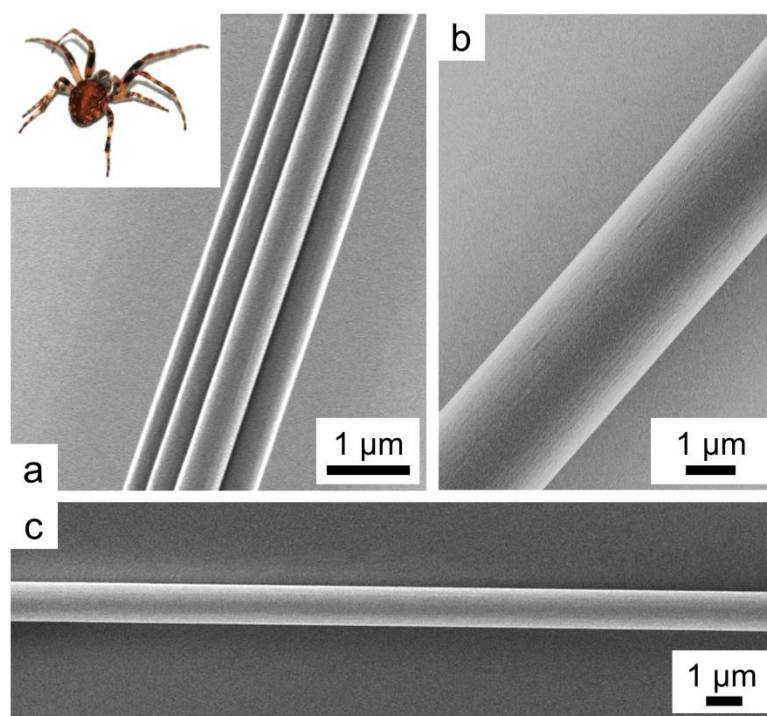
Figure 6.2: a) A spider silk fibre consists of several strands which can be separated under an optical microscope into single strands (b) and (c) (2.6 μm and 1.1 μm average diameter, respectively). The silk fibre (a, 1.6 μm average diameter) was drawn mechanically from a walnut orb-weaver spider (Nuctenea umbratica, a, inset).

TEMPLATE-ASSISTED FABRICATION OF SILICA CHANNELS

The electrospun fibres were treated with a weak oxygen plasma (FEMTO plasma cleaner, Diener electronic, Power: 10 W, oxygen flow rate: 0.5 sccm) for 30 s directly before coating them with silica. The spider silk strands were immersed in pure ethanol for 20 min before adding the reactants, since spider silk swells slightly in ethanol. The fibre templates which were deposited onto a silicon or silica substrate were placed slantly into the reaction vessel. The fibre-covered side was facing downwards to avoid sedimentation of silica colloids onto the surface which are formed as byproduct during the coating reaction. The spider silk strands were immersed in pure ethanol for 20 min before adding the reactants since they might swell slightly in ethanol. A solution of ethanol (50 mL), aqueous ammonia solution (4.2 mL) and TEOS (1.82 mL) was added and the reaction vessel was slowly agitated on a laboratory shaker (150 rpm) for 2 h. For the coating of the PVA fibres isopropanol was used instead of ethanol. The coating step was repeated and the substrates were cleaned with fresh ethanol (isopropanol in case of the PVA fibres) after each coating step to remove the formed silica colloids. All silica-coated fibres were calcinated for 2 h at 500 °C to remove the organic template material. To prevent crack formation a very low heating rate was applied (0.36 °C/min).

HYDROPHOBIZATION

To hydrophobize the outer channel wall and the substrate surface chemical vapour deposition of (1H,1H,2H,2H)-perfluorooctyltrichlorosilane (100 µL) was performed in a desiccator for 1 h in vacuum.[58],[60] Subsequently, the substrates were left in vacuum overnight to remove unreacted residuals.

6.3   RESULTS AND DISCUSSION

The silica nano- and microchannels were fabricated with a template-assisted technique. As templates we used either artificial electrospun polymer, poly(vinyl alcohol) (PVA) or polystyrene (PS), fibres (Fig. 6.1) or natural spider silk threads from orb-weaver spiders (Fig. 6.2). Electrospinning is a simple and versatile technique to fabricate long polymer fibres with diameters ranging from tens of nanometres to a few micrometres in a continuous process.[223],[224],[225] The diameters of the PVA nanofibres and PS microfibres that were prepared for this work ranged

from 150 nm to 500 nm and from 0.9 μm to 3.8 μm, respectively. Spider silk fibres have a very smooth surface topography (Fig. 6.2b) and an extremely uniform diameter, ranging from 0.2 to 10 μm, varying no more than 10 % within a total length of a few meters (Fig. 6.2c). Orb-weaver spiders have several spinneret glands that are located at their abdomen. Their silk fibres generally consist of several single strands (Fig. 6.2a). The fibres were drawn mechanically from the abdominal spinnerets and were separated into the single strands by monitoring them under an optical microscope. The diameter of the single strands that were used in this work varied between 500 nm and 2.6 μm depending on the type of silk or spider species. Due to the high tensile strength of the strands (several GPa)[222] they could be easily aligned onto a glass substrate.

For the silica coating of the fibres a modified Stöber synthesis[83] was applied. The fibres that were deposited onto a glass or silicon substrate were dipped twice for two hours into a mixture of TEOS (3.8 wt%) and aqueous ammonia (8.4 wt%) in ethanol. Since PVA is slightly soluble in ethanol the coating reaction was performed in isopropanol instead. Whereas the spider silk strands and PVA fibres adhered well to the glass or silicon substrate the PS fibres partially detached or rearranged during the coating. To avoid this they can be fixed to the substrate by coating them with a thin silica shell (20-30 nm) in vapour phase by chemical vapour deposition of TEOS[59],[60] before dipping them into the reaction mixture. To achieve a homogeneous nucleation of silica onto the fibre surface the PVA and PS fibres were treated with a weak oxygen plasma to create superficial hydrophilic groups and to decrease the activation energy for nucleation (Figs. 6.3-4). Without previous surface treatment a more heterogeneous nucleation causes a nanoporous and rough silica coating of the PVA fibres (Fig. 6.3d) whereas almost no silica nucleated onto the polystyrene fibres (Fig. 6.4d). For the spider strands no surface modification is required in spite of the partially hydrophobic character of the silk (Fig. 6.5).[226] Spider silk has a skin-core structure with two thin layers on top of the skin.[227] The outer lipid layer (10-20 nm thick) is only loosely connected to the inward material. It is probably removed during the coating reaction. The inner layer (40-100 nm thick) is attached more tightly and consists of glycoproteins which may facilitate nucleation of silica on its surface. The thickness of the silica shell depends on the composition of the Stöber solution, the number of dipping cycles and on the template material. Under identical reaction conditions the silica shell grew to an average thickness of 175 nm on oxygen plasma treated PVA fibres (Fig. 6.3b) and to an average thickness of 120 nm on oxygen plasma treated PS fibres (Fig. 6.4b). On a spider silk thread the wall thickness varied between 120 and 170 nm (Fig. 6.5b,d). We assume that these variations rely on the diverse surface groups of the different kinds of spider silk which influence the rate of nucleation and that the thickness of the silica coating generally increases with the

hydrophilicity of the template surface. However, the thickness should not exceed a critical value (more than 200 nm). Thicker shells often led to crack formation during calcination, especially for the thicker fibres. Before calcination and up to a certain thickness the shell is still partially gas permeable due to connected nanopores what reduces the pressure during decomposition of the organic template material. Besides, SEM images of the channels revealed that the polystyrene and spider silk threads are really enclosed by the silica shell resulting in a circular channel cross-section (Figs. 6.4a-b and 6.5b-c) whereas the PVA fibres are covered with a "silica blanket" and no silica nucleated at their bottom side what results in a more elliptical channel cross-section (Fig. 6.3b). We assume that this rely on the stronger adhesion of the PVA fibre to the substrate. To investigate whether this shape is caused by swelling of PVA during the coating reaction we sputtered a 120 nm thick layer of indium tin oxide (ITO) onto a PVA fibre-covered substrate. A SEM image of the calcinated sample also
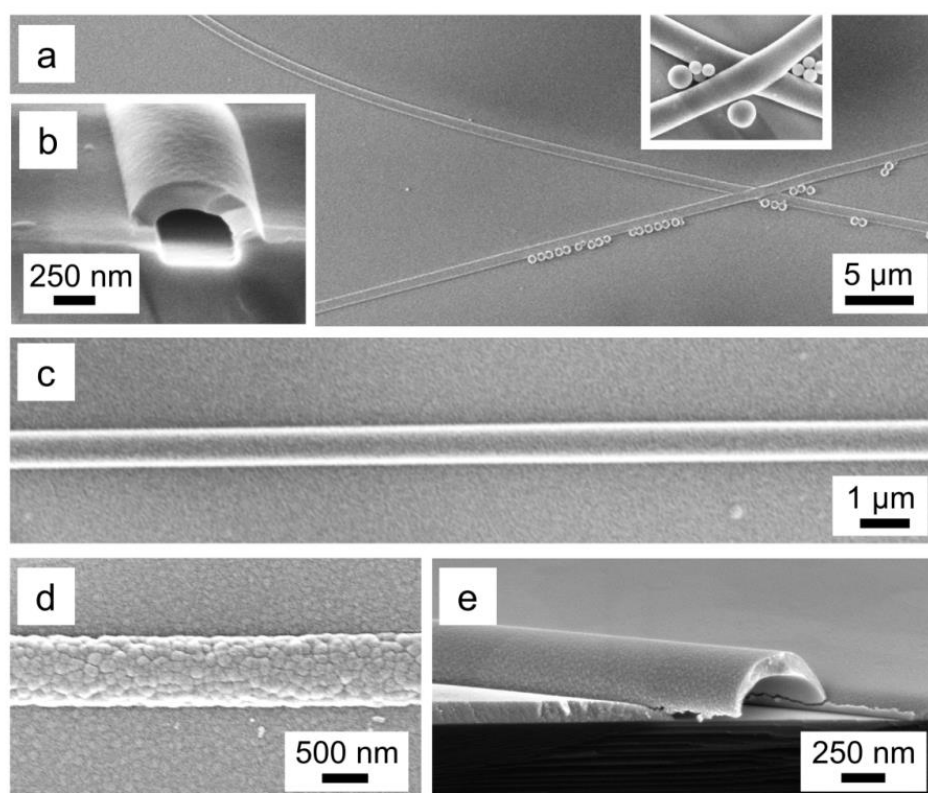
Figure 6.3: Silica nanochannels prepared by coating and subsequent calcination of PVA nanofibres that (a - c) were treated with an oxygen plasma before and (d) silica nanochannels with a nanoporous and rough silica shell without previous oxygen plasma treatment of the fibre surface. e) Indium tin oxide (ITO) nanochannel prepared by sputtering a layer of ITO onto a PVA template fibre and subsequent calcination. Coating of crossed fibres resulted in connected and tight channel junctions (a, inset).
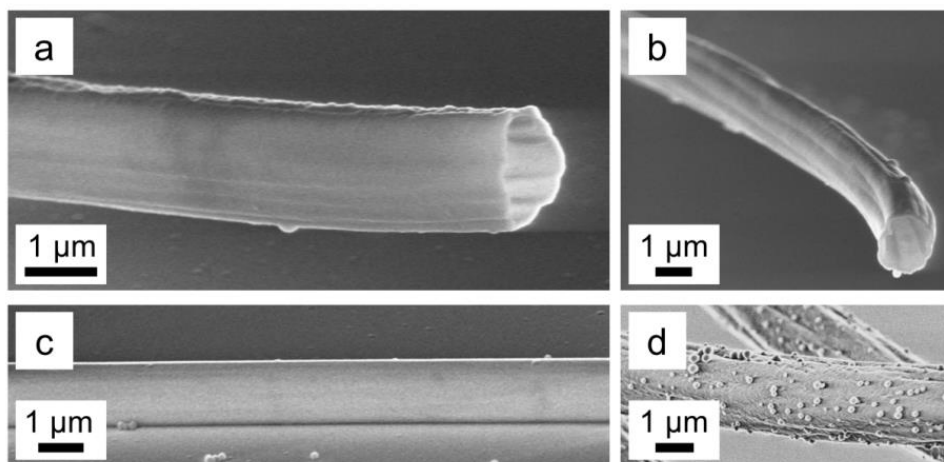
Figure 6.4: a) - c) Silica microchannels that were synthesized by templating against PS microfibres followed by calcination. The PS fibre surface was treated with an oxygen plasma before coating. d) Without surface modification only poor silica nucleation was observed.

showed an elliptical cross-section (Fig. 6.3e). This indicates that the elliptical shape is caused by a deformation of the fibre due to the strong adhesion of the hydrophilic PVA fibre to the hydrophilic substrate. By coating two fibers crossing each other we obtained channel junctions (Fig. 6.3a).

To gain information on the surface morphology the inner and outer wall of a broken piece of a spider silk-templated channel was imaged with a scanning force microscope (SFM). Whereas the outer channel wall had a root mean square (RMS) roughness of 2.2 nm over an area of 275×275 nm^2 (Fig. 6.5e) the RMS roughness of the inner wall was only 1.6 nm (Fig. 6.5f). The roughness at the outside arises from heterogeneous nucleation of silica that formed small islands which gradually grew with the reaction time.
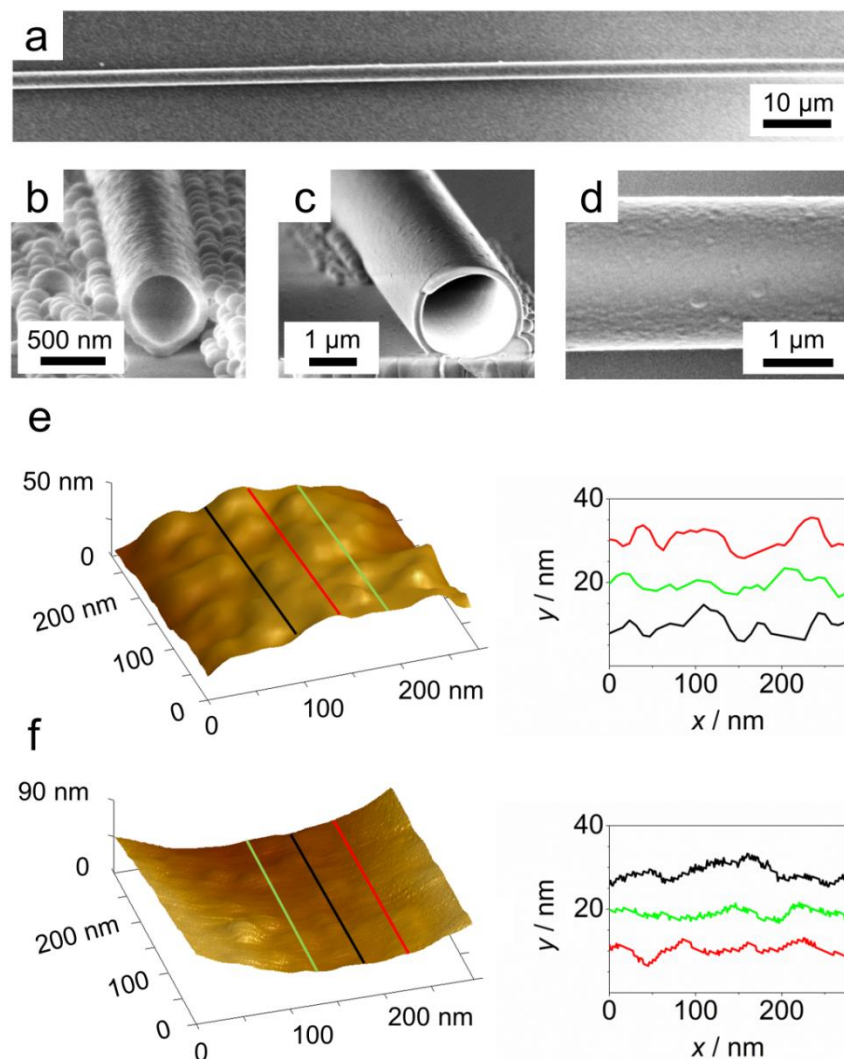
Figure 6.5: SEM images of spider silk-templated silica (b) nano- and (a, c, d) microchannels showing their (a) highly uniform diameter, (b, c) circular cross-section and (d) surface topography. e), f) SFM images of the (e) outer and (f) inner silica channel wall. The coloured lines illustrate the positions of the plotted profiles.

To prove that the channels are solvent-tight we embedded a closed loop in a drop of dyed glycerine/water 80 % (Fig. 6.6). Since silica is hydrophilic, the outer surface of the channels became fully wetted. In reflection mode the contour of the channel was identified as a bright line (Fig. 6.6a). It results from light that is reflected at the inner wall of the channel due to refractive index mismatch, proving that the channels were filled with air. The refractive indices of glycerine/water 80 % (1.45) and glass or silica ($\sim$ 1.52) are too similar. Therefore reflections from wetted parts of the substrate and the channel can not be resolved. Simultanelously, we recorded the fluorescence of the solution (Fig. 6.6b). Again, the channel remained clearly visible as
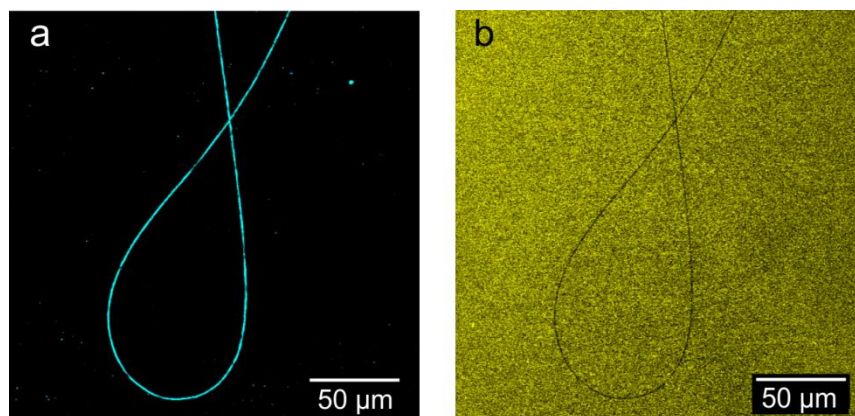
Figure 6.6: Confocal images of a microchannel embedded in dyed glycerine/water 80 %. a) Reflection of light at the silica-air interface depicts the contour of the channel. b) Fluorescence image of the same channel. The channel remained free of dye.

a dark loop in a bright background caused by the fluorescence of the wetted substrate (yellow). A crack would allow the solution to wet parts of the channels, causing disapperance of the reflection and appearance of fluorescence, making the channel indistinguishable from the background. However, no penetration of solvent into the channel was observed until the end of the measurement, which took more than one hour.

The channels are not only solvent-tight but also airtight. To prove their airtightness and to demonstrate that the channels are connected at a junction point, we monitored the filling of a channel junction with a closed loop (Fig. 6.7). The imbibition of fluorescently labelled castor oil was monitored by confocal microscopy. To suppress wetting outside the channel, the substrate and outer channel surface were hydrophobized with (1H,1H,2H,2H)-perfluorooctyltrichlorosilane. The shape of the channel is shown in transmission mode (Fig. 6.7a). The dark spots result from silica spheres that formed during the Stöber reaction and adhered to the glass surface. A drop of castor oil was carefully deposited to the left of the channel opening. Since castor oil wets silica (contact angle nearly zero), capillary forces drew the oil into the channel (Fig. 6.7b, green line). When the liquid meniscus reached the junction, it was drawn into both entrances of the loop and into the continuing channel (Fig. 6.7c-f). The continuing channel was filled rapidly. Filling of the closed loop slowed down (Fig. 6.7g) until it stopped (Fig. 6.7h), when the compression of the air counterbalanced the capillary force. The presence of trapped air is proven by the part of the channel that remains black. The trapped air was not leaking out, even though the capillary pressure reached $P = 2\gamma/r = 3.2$ bar, where $\gamma = 34.7$ mN/m (22°C) is the surface tension of the liquid and $r = 220$ nm the inner radius of the capillary. This verifies

that the channels are airtight and robust, even at parts with high curvature like in a loop, and that they are connected at the junction points.
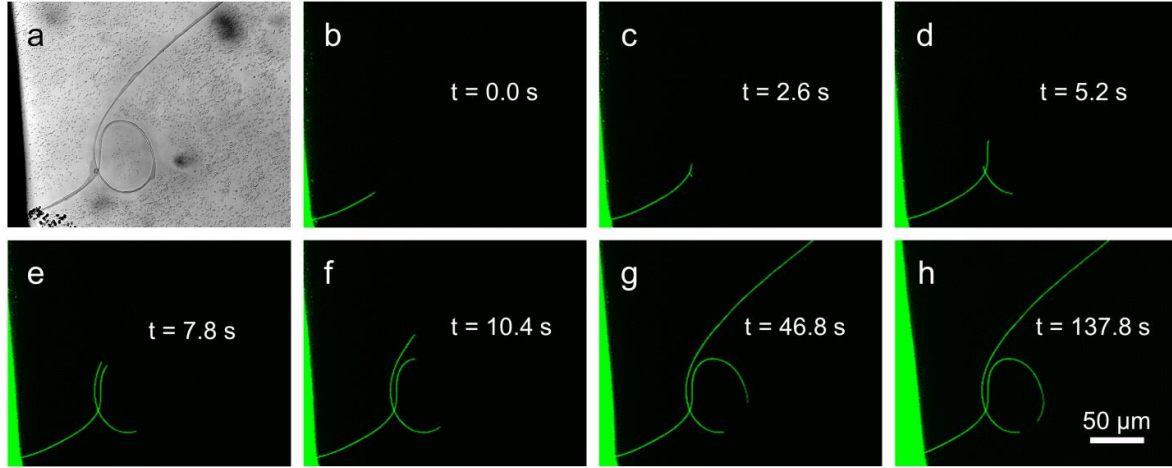
Figure 6.7: Confocal microscope images of the capillary filling of fluorescently labelled castor oil into a silica channel with a closed loop. a) Transmission image of the channel. b) - h) Fluorescence images tracking the filling of the channel. The channel was fabricated from a PVA nanofibre as template (average channel diameter: 440 nm, average wall thickness: 100 nm). The image resolution was about 0.35 μm. Images were recorded every 2.6 s. The contact line of the drop seen in the bottom left (reservoir, light green) moved slowly with a velocity of 0.14 μm/s.

Liquid flow in thin capillaries is usually dominated by capillary pressure rather than external hydrostatic pressure. The distance x a liquid penetrates into a horizontal cylindrical channel due to capillary action is according to Lucas and Washburn proportional to the square root of time:[65],[66]

$$x = c \sqrt{t}, \quad c = \sqrt{\frac{r \, \gamma \cos \theta}{2 \, \eta}} \tag{6.1}$$

Here, η is the dynamic viscosity, θ the advancing contact angle of the liquid, and c is the Lucas-Washburn coefficient. Even though capillary filling in microchannels obeys the power-law for long times, deviations of the Lucas-Washburn coefficient were observed for the early stage of capillary filling.[216],[228],[229] Spider silk-templated silica channels with their uniform diameter, transparency and circular cross-section in combination with the high viscosity (880 mPa s, 23 °C), low surface tension, and zero contact angle of castor oil are ideally suited for detailed measurements of the filling kinetics. The channels were cut open with a diamond tip. A liquid drop (reservoir)

was deposited close to the opening. The meniscus moved according to the Lucas-Washburn equation for different channel diameters, proving that the channels are defect-free with homogeneous thickness and wetting properties (Fig. 6.8a). To exclude an effect of the dye a measurement without dye was performed. In this case the liquid meniscus was detected from the transmitted light. The filling velocity was identical.

The Lucas-Washburn law was also tested using liquids of higher surface tension and nonzero contact angle on silica. For aqueous glycerol solutions (80 v% and 90 v%) with dynamic viscosities of 70 mPa s and 230 mPa s (23 °C), respectively, the $t^{1/2}$ power law of the Lucas-Washburn equation was obeyed (Fig. 6.8b). Since r, γ and η are known, the Lucas-Washburn law allows to measure θ in capillaries. For 90 v% glycerol an advancing contact angle of $\theta = 70°$ was obtained (dotted line, Fig. 6.8b). To demonstrate the absence of defects of the channels we measured the filling velocities of glycerol over a distance of several millimetres (Fig. 6.8c, Fig. 6.9c). Indeed, the measured values were consistent with the $t^{1/2}$ power law of the Lucas-Washburn equation even after 100 s. We also measured deliberately channels with defects. In those cases steps in the time dependence of the distance were observed, or even air bubbles sucked into the channels through larger defects (Fig. S6.1).
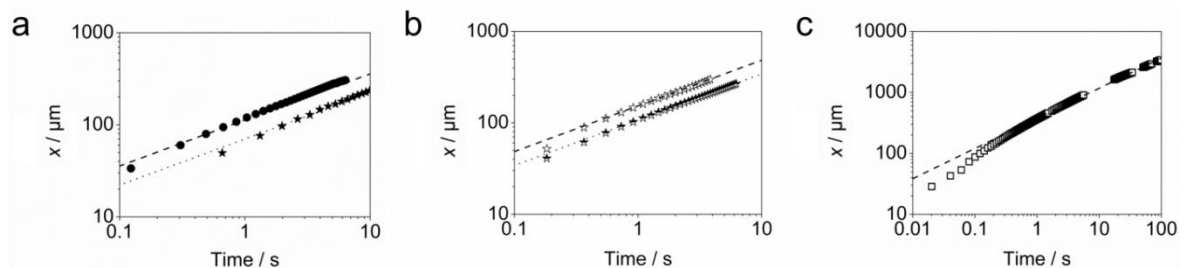
Figure 6.8: a) Filling distance of castor oil in a spider silk-templated channel (radius, $r = 650 \pm 50$ nm, circles) and in a PVA-templated channel ($r = 250 \pm 50$ nm, stars). The lines show the corresponding theoretical values according to Lucas and Washburn for an advancing contact angle of zero. b) Filling distance of 80 v% (empty stars) and 90 v% (half-filled stars) glycerol-water solutions in a PVA-templated channel with $r = 250$ nm. The lines correspond to an advancing contact angle of $\theta = 70°$ and viscosity $\eta = 118$ mPa s (dashed line: 80 v% glycerol) or 233 mPa s (dotted line: 90 v% glycerol). The viscosity of 80 v% glycerol was slightly above its nominal value, likely since water close to the liquid/air interface of the reservoir evaporated. c) Long distance capillary filling of glycerol (80 v%) into a spider silk-templated channel with $r = 1.0 \pm 0.1$ μm. The dashed line illustrates the $t^{1/2}$ power law for $t > 0.2$ s.

At short filling times (t < 0.2 s) we always observed a deviation to slower velocities from the theoretically predicted power law (Fig. 6.9a). The length of the channel filled with solvent increases nearly proportional to t. This also holds for water; for water, however, the high filling velocity hindered imaging longer distances. The water meniscus in a silica channel with a radius of 1 μm already reached a distance of almost 800 μm after 83 ms (Fig. 6.9a-b). Deviations from the Lucas-Washburn law at low filling velocities have been observed in the past. Possible explanations for the deviation of the filling velocity from the Lucas-Washburn law are: an increased contact angle at high advancing speed,[216] inertia,[219]   evaporation induced prewetting of the capillary,[219],[220] nonlinear energy dissipation, and flow pattern effects[221] at the channel opening; edges at the entrance may generate vortices which reduce the initial filling rate.[219] The highest Reynolds number of all measurements is the one for water in the channel with r = 1.0 μm: $Re = \rho\, v\, r/\eta = 10^{-2}$, where $v = 10$ mm s^{-1}. This low value minimizes the likeliness of vortex formation, although recirculating zones can occur in viscous fluids even if the Reynolds number is vanishingly small.[230] Flow in the reservoir or vortex formation has a minimal effect, since deviations are also observed when the liquid meniscus is at distances orders of magnitude larger than the channel diameter. To investigate whether the deviations of the flow velocity are due to evaporation induced prewetting of the capillary, we studied volatile as well as non-volatile liquids. All investigated liquids showed pronounced deviations of the filling kinetics at short times, excluding evaporation induced prewetting as the main reason. Even though inertia can be important in macroscopic channels, in thin capillaries the liquid should be accelerated almost instantaneously. To estimate the acceleration we neglected viscous forces and assume that the capillary force puts a length of liquid, e.g. L = 50 μm, in motion. The acceleration is $a = 2\,\gamma\,cos\theta/\rho\, r\, L$. With r = 1.0 μm, γ = 72 mN/m, θ = 0° and ρ = 10^3 kg m^{-3} one gets $a \approx 3{\times}10^6$ m s^{-2}. This large value suggests that inertia should be negligible at times longer than a few μs. Inertial effects were investigated by Quéré.[219] He found that for $t < \tau^* = \rho\, r^2/4\,\eta$ the meniscus moves with a constant velocity $v = \sqrt{2\,\gamma/\rho\, r}$. For water the respective values are τ^* = 0.25 μs and c = 12 m s^{-1}, i.e. the inertia dominated regime breaks down 6 orders of magnitude before the filling velocity follows the Lucas-Washburn law (Figs. 6.8-9). For more viscous liquids τ^* is even shorter, showing that inertial effects cannot explain the deviations observed in capillaries with a thickness of a few μm or less.
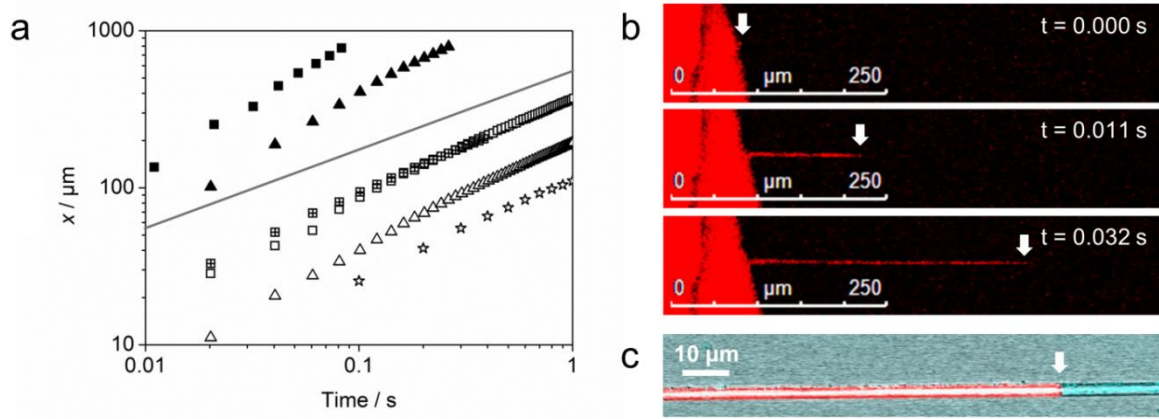
Figure 6.9: (a) Initial deviations from the $t^{1/2}$ power law (grey line) of water (filled symbols) and 80 v% glycerol (empty and structured symbols) penetrating into silica capillaries with $r = 1.0 \pm 0.1$ μm (squares), 0.4 ± 0.1 μm (triangles) and 0.25 ± 0.05 μm (stars), respectively. Apart from the channels with $r = 0.25$ μm (stars, PVA-templated) all other channels originated from spider silk fibres. Confocal microscope snap-shots showing the capillary filling of dyed (b) water and (c) glycerol into a silica channel, $r = 1.0 \pm 0.1$ μm. The white arrows mark the position of the liquid menisci.

Fitting the curve of capillary filling with the Lucas-Washburn equation yields an advancing contact angle of $\theta = 70°$ for glycerol (Fig. 6.8b-c) which is much larger than the static contact angle of glycerol on silica $\theta = 10°$. To check to what extent dynamic wetting may affect the contact angle we estimated θ for every point of the curve in Figure 6.8c by balancing the capillary and viscous forces:

$$8\pi\eta x \frac{dx}{dt} = 2\pi\gamma r \cos\theta \implies \cos\theta = \frac{2\eta}{\gamma r}\frac{dx^2}{dt} \qquad (6.2)$$

The extracted values (Fig. 6.10a) show that the contact angle indeed varied during capillary filling. At short times it reached nearly 90° and then droped to a constant value of about 60°. This is why the fit of the filling length with Equation 6.1 fails at short times. To demonstrate the failure of the Lukas-Washburn law in the early stage caused by a dynamic contact angle, we measured the time dependence of the contact angle in much larger PMMA capillaries, with an inner radius of 0.25 mm. We compared castor oil (Fig. 6.10b) and isopropanol ($\gamma = 23$ mN/m, $\eta = 2.1$ mPa s at 25°C) (Fig. 6.10c). Both liquids have static contact angles of about 30° on flat PMMA. For both liquids strong deviations from this value are observed, especially at short times. The contact angle continues to decrease even after 1000 s (Fig. 6.10b). For comparison, we calculated the contact angle of castor oil in silica channels according to Equation 6.2. We obtained $\cos\theta = 1.0$ in agreement with the value assumed in

Figure 6.8a. Thus, due to dynamic wetting the actual contact angle in a channel may differ significantly from the static one and strongly depends on velocity, supporting that the deviations of the filling velocity at short times are due to a velocity dependent contact angle.
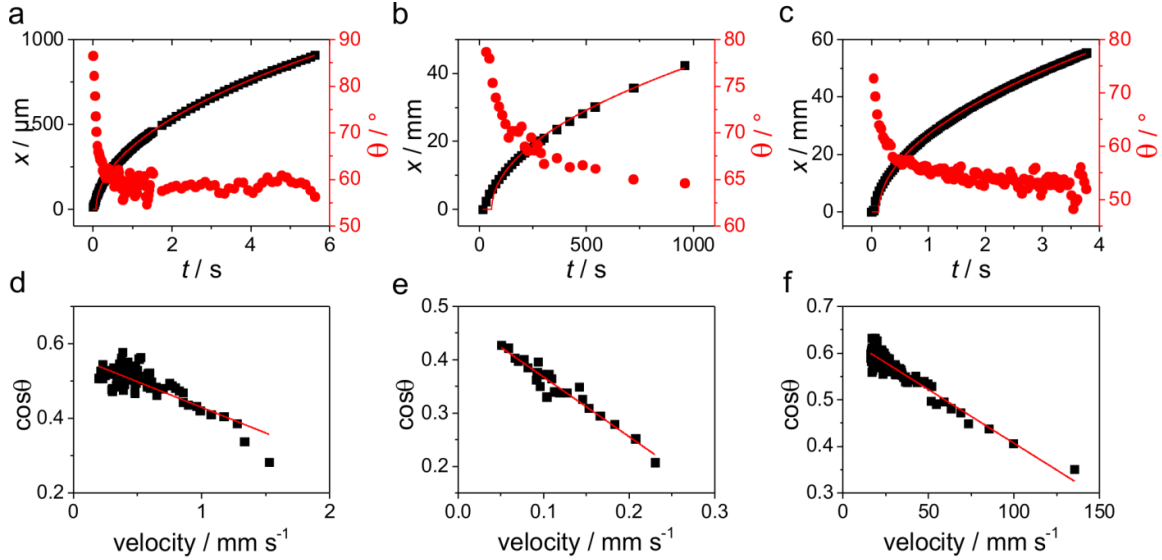
Figure 6.10: a) Capillary filling of glycerol (80 v%) into a microchannel ($r = 1.0 \pm 0.1$ µm). b), c) Filling of a PMMA tube ($r = 0.25$ mm) by (b) castor oil and (c) isopropanol. The red points correspond to the contact angles for every measured filling distance. d) to f) show the dependence of the advancing contact angle on the velocity and the red lines the fit of the data according to the molecular-kinetic theory using the values listed in Table 6.1.

The description of the velocity dependence of the advancing contact angle has received a lot of attention in modelling wetting dynamics. The two most intensively studied approaches are the molecular-kinetic theory (MKT) and the hydrodynamic theory.[67] MKT assumes that the motion of the molecules in the liquid-air-substrate contact zone can be described by a composition and substrate dependent jump frequency of the molecules, where the average displacement relates to the distance between neighbouring adsorption sites. For small displacements the velocity dependence of the contact angle is given by:[67]

$$v = \zeta^{-1} \gamma (\cos \theta_0 - \cos \theta) \tag{6.3}$$

where the wetting-line friction ζ depends on the frequency and distance of displacements, θ_0 is the microscopic and θ the advancing contact angle. Thus, $cos\theta = cos\theta_0 - v \zeta \gamma^{-1}$ depends linearly on velocity, where the wetting-line friction

is proportional to the slope of $\cos\theta$ (v). The microscopic advancing contact angle is given by $v \to 0$. The velocities were derived from the derivative of the time dependent filling distance (Fig. 6.10e-f). The molecular-kinetic theory represents the data quite well (red lines in Fig. 6.10e-f) and the values for ζ are in the same order of magnitude than observed for other systems (Table 6.1).[67] The data for $\cos\theta$ (v) can be equally well fitted with the hydrodynamic theory: $\theta^3 - \theta_0{}^3 = 9\,Ca\,ln(r/L_\mathrm{m})$, with $Ca \equiv v\eta/\gamma$ the capillary number and L_m the cut-off length.[231],[232] The microscopic contact angle agreed within 5 % (Table 6.1). However, the values for the cut-off length varied by several orders of magnitude and were well below molecular dimensions for 80 v% glycerine (1×10^{-11} nm) and castor oil (1.1×10^{-5} nm). The good description of the velocity dependent contact angle by the molecular-kinetic and hydrodynamic theory supports that the deviations of Lukas-Washburn for short times are dominated by the velocity dependent contact angle.

Table 6.1: Fitted values for the advancing microscopic contact angle θ_0 according to molecular-kinetic and hydrodynamic theory, the wetting-line friction ζ and the cut-off length L_m. The values for the interfacial tension γ and viscosity η were taken from literature.

	80 v% glycerol	Castor oil	Isopropanol
MKT: $cos\,\theta_0$	0.57	0.48	0.64
Hydrodynamic theory: $cos\,\theta_0$	0.57	0.49	0.65
ζ / Pa s	8.9	39	0.05
L_m / nm	1×10^{-11}	1.1×10^{-5}	4.2
r / nm	1000	250 000	250 000
γ / mN m^{-1}	65	35	23
η / Pa s	0.118	0.88	0.002

6.4   CONCLUSION

In summary, to fabricate airtight, mechanically stable and chemically inert channels, different fibres were coated with a silica shell using a Stöber synthesis. Transparent silica nano- and microchannels with homogeneous, circular cross-section and high length-to-diameter ratio are obtained after removing the sacrificial fibres by

calcination. The channels are UV stable and do not swell when exposed to organic or inorganic solvents. 100 nm thick silica walls already possess a Young modulus as high as 40 GPa, i.e. close to fused silica.[84] Although chemically inert, a silica surfaces can easily be chemically modified, allowing to selectively tune the hydrophilicity and hydrophobicity of the inner and outer surface of the channels, thereby also tuning the flow behaviour. Coating crossed fibres permitted to achieve connected channel junctions, that remain airtight even when applying a pressure above 3 bar. To the best of our knowledge this is the first study proving that the microchannels are solvent- and airtight. This offers the perspective to fabricate tight nanojunctions in a controlled way. The presented strategy offers a promising alternative to coaxial electrospinning, still keeping the advantageous of electrospinning, such as its high yield, wide range of accessible diameters and options to align the fibres in a predetermined way.

The model character of the channels allowed for a systematic investigation of the origin of the deviations from Lucas-Washburn at short filling times. We ruled out evaporation induced prewetting by investigating volatile and non-volatile liquids. Vortex formation in the reservoir is unlikely to be the origin of the deviations since they are also observed far beyond the channel entrance. Inertial effects can be excluded because the deviations are observed for time scales lasting more than 6 orders of magnitude after the inertia dominated regime. Our data support that the initial deviations are dominated by a velocity dependent contact angle. Indeed, the velocity dependent contact angle can be well described by the molecular-kinetic theory with the coefficient of wetting line-friction as only free parameter.

6.5   ACKNOWLEDGEMENTS

6.6   SUPPLEMENTARY INFORMATION

Deviations with defects:
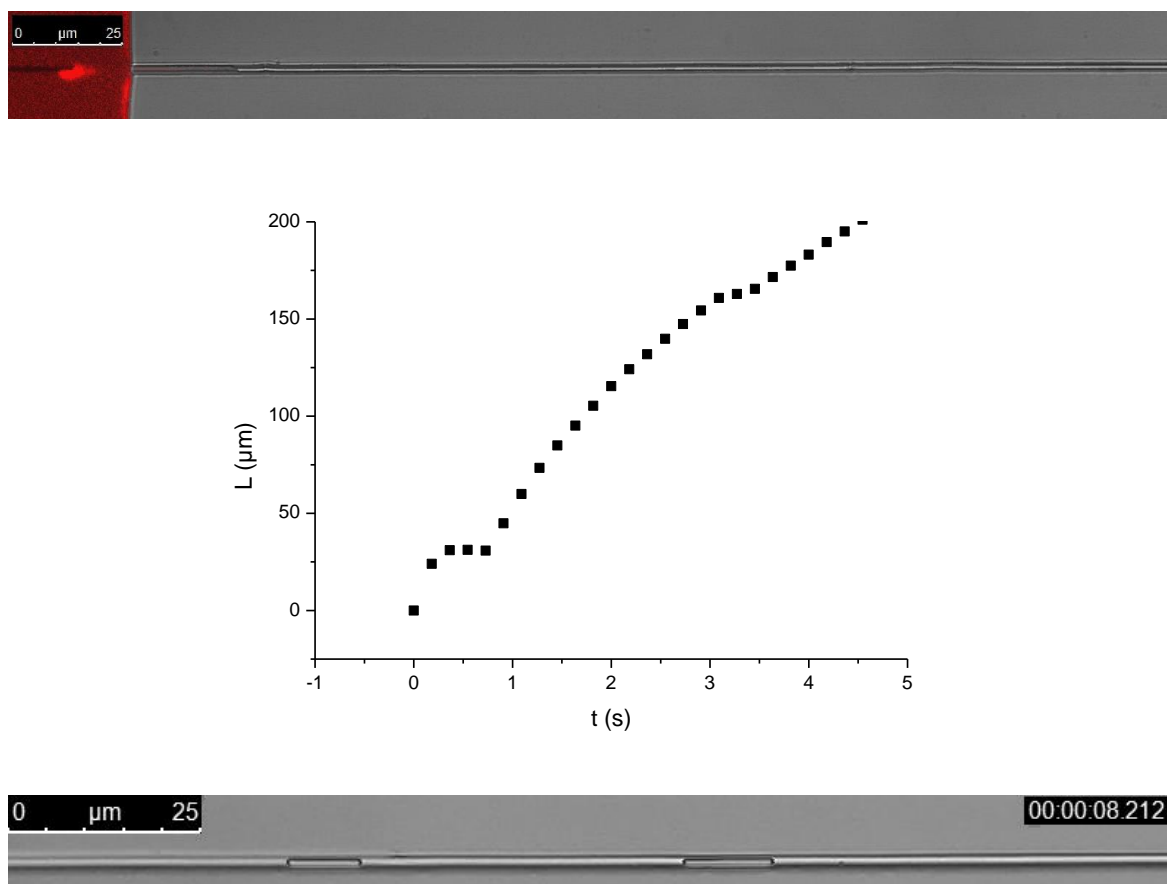
Figure S6.1: Top: A chanel with two defects. The defects are marked by the white arrows. Middle: If the solvents hits a defect the filling velocitiy is delayed, reflected in a step in the time dependent position of the meniscus (L). Bottom: After the solvent passed the defect air is sucked into the channel.

MOVIE S.6.1: Capillary filling of fluorescently labelled glycerol (80 v%) into a spider silk-templated silica channel (radius: 1 µm). The movie shows the first 1.3 s of filling.

REFERENCES

[1]   T. Young, *An Essay on the Cohesion of Fluids, Phil. Trans. R. Soc. Lond.* **1805**, *95*, 65-87.

[2]   C. W. Extrand, *Designing for optimum liquid repellency, Langmuir* **2006**, *22*, 1711-1714.

[3]   T. Nishino, M. Meguro, K. Nakamae, M. Matsushita, Y. Ueda, *The lowest surface free energy based on -CF3 alignment, Langmuir* **1999**, *15*, 4321-4323.

[4]   H. J. Butt, K. Graf, M. Kappl, *Physics and Chemistry of Interfaces*, WILEY-VCH Verlag GmbH & Co. KGaA, Weinheim, **2006**.

[5]   R. N. Wenzel, *Resistance of solid surfaces to wetting by water, Ind Eng Chem* **1936**, *28*, 988-994.

[6]   M. Callies, D. Quere, *On water repellency, Soft Matter* **2005**, *1*, 55-61.

[7]   A. Lafuma, D. Quere, *Superhydrophobic states, Nat Mater* **2003**, *2*, 457-460.

[8]   A. B. D. Cassie, S. Baxter, *Wettability of porous surfaces., T Faraday Soc* **1944**, *40*, 0546-0550.

[9]   E. L. Decker, S. Garoff, *Contact line structure and dynamics on surfaces with contact angle hysteresis, Langmuir* **1997**, *13*, 6321-6332.

[10]   F. E. Bartell, J. W. Shepard, *Surface Roughness as Related to Hysteresis of Contact Angles .2. The Systems Paraffin-3 Molar Calcium Chloride Solution-Air and Paraffin-Glycerol-Air, J Phys Chem-Us* **1953**, *57*, 455-458.

[11]   C. W. Extrand, *Contact angles and hysteresis on surfaces with chemically heterogeneous islands, Langmuir* **2003**, *19*, 3793-3796.

[12]   L. C. Gao, T. J. McCarthy, *How Wenzel and Cassie were wrong, Langmuir* **2007**, *23*, 3762-3765.

[13]   L. C. Gao, T. J. McCarthy, *Wetting 101 degrees, Langmuir* **2009**, *25*, 14105-14115.

[14]   J. W. Krumpfer, P. Bian, P. W. Zheng, L. C. Gao, T. J. McCarthy, *Contact Angle Hysteresis on Superhydrophobic Surfaces: An Ionic Liquid Probe Fluid Offers Mechanistic Insight, Langmuir* **2011**, *27*, 2166-2169.

[15]   L. C. Gao, T. J. McCarthy, *The "lotus effect" explained: Two reasons why two length scales of topography are important, Langmuir* **2006**, *22*, 2966-2967.

[16]   C. V. Boys, *Soap-bubbles and the forces which mould them.*, Society for Promoting Christian Knowledge, London, **1896**.

[17]   C. Neinhuis, W. Barthlott, *Characterization and distribution of water-repellent, self-cleaning plant surfaces, Ann Bot-London* **1997**, *79*, 667-677.

[18]   W. Barthlott, C. Neinhuis, *Purity of the sacred lotus, or escape from contamination in biological surfaces, Planta* **1997**, *202*, 1-8.

[19]   T. L. Sun, L. Feng, X. F. Gao, L. Jiang, *Bioinspired surfaces with special wettability, Accounts Chem Res* **2005**, *38*, 644-652.

[20]   X. F. Gao, L. Jiang, *Water-repellent legs of water striders, Nature* **2004**, *432*, 36-36.

[21]   Y. W. Su, B. H. Ji, Y. Huang, K. C. Hwang, *Nature's Design of Hierarchical Superhydrophobic Surfaces of a Water Strider for Low Adhesion and Low-Energy Dissipation, Langmuir* **2010**, *26*, 18926-18937.

[22]   L. Zhang, Z. Zhou, B. Cheng, J. M. DeSimone, E. T. Samulski, *Superhydrophobic Behavior of a Perfluoropolyether Lotus-Leaf-like Topography, Langmuir* **2006**, *22*, 8576-8580.

[23]   D. K. Owens, R. C. Wendt, *Estimation of Surface Free Energy of Polymers, J Appl Polym Sci* **1969**, *13*, 1741-1747.

[24]   A. M. Cao, L. L. Cao, D. Gao, *Fabrication of nonaging superhydrophobic surfaces by packing flowerlike hematite particles, Appl Phys Lett* **2007**, *91*, 034102.

[25]   L. L. Cao, H. H. Hu, D. Gao, *Design and fabrication of micro-textures for inducing a superhydrophobic behavior on hydrophilic materials, Langmuir* **2007**, *23*, 4310-4314.

[26]   S. Herminghaus, *Roughness-induced non-wetting*, *Europhys Lett* **2000**, *52*, 165-170.

[27]   Y. T. Cheng, D. E. Rodak, *Is the lotus leaf superhydrophobic?*, *Appl Phys Lett* **2005**, *86*, 144101.

[28]   B. He, N. A. Patankar, J. Lee, *Multiple equilibrium droplet shapes and design criterion for rough hydrophobic surfaces*, *Langmuir* **2003**, *19*, 4999-5003.

[29]   T. N. Krupenkin, J. A. Taylor, E. N. Wang, P. Kolodner, M. Hodes, T. R. Salamon, *Reversible wetting-dewetting transitions on electrically tunable superhydrophobic nanostructured surfaces*, *Langmuir* **2007**, *23*, 9128-9133.

[30]   T. Verho, J. T. Korhonen, L. Sainiemi, V. Jokinen, C. Bower, K. Franze, S. Franssila, P. Andrew, O. Ikkala, R. H. A. Ras, *Reversible switching between superhydrophobic states on a hierarchically structured surface*, *P Natl Acad Sci USA* **2012**, *109*, 10210-10213.

[31]   R. Hensel, R. Helbig, S. Aland, H. G. Braun, A. Voigt, C. Neinhuis, C. Werner, *Wetting Resistance at Its Topographical Limit The Benefit of Mushroom and Serif T Structures*, *Langmuir* **2013**, *29*, 1100-1112.

[32]   W. Chen, A. Y. Fadeev, M. C. Hsieh, D. Oner, J. Youngblood, T. J. McCarthy, *Ultrahydrophobic and ultralyophobic surfaces: Some comments and examples*, *Langmuir* **1999**, *15*, 3395-3399.

[33]   A. Tuteja, W. Choi, M. L. Ma, J. M. Mabry, S. A. Mazzella, G. C. Rutledge, G. H. McKinley, R. E. Cohen, *Designing superoleophobic surfaces*, *Science* **2007**, *318*, 1618-1622.

[34]   L. L. Cao, T. P. Price, M. Weiss, D. Gao, *Super water- and oil-repellent surfaces on intrinsically hydrophilic and oleophilic porous silicon films*, *Langmuir* **2008**, *24*, 1640-1643.

[35]   A. Ahuja, J. A. Taylor, V. Lifton, A. A. Sidorenko, T. R. Salamon, E. J. Lobaton, P. Kolodner, T. N. Krupenkin, *Nanonails: A simple geometrical approach to electrically tunable superlyophobic surfaces*, *Langmuir* **2008**, *24*, 9-14.

[36]   X. Deng, L. Mammen, H. J. Butt, D. Vollmer, *Candle Soot as a Template for a Transparent Robust Superamphiphobic Coating*, *Science* **2012**, *335*, 67-70.

[37]   A. Tuteja, W. J. Choi, G. H. McKinley, R. E. Cohen, M. F. Rubner, *Design parameters for superhydrophobicity and superoleophobicity*, *Mrs Bull* **2008**, *33*, 752-758.

[38]   M. Nosonovsky, *Multiscale roughness and stability of superhydrophobic biomimetic interfaces*, *Langmuir* **2007**, *23*, 3157-3161.

[39]   A. Tuteja, W. Choi, J. M. Mabry, G. H. McKinley, R. E. Cohen, *Robust omniphobic surfaces*, *P Natl Acad Sci USA* **2008**, *105*, 18200-18205.

[40]   K. Tsujii, T. Yamamoto, T. Onda, S. Shibuichi, *Super oil-repellent surfaces*, *Angewandte Chemie-International Edition in English* **1997**, *36*, 1011-1012.

[41]   N. A. Patankar, *On the modeling of hydrophobic contact angles on rough surfaces*, *Langmuir* **2003**, *19*, 1249-1253.

[42]   H. J. Butt, C. Semprebon, P. Papadopoulos, D. Vollmer, M. Brinkmann, M. Ciccotti, *Design principles for superamphiphobic surfaces*, *Soft Matter* **2013**, *9*, 418-428.

[43]   Z. G. Guo, W. M. Liu, B. L. Su, *Superhydrophobic surfaces: From natural to biomimetic to functional*, *Journal of Colloid and Interface Science* **2011**, *353*, 335-355.

[44]   Q. M. Pan, H. Z. Jin, H. Wang, *Fabrication of superhydrophobic surfaces on interconnected Cu(OH)(2) nanowires via solution-immersion*, *Nanotechnology* **2007**, *18*, 355605(4pp).

[45]   M. N. Qu, B. W. Zhang, S. Y. Song, L. Chen, J. Y. Zhang, X. P. Cao, *Fabrication of superbydrophobic surfaces on engineering materials by a solution-immersion process*, *Adv Funct Mater* **2007**, *17*, 593-596.

[46]   Z. G. Guo, W. M. Liu, *Superhydrophobic spiral Co3O4 nanorod arrays*, *Appl Phys Lett* **2007**, *90*, 193108.

[47]   Y. Li, W. Z. Jia, Y. Y. Song, X. H. Xia, *Superhydrophobicity of 3D porous copper films prepared using the hydrogen bubble dynamic template*, *Chem Mater* **2007**, *19*, 5758-5764.

[48] S. T. Wang, Y. L. Song, L. Jiang, *Microscale and nanoscale hierarchical structured mesh films with superhydrophobic and superoleophilic properties induced by long-chain fatty acids*, Nanotechnology **2007**, *18*, 015103(5pp).

[49] A. Ruiz, A. Valsesia, G. Ceccone, D. Gilliland, P. Colpo, F. Rossi, *Fabrication and characterization of plasma-processed surfaces with tuned wettability*, Langmuir **2007**, *23*, 12984-12989.

[50] N. Vourdas, A. Tserepi, E. Gogolides, *Nanotextured super-hydrophobic transparent poly(methyl methacrylate) surfaces using high-density plasma processing*, Nanotechnology **2007**, *18*, 125304(7pp).

[51] K. K. S. Lau, J. Bico, K. B. K. Teo, M. Chhowalla, G. A. J. Amaratunga, W. I. Milne, G. H. McKinley, K. K. Gleason, *Superhydrophobic carbon nanotube forests*, Nano Lett **2003**, *3*, 1701-1705.

[52] S. H. Li, H. B. Xie, S. B. Zhang, X. H. Wang, *Facile transformation of hydrophilic cellulose into superhydrophobic cellulose*, Chem Commun **2007**, 4857-4859.

[53] H. F. Hoefnagels, D. Wu, G. de With, W. Ming, *Biomimetic superhydrophobic and highly oleophobic cotton textiles*, Langmuir **2007**, *23*, 13158-13163.

[54] Y. Li, G. T. Duan, W. P. Cai, *Controllable superhydrophobic and lipophobic properties of ordered pore indium oxide array films*, Journal of Colloid and Interface Science **2007**, *314*, 615-620.

[55] J. Bravo, L. Zhai, Z. Z. Wu, R. E. Cohen, M. F. Rubner, *Transparent superhydrophobic films based on silica nanoparticles*, Langmuir **2007**, *23*, 7293-7298.

[56] L. L. Cao, D. Gao, *Transparent superhydrophobic and highly oleophobic coatings*, Faraday Discuss **2010**, *146*, 57-65.

[57] N. Nuraje, W. S. Khan, Y. Lei, M. Ceylan, R. Asmatulu, *Superhydrophobic electrospun nanofibers*, J Mater Chem A **2013**, *1*, 1929-1946.

[58] M. D'Acunzi, L. Mammen, M. Singh, X. Deng, M. Roth, G. K. Auernhammer, H. J. Butt, D. Vollmer, *Superhydrophobic surfaces by hybrid raspberry-like particles*, Faraday Discuss **2010**, *146*, 35-48.

[59] L. Mammen, X. Deng, M. Untch, D. Vijayshankar, P. Papadopoulos, R. Berger, E. Riccardi, F. Leroy, D. Vollmer, *Effect of Nanoroughness on Highly Hydrophobic and Superhydrophobic Coatings*, Langmuir **2012**, *28*, 15005-15014.

[60] X. Deng, L. Mammen, Y. F. Zhao, P. Lellig, K. Mullen, C. Li, H. J. Butt, D. Vollmer, *Transparent, Thermally Stable and Mechanically Robust Superhydrophobic Surfaces Made from Porous Silica Capsules*, Adv Mater **2011**, *23*, 2962-2965.

[61] D. Xiong, G. J. Liu, L. Z. Hong, E. J. S. Duncan, *Superamphiphobic Diblock Copolymer Coatings*, Chem Mater **2011**, *23*, 4357-4366.

[62] A. Steele, I. Bayer, E. Loth, *Inherently Superoleophobic Nanocomposite Coatings by Spray Atomization*, Nano Lett **2009**, *9*, 501-505.

[63] R. Dufour, M. Harnois, V. Thomy, R. Boukherroub, V. Senez, *Contact angle hysteresis origins: Investigation on super-omniphobic surfaces*, Soft Matter **2011**, *7*, 9380-9387.

[64] T. Darmanin, F. Guittard, S. Amigoni, E. T. de Givenchy, X. Noblin, R. Kofman, F. Celestini, *Superoleophobic behavior of fluorinated conductive polymer films combining electropolymerization and lithography*, Soft Matter **2011**, *7*, 1053-1057.

[65] R. Lucas, *The time law of the capillary rise of liquids.*, Kolloid Z **1918**, *23*, 15-22.

[66] E. W. Washburn, *The dynamics of capillary flow.*, Phys Rev **1921**, *17*, 273-283.

[67] T. D. Blake, *The physics of moving wetting lines*, J Colloid Interf Sci **2006**, *299*, 1-13.

[68] M. Gotzinger, W. Peukert, *Particle adhesion force distributions on rough surfaces*, Langmuir **2004**, *20*, 5298-5303.

[69] K. Zhao, T. G. Mason, *Directing colloidal self-assembly through roughness-controlled depletion attractions*, Phys Rev Lett **2007**, *99*, 268301.

[70] K. Zhao, T. G. Mason, *Suppressing and enhancing depletion attractions between surfaces roughened by asperities*, Phys Rev Lett **2008**, *101*, 148301.

[71] M. Jin, X. Feng, L. Feng, T. Sun, J. Zhai, T. Li, L. Jiang, *Superhydrophobic Aligned Polystyrene Nanotube Films with High Adhesive Force*, Adv Mater **2005**, *17*, 1977-1981.

[72] D. Quere, *Wetting and roughness*, *Annu Rev Mater Res* **2008**, *38*, 71-99.

[73] X. J. Feng, L. Jiang, *Design and creation of superwetting/antiwetting surfaces*, *Adv Mater* **2006**, *18*, 3063-3078.

[74] X. Gao, X. Yan, X. Yao, L. Xu, K. Zhang, J. Zhang, B. Yang, L. Jiang, *The Dry-Style Antifogging Properties of Mosquito Compound Eyes and Artificial Analogues Prepared by Soft Lithography*, *Adv Mater* **2007**, *19*, 2213-2217.

[75] D. Quere, *Non-sticking drops*, *Rep Prog Phys* **2005**, *68*, 2495-2532.

[76] W. Ming, D. Wu, R. van Benthem, G. de With, *Superhydrophobic films from raspberry-like particles*, *Nano Lett* **2005**, *5*, 2298-2301.

[77] Z. Qian, Z. C. Zhang, L. Y. Song, H. R. Liu, *A novel approach to raspberry-like particles for superhydrophobic materials*, *J Mater Chem* **2009**, *19*, 1297-1304.

[78] L. C. Gao, T. J. McCarthy, X. Zhang, *Wetting and Superhydrophobicity*, *Langmuir* **2009**, *25*, 14100-14104.

[79] N. A. Patankar, *Hysteresis with Regard to Cassie and Wenzel States on Superhydrophobic Surfaces*, *Langmuir* **2010**, *26*, 7498-7503.

[80] M. Reyssat, D. Richard, C. Clanet, D. Quere, *Dynamical superhydrophobicity*, *Faraday Discuss* **2010**, *146*, 19-33.

[81] Y. Rahmawan, T. I. Kim, S. J. Kim, K. R. Lee, M. W. Moon, K. Y. Suh, *Surface energy tunable nanohairy dry adhesive by broad ion beam irradiation*, *Soft Matter* **2012**, *8*, 1673-1680.

[82] Y. Rahmawan, M. W. Moon, K. S. Kim, K. R. Lee, K. Y. Suh, *Wrinkled, Dual-Scale Structures of Diamond-Like Carbon (DLC) for Superhydrophobicity*, *Langmuir* **2010**, *26*, 484-491.

[83] W. Stöber, A. Fink, E. Bohn, *Controlled growth of monodisperse silica spheres in the micron size range*, *Journal of Colloid and Interface Science* **1968**, *26*, 62-69.

[84] L. J. Zhang, M. D'Acunzi, M. Kappl, A. Imhof, A. van Blaaderen, H. J. Butt, R. Graf, D. Vollmer, *Tuning the mechanical properties of silica microcapsules*, *Phys Chem Chem Phys* **2010**, *12*, 15392-15398.

[85] H. J. C. Berendsen, J. R. Grigera, T. P. Straatsma, *The Missing Term in Effective Pair Potentials*, *J Phys Chem-Us* **1987**, *91*, 6269-6271.

[86] P. E. M. Lopes, V. Murashov, M. Tazi, E. Demchuk, A. D. MacKerell, *Development of an empirical force field for silica. Application to the quartz-water interface*, *J Phys Chem B* **2006**, *110*, 2782-2792.

[87] W. L. Jorgensen, D. S. Maxwell, J. TiradoRives, *Development and testing of the OPLS all-atom force field on conformational energetics and properties of organic liquids*, *J Am Chem Soc* **1996**, *118*, 11225-11236.

[88] E. K. Watkins, W. L. Jorgensen, *Perfluoroalkanes: Conformational analysis and liquid-state properties from ab initio and Monte Carlo calculations*, *J Phys Chem A* **2001**, *105*, 4118-4125.

[89] M. P. Allen, D. J. Tildesley, *Computer simulation of liquids*, Clarendon Press, **1989**.

[90] S. Pal, H. Weiss, H. Keller, F. Muller-Plathe, *The hydrophobicity of nanostructured alkane and perfluoro alkane surfaces: A comparison by molecular dynamics simulation*, *Phys Chem Chem Phys* **2005**, *7*, 3191-3196.

[91] T. V. M. Ndoro, E. Voyiatzis, A. Ghanbari, D. N. Theodorou, M. C. Bohm, F. Muller-Plathe, *Interface of Grafted and Ungrafted Silica Nanoparticles with a Polystyrene Matrix: Atomistic Molecular Dynamics Simulations*, *Macromolecules* **2011**, *44*, 2316-2327.

[92] F. Leroy, D. J. V. A. dos Santos, F. Muller-Plathe, *Interfacial Excess Free Energies of Solid-Liquid Interfaces by Molecular Dynamics Simulation and Thermodynamic Integration*, *Macromol Rapid Comm* **2009**, *30*, 864-870.

[93] F. Leroy, F. Muller-Plathe, *Solid-liquid surface free energy of Lennard-Jones liquid on smooth and rough surfaces computed by molecular dynamics using the phantom-wall method*, *J Chem Phys* **2010**, *133*, 044110.

[94] F. Leroy, F. Muller-Plathe, *Rationalization of the Behavior of Solid-Liquid Surface Free Energy of Water in Cassie and Wenzel Wetting States on Rugged Solid Surfaces at the Nanometer Scale*, *Langmuir* **2011**, *27*, 637-645.

[95] K. Oura, V. G. Lifshits, A. A. Saranin, A. V. Zotov, *Surface Science: An Introduction*, Springer, **2003**.

[96] P. S. H. Forsberg, C. Priest, M. Brinkmann, R. Sedev, J. Ralston, *Contact Line Pinning on Microstructured Surfaces for Liquids in the Wenzel State*, Langmuir **2010**, *26*, 860-865.

[97] F. Schulman, W. A. Zisman, *The Spreading of Liquids on Low-Energy Surfaces .5. Perfluorodecanoic Acid Monolayers*, J Coll Sci Imp U Tok **1952**, *7*, 465-481.

[98] H. Y. Erbil, A. L. Demirel, Y. Avci, O. Mert, *Transformation of a simple plastic into a superhydrophobic surface*, Science **2003**, *299*, 1377-1380.

[99] X. M. Li, D. Reinhoudt, M. Crego-Calama, *What do we need for a superhydrophobic surface? A review on the recent progress in the preparation of superhydrophobic surfaces*, Chem Soc Rev **2007**, *36*, 1350-1368.

[100] R. Blossey, *Self-cleaning surfaces - virtual realities*, Nat Mater **2003**, *2*, 301-306.

[101] J. Genzer, K. Efimenko, *Creating long-lived superhydrophobic polymer surfaces through mechanically assembled monolayers*, Science **2000**, *290*, 2130-2133.

[102] S. H. Kim, S. Y. Lee, S. M. Yang, *Janus Microspheres for a Highly Flexible and Impregnable Water-Repelling Interface*, Angew Chem Int Edit **2010**, *49*, 2535-2538.

[103] Z. Yoshimitsu, A. Nakajima, T. Watanabe, K. Hashimoto, *Effects of surface structure on the hydrophobicity and sliding behavior of water droplets*, Langmuir **2002**, *18*, 5818-5822.

[104] G. McHale, M. I. Newton, N. J. Shirtcliffe, *Immersed superhydrophobic surfaces: Gas exchange, slip and drag reduction properties*, Soft Matter **2010**, *6*, 714-719.

[105] S. Shibuichi, T. Onda, N. Satoh, K. Tsujii, *Super water-repellent surfaces resulting from fractal structure*, J Phys Chem-Us **1996**, *100*, 19512-19517.

[106] S. Singh, J. Houston, F. van Swol, C. J. Brinker, *Superhydrophobicity - Drying transition of confined water*, Nature **2006**, *442*, 526-526.

[107] G. Manukyan, J. M. Oh, D. van den Ende, R. G. H. Lammertink, F. Mugele, *Electrical Switching of Wetting States on Superhydrophobic Surfaces: A Route Towards Reversible Cassie-to-Wenzel Transitions*, Phys Rev Lett **2011**, *106*, 014501.

[108] Q. D. Xie, J. Xu, L. Feng, L. Jiang, W. H. Tang, X. D. Luo, C. C. Han, *Facile creation of a super-amphiphobic coating surface with bionic microstructure*, Adv Mater **2004**, *16*, 302-305.

[109] R. T. R. Kumar, K. B. Mogensen, P. Boggild, *Simple Approach to Superamphiphobic Overhanging Silicon Nanostructures*, J Phys Chem C **2010**, *114*, 2936-2940.

[110] L. Joly, T. Biben, *Wetting and friction on superoleophobic surfaces*, Soft Matter **2009**, *5*, 2549-2557.

[111] C. M. Megaridis, R. A. Dobbins, *Morphological Description of Flame-Generated Materials*, Combust Sci Technol **1990**, *71*, 95-109.

[112] D. Bartolo, F. Bouamrirene, E. Verneuil, A. Buguin, P. Silberzan, S. Moulinet, *Bouncing or sticky droplets: Impalement transitions on superhydrophobic micropatterned surfaces*, Europhys Lett **2006**, *74*, 299-305.

[113] D. Richard, C. Clanet, D. Quere, *Surface phenomena - Contact time of a bouncing drop*, Nature **2002**, *417*, 811-811.

[114] W. Hollander, J. Schormann, W. Stober, F. J. Monig, N. Schwarzer, *Sensitive Integrated and Time-Resolved Aerosol Measurement by Means of Light-Transmission Changes of Metal-Coated Nuclepore Filters (Filter-Fotometer)*, Environ Sci Technol **1981**, *15*, 471-473.

[115] F. Caruso, R. A. Caruso, H. Mohwald, *Nanoengineering of inorganic and hybrid hollow spheres by colloidal templating*, Science **1998**, *282*, 1111-1114.

[116] M. Chen, L. M. Wu, S. X. Zhou, B. You, *A method for the fabrication of monodisperse hollow silica spheres*, Adv Mater **2006**, *18*, 801-806.

[117] M. Retsch, M. Schmelzeisen, H. J. Butt, E. L. Thomas, *Visible Mie Scattering in Nonabsorbing Hollow Sphere Powders*, Nano Lett **2011**, *11*, 1389-1394.

[118] A. S. Ahmed, A. A. Ali, M. A. Alhaider, *Measurement of Atmospheric Particle-Size Distribution during Sand Duststorm in Riyadh, Saudi-Arabia*, Atmos Environ **1987**, *21*, 2723-2725.

[119] S. Aman, J. Tomas, H. Kalman, *Breakage probability of irregularly shaped particles*, Chem Eng Sci **2010**, *65*, 1503-1512.

[120] T. Verho, C. Bower, P. Andrew, S. Franssila, O. Ikkala, R. H. A. Ras, *Mechanically Durable Superhydrophobic Surfaces*, Adv Mater **2011**, *23*, 673-678.

[121] A. R. Parker, C. R. Lawrence, *Water capture by a desert beetle*, Nature **2001**, *414*, 33-34.

[122] T. Wagner, C. Neinhuis, W. Barthlott, *Wettability and contaminability of insect wings as a function of their surface sculptures*, Acta Zool-Stockholm **1996**, *77*, 213-225.

[123] L. Feng, S. H. Li, Y. S. Li, H. J. Li, L. J. Zhang, J. Zhai, Y. L. Song, B. Q. Liu, L. Jiang, D. B. Zhu, *Super-hydrophobic surfaces: From natural to artificial*, Adv Mater **2002**, *14*, 1857-1860.

[124] P. Roach, N. J. Shirtcliffe, M. I. Newton, *Progess in superhydrophobic surface development*, Soft Matter **2008**, *4*, 224-240.

[125] F. Xia, L. Jiang, *Bio-inspired, smart, multiscale interfacial materials*, Adv Mater **2008**, *20*, 2842-2858.

[126] X. Yao, Q. W. Chen, L. Xu, Q. K. Li, Y. L. Song, X. F. Gao, D. Quere, L. Jiang, *Bioinspired Ribbed Nanoneedles with Robust Superhydrophobicity*, Adv Funct Mater **2010**, *20*, 656-662.

[127] G. R. J. Artus, J. Zimmermann, F. A. Reifler, S. A. Brewer, S. Seeger, *A superoleophobic textile repellent towards impacting drops of alkanes*, Appl Surf Sci **2012**, *258*, 3835-3840.

[128] H. Zhou, H. X. Wang, H. T. Niu, A. Gestos, X. G. Wang, T. Lin, *Fluoroalkyl Silane Modified Silicone Rubber/Nanoparticle Composite: A Super Durable, Robust Superhydrophobic Fabric Coating*, Adv Mater **2012**, *24*, 2409-2412.

[129] A. K. Kota, G. Kwon, W. Choi, J. M. Mabry, A. Tuteja, *Hydro-responsive membranes for effective oil-water separation*, Nature Communications **2012**, *3*, 1025.

[130] J. Y. Shiu, C. W. Kuo, W. T. Whang, P. L. Chen, *Observation of enhanced cell adhesion and transfection efficiency on superhydrophobic surfaces*, Lab Chip **2010**, *10*, 556-558.

[131] Y. Koc, A. J. de Mello, G. McHale, M. I. Newton, P. Roach, N. J. Shirtcliffe, *Nano-scale superhydrophobicity: suppression of protein adsorption and promotion of flow-induced detachment*, Lab Chip **2008**, *8*, 582-586.

[132] R. Dufour, P. Brunet, M. Harnois, R. Boukherroub, V. Thomy, V. Senez, *Zipping Effect on Omniphobic Surfaces for Controlled Deposition of Minute Amounts of Fluid or Colloids*, Small **2012**, *8*, 1229-1236.

[133] H. Mertaniemi, V. Jokinen, L. Sainiemi, S. Franssila, A. Marmur, O. Ikkala, R. H. A. Ras, *Superhydrophobic Tracks for Low-Friction, Guided Transport of Water Droplets*, Adv Mater **2011**, *23*, 2911-2914.

[134] X. Hong, X. F. Gao, L. Jiang, *Application of superhydrophobic surface with high adhesive force in no lost transport of superparamagnetic microdroplet*, J Am Chem Soc **2007**, *129*, 1478-1479.

[135] J. W. Krumpfer, T. J. McCarthy, *Dip-Coating Crystallization on a Superhydrophobic Surface: A Million Mounted Crystals in a 1 cm(2) Array*, J. Am. Chem. Soc. **2011**, *133*, 5764-5766.

[136] B. D. Hatton, J. Aizenberg, *Writing on Superhydrophobic Nanopost Arrays: Topographic Design for Bottom-up Assembly*, Nano Lett **2012**, *12*, 4551-4557.

[137] A. B. D. Cassie, S. Baxter, *Large Contact Angles of Plant and Animal Surfaces*, Nature **1945**, *155*, 21-22.

[138] C. W. Extrand, *Criteria for ultralyophobic surfaces*, Langmuir **2004**, *20*, 5013-5018.

[139] C. W. Extrand, *Model for contact angles and hysteresis on rough and ultraphobic surfaces*, Langmuir **2002**, *18*, 7991-7999.

[140] W. Choi, A. Tuteja, J. M. Mabry, R. E. Cohen, G. H. McKinley, *A modified Cassie-Baxter relationship to explain contact angle hysteresis and anisotropy on non-wetting textured surfaces*, Journal of Colloid and Interface Science **2009**, *339*, 208-216.

[141] P. Papadopoulos, X. Deng, L. Mammen, D. M. Drotlef, G. Battagliarin, C. Li, K. Mullen, K. Landfester, A. del Campo, H. J. Butt, D. Vollmer, *Wetting on the*

Microscale: Shape of a Liquid Drop on a Microstructured Surface at Different Length Scales, Langmuir **2012**, *28*, 8392-8398.

[142] E. Bormashenko, R. Pogreb, G. Whyman, M. Erlich, *Cassie-Wenzel wetting transition in vibrating drops deposited on rough surfaces: is the dynamic Cassie-Wenzel wetting transition a 2D or 1D affair?*, Langmuir **2007**, *23*, 6501-6503.

[143] H.-M. Kwon, A. T. Paxson, K. K. Varanasi, N. A. Patankar, *Rapid Deceleration-Driven Wetting Transition during Pendant Drop Deposition on Superhydrophobic Surfaces*, Phys Rev Lett **2011**, *106*, 036102.

[144] G. Manukyan, J. M. Oh, D. van den Ende, R. G. H. Lammertink, F. Mugele, *Electrical switching of wetting states on superhydrophobic surfaces: a route towards reversible Cassie-to-Wenzel transitions*, Physical Review Letters **2011**, *106*, 014501.

[145] F. O. Ochanda, M. A. Samaha, H. V. Tafreshi, G. C. Tepper, M. Gad-el-Hak, *Salinity effects on the degree of hydrophobicity and longevity for superhydrophobic fibrous coatings*, J Appl Polym Sci **2012**, *124*, 5021-5026.

[146] H. Kusumaatmaja, M. L. Blow, A. Dupuis, J. M. Yeomans, *The collapse transition on superhydrophobic surfaces*, EPL (Europhysics Letters) **2008**, *81*, 36003.

[147] G. McHale, S. Aqil, N. J. Shirtcliffe, M. I. Newton, H. Y. Erbil, *Analysis of droplet evaporation on a superhydrophobic surface*, Langmuir **2005**, *21*, 11053-11060.

[148] D. H. Kwon, S. J. Lee, *Impact and wetting behaviors of impinging microdroplets on superhydrophobic textured surfaces*, Appl Phys Lett **2012**, *100*, 171601.

[149] P. C. Tsai, R. G. H. Lammertink, M. Wessling, D. Lohse, *Evaporation-Triggered Wetting Transition for Water Droplets upon Hydrophobic Microstructures*, Phys Rev Lett **2010**, *104*, 116102.

[150] C. Dorrer, J. Ruhe, *Some thoughts on superhydrophobic wetting*, Soft Matter **2009**, *5*, 51-61.

[151] G. Whyman, E. Bormashenko, T. Stein, *The rigorous derivation of Young, Cassie-Baxter and Wenzel equations and the analysis of the contact angle hysteresis phenomenon*, Chem Phys Lett **2008**, *450*, 355-359.

[152] A. Susarrey-Arce, A. G. Marin, H. Nair, L. Lefferts, J. G. E. Gardeniers, D. Lohse, A. van Houselt, *Absence of an evaporation-driven wetting transition on omniphobic surfaces*, Soft Matter **2012**, *8*, 9765-9770.

[153] H. Kusumaatmaja, M. L. Blow, A. Dupuis, J. M. Yeomans, *The collapse transition on superhydrophobic surfaces*, Europhysics Letters **2008**, *81*, 36003.

[154] J. F. Oliver, C. Huh, S. G. Mason, *Resistance to Spreading of Liquids by Sharp Edges*, Journal of Colloid and Interface Science **1977**, *59*, 568-581.

[155] P. Papadopoulos, X. Deng, L. Mammen, D.-M. Drotlef, G. Battagliarin, C. Li, K. Muellen, K. Landfester, A. del Campo, H.-J. Butt, D. Vollmer, *Wetting on the microscale: shape of a liquid drop on a microstructured surface at different length scales*, Langmuir **2012**, *28*, 8392-8398.

[156] M. Reyssat, D. Quere, *Contact angle hysteresis generated by strong dilute defects*, Journal of Physical Chemistry B **2009**, *113*, 3906-3909.

[157] C. Luo, H. Zheng, L. Wang, H. P. Fang, J. Hu, C. H. Fan, Y. Cao, J. A. Wang, *Direct Three-Dimensional Imaging of the Buried Interfaces between Water and Superhydrophobic Surfaces*, Angew Chem Int Edit **2010**, *49*, 9145-9148.

[158] J. B. Wu, M. Y. Zhang, X. Wang, S. B. Li, W. J. Wen, *A Simple Approach for Local Contact Angle Determination on a Heterogeneous Surface*, Langmuir **2011**, *27*, 5705-5708.

[159] P. Papadopoulos, X. Deng, L. Mammen, D.-M. Drotlef, G. Battagliarin, C. Li, K. Müllen, K. Landfester, A. d. Campo, H.-J. Butt, D. Vollmer, *Wetting on the Microscale: Shape of a Liquid Drop on a Microstructured Surface at Different Length Scales*, Langmuir **2012**, *28*, 8392-8398.

[160] T. Weil, T. Vosch, J. Hofkens, K. Peneva, K. Muellen, *The Rylene Colorant Family-Tailored Nanoemitters for Photonics Research and Applications*, Angew. Chem. Intl. Ed. **2010**, *49*, 9068-9093.

[161] J. Q. Qu, C. Kohl, M. Pottek, K. Mullen, *Ionic perylenetetracarboxdiimides: Highly fluorescent and water-soluble dyes for biolabeling*, Angew. Chem. Int. Ed. **2004**, *43*, 1528-1531.

[162] D. Bonn, J. Eggers, J. Indekeu, J. Meunier, E. Rolley, *Wetting and spreading*, *Rev Mod Phys* **2009**, *81*, 739-805.

[163] H. Gau, S. Herminghaus, P. Lenz, R. Lipowsky, *Liquid morphologies on structured surfaces: From microchannels to microchips*, *Science* **1999**, *283*, 46-49.

[164] G. M. Whitesides, *The origins and the future of microfluidics*, *Nature* **2006**, *442*, 368-373.

[165] T. M. Squires, S. R. Quake, *Microfluidics: Fluid physics at the nanoliter scale*, *Rev Mod Phys* **2005**, *77*, 977-1026.

[166] A. L. Yarin, *Drop impact dynamics: Splashing, spreading, receding, bouncing...* *Annu Rev Fluid Mech* **2006**, *38*, 159-192.

[167] M. Reyssat, A. Pépin, F. Marty, Y. Chen, D. Quéré, *Bouncing transitions on microtextured materials*, *EPL (Europhysics Letters)* **2006**, *74*, 306.

[168] K.-C. Park, S. S. Chhatre, S. Srinivasan, R. E. Cohen, G. H. McKinley, *Optimal Design of Permeable Fiber Network Structures for Fog Harvesting*, *Langmuir* **2013**, *29*, 13269-13277.

[169] L. Zhai, M. C. Berg, F. C. Cebeci, Y. Kim, J. M. Milwid, M. F. Rubner, R. E. Cohen, *Patterned superhydrophobic surfaces: Toward a synthetic mimic of the Namib Desert beetle*, *Nano Lett* **2006**, *6*, 1213-1217.

[170] E. Ueda, P. A. Levkin, *Emerging Applications of Superhydrophilic-Superhydrophobic Micropatterns*, *Adv Mater* **2013**, *25*, 1234-1247.

[171] P. Lam, K. J. Wynne, G. E. Wnek, *Surface-tension-confined microfluidics*, *Langmuir* **2002**, *18*, 948-951.

[172] R. Wang, K. Hashimoto, A. Fujishima, M. Chikuni, E. Kojima, A. Kitamura, M. Shimohigoshi, T. Watanabe, *Light-induced amphiphilic surfaces*, *Nature* **1997**, *388*, 431-432.

[173] C. W. Extrand, *Contact angles and hysteresis on surfaces with chemically heterogeneous islands (vol 19, pg 3793, 2003)*, *Langmuir* **2005**, *21*, 11546-11546.

[174] J. S. S. Li, E. Ueda, A. Nallapaneni, L. X. X. Li, P. A. Levkin, *Printable Superhydrophilic-Superhydrophobic Micropatterns Based on Supported Lipid Layers*, *Langmuir* **2012**, *28*, 8286-8291.

[175] C. Dorrer, J. Ruhe, *Mimicking the stenocara beetle-dewetting of drops from a patterned superhydrophobic surface*, *Langmuir* **2008**, *24*, 6154-6158.

[176] U. Manna, A. H. Broderick, D. M. Lynn, *Chemical Patterning and Physical Refinement of Reactive Superhydrophobic Surfaces*, *Adv Mater* **2012**, *24*, 4291-4295.

[177] L. Mishchenko, M. Khan, J. Aizenberg, B. D. Hatton, *Spatial Control of Condensation and Freezing on Superhydrophobic Surfaces with Hydrophilic Patches*, *Adv Funct Mater* **2013**, *23*, 4577-4584.

[178] K. K. Varanasi, M. Hsu, N. Bhate, W. S. Yang, T. Deng, *Spatial control in the heterogeneous nucleation of water*, *Appl Phys Lett* **2009**, *95*, 094101.

[179] P. Papadopoulos, L. Mammen, X. Deng, D. Vollmer, H. J. Butt, *How superhydrophobicity breaks down*, *P Natl Acad Sci USA* **2013**, *110*, 3254-3258.

[180] T. Weil, T. Vosch, J. Hofkens, K. Peneva, K. Mullen, *The Rylene Colorant Family-Tailored Nanoemitters for Photonics Research and Applications*, *Angew Chem Int Edit* **2010**, *49*, 9068-9093.

[181] L. Mammen, P. Papadopoulos, K. Friedemann, S. Wanka, D. Crespy, D. Vollmer, H. J. Butt, *Transparent and airtight silica nano- and microchannels with uniform tubular cross-section*, *Soft Matter* **2013**, *9*, 9824-9832.

[182] T. Baumgartel, C. von Borczyskowski, H. Graaf, *Selective surface modification of lithographic silicon oxide nanostructures by organofunctional silanes*, *Beilstein J Nanotech* **2013**, *4*, 218-226.

[183] A. V. Fuchs, N. Kotman, J. Andrieu, V. Mailander, C. K. Weiss, K. Landfester, *Enzyme cleavable nanoparticles from peptide based triblock copolymers*, *Nanoscale* **2013**, *5*, 4829-4839.

[184] N. Vogel, L. de Viguerie, U. Jonas, C. K. Weiss, K. Landfester, *Wafer-Scale Fabrication of Ordered Binary Colloidal Monolayers with Adjustable Stoichiometries*, *Adv Funct Mater* **2011**, *21*, 3064-3073.

[185] M. Nosonovsky, B. Bhushan, *Biomimetic superhydrophobic surfaces: Multiscale approach*, *Nano Lett* **2007**, *7*, 2633-2637.

[186] A. ElSherbini, A. Jacobi, *Retention forces and contact angles for critical liquid drops on non-horizontal surfaces*, *Journal of Colloid and Interface Science* **2006**, *299*, 841-849.

[187] C. W. Extrand, Y. Kumagai, *Liquid-Drops on an Inclined Plane - the Relation between Contact Angles, Drop Shape, and Retentive Force*, *Journal of Colloid and Interface Science* **1995**, *170*, 515-521.

[188] A. T. Paxson, K. K. Varanasi, *Self-similarity of contact line depinning from textured surfaces*, *Nat Commun* **2013**, *4*, 1492.

[189] W. J. Li, F. Nicol, F. C. Szoka, *GALA: a designed synthetic pH-responsive amphipathic peptide with applications in drug and gene delivery*, *Adv Drug Deliver Rev* **2004**, *56*, 967-985.

[190] N. K. Subbarao, R. A. Parente, F. C. Szoka, L. Nadasdi, K. Pongracz, *Ph-Dependent Bilayer Destabilization by an Amphipathic Peptide*, *Biochemistry-Us* **1987**, *26*, 2964-2972.

[191] I. You, N. Yun, H. Lee, *Surface-Tension-Confined Microfluidics and Their Applications*, *Chemphyschem* **2013**, *14*, 471-481.

[192] N. Miljkovic, E. N. Wang, *Condensation heat transfer on superhydrophobic surfaces*, *Mrs Bull* **2013**, *38*, 397-406.

[193] S. Gogte, P. Vorobieff, R. Truesdell, A. Mammoli, F. van Swol, P. Shah, C. J. Brinker, *Effective slip on textured superhydrophobic surfaces*, *Physics of Fluids* **2005**, *17*, 051701.

[194] J. P. Rothstein, in *Annu Rev Fluid Mech, Vol. 42*, **2010**, pp. 89-109.

[195] D. BARTOLO, C. JOSSERAND, D. BONN, *Retraction dynamics of aqueous drops upon impact on non-wetting surfaces*, *J Fluid Mech* **2005**, *545*, 329-338.

[196] C. CLANET, C. BÉGUIN, Eacute, DRIC, D. RICHARD, D. QUÉRÉ, *Maximal deformation of an impacting drop*, *J Fluid Mech* **2004**, *517*, 199-208.

[197] F. L. Geyer, E. Ueda, U. Liebel, N. Grau, P. A. Levkin, *Superhydrophobic-Superhydrophilic Micropatterning: Towards Genome-on-a-Chip Cell Microarrays*, *Angew Chem Int Edit* **2011**, *50*, 8424-8427.

[198] J. Groten, J. Ruhe, *Surfaces with Combined Microscale and Nanoscale Structures: A Route to Mechanically Stable Superhydrophobic Surfaces?*, *Langmuir* **2013**, *29*, 3765-3772.

[199] A. Lenshof, T. Laurell, *Continuous separation of cells and particles in microfluidic systems*, *Chem Soc Rev* **2010**, *39*, 1203-1217.

[200] P. M. Sinha, G. Valco, S. Sharma, X. W. Liu, M. Ferrari, *Nanoengineered device for drug delivery application*, *Nanotechnology* **2004**, *15*, S585-S589.

[201] A. L. Yarin, E. Zussman, J. H. Wendorff, A. Greiner, *Material encapsulation and transport in core-shell micro/nanofibers, polymer and carbon nanotubes and micro/nanochannels*, *J Mater Chem* **2007**, *17*, 2585-2599.

[202] Y. J. Xiong, B. T. Mayers, Y. N. Xia, *Some recent developments in the chemical synthesis of inorganic nanotubes*, *Chem Commun* **2005**, 5013-5022.

[203] Y. Dror, W. Salalha, R. Avrahami, E. Zussman, A. L. Yarin, R. Dersch, A. Greiner, J. H. Wendorff, *One-step production of polymeric microtubes by co-electrospinning*, *Small* **2007**, *3*, 1064-1073.

[204] D. Li, J. T. McCann, Y. N. Xia, *Use of electrospinning to directly fabricate hollow nanofibers with functionalized inner and outer surfaces*, *Small* **2005**, *1*, 83-86.

[205] I. G. Loscertales, A. Barrero, M. Marquez, R. Spretz, R. Velarde-Ortiz, G. Larsen, *Electrically forced coaxial nanojets for one-step hollow nanofiber design*, *J Am Chem Soc* **2004**, *126*, 5376-5377.

[206] M. Wang, N. Jing, C. B. Su, J. Kameoka, C. K. Chou, M. C. Hung, K. A. Chang, *Electrospinning of silica nanochannels for single molecule detection*, *Appl Phys Lett* **2006**, *88*, 033106.

[207] R. A. Caruso, J. H. Schattka, A. Greiner, *Titanium dioxide tubes from sol-gel coating of electrospun polymer fibers*, *Adv Mater* **2001**, *13*, 1577-1579.

[208] G. Che, B. B. Lakshmi, C. R. Martin, E. R. Fisher, R. S. Ruoff, *Chemical vapor deposition based synthesis of carbon nanotubes and nanofibers using a template method*, *Chem Mater* **1998**, *10*, 260-267.

[209] X. Chen, A. Berger, M. Y. Ge, S. Hopfe, N. Dai, U. Gosele, S. Schlecht, M. Steinhart, *Silica Nanotubes by Templated Thermolysis of Silicon Tetraacetate*, *Chem Mater* **2011**, *23*, 3129-3131.

[210] L. M. Huang, H. T. Wang, C. Y. Hayashi, B. Z. Tian, D. Y. Zhao, Y. S. Yan, *Single-strand spider silk templating for the formation of hierarchically ordered hollow mesoporous silica fibers*, *J Mater Chem* **2003**, *13*, 666-668.

[211] S. S. Verbridge, J. B. Edel, S. M. Stavis, J. M. Moran-Mirabal, S. D. Allen, G. Coates, H. G. Craighead, *Suspended glass nanochannels coupled with microstructures for single molecule detection*, *J Appl Phys* **2005**, *97*, 124317.

[212] M. Steinhart, R. B. Wehrspohn, U. Gosele, J. H. Wendorff, *Nanotubes by template wetting: A modular assembly system*, *Angew Chem Int Edit* **2004**, *43*, 1334-1344.

[213] M. Bognitzki, H. Q. Hou, M. Ishaque, T. Frese, M. Hellwig, C. Schwarte, A. Schaper, J. H. Wendorff, A. Greiner, *Polymer, metal, and hybrid nano- and mesotubes by coating degradable polymer template fibers (TUFT process)*, *Adv Mater* **2000**, *12*, 637-640.

[214] M. Zhou, J. Y. Zhou, R. S. Li, E. Q. Xie, *Preparation of Aligned Ultra-long and Diameter-controlled Silicon Oxide Nanotubes by Plasma Enhanced Chemical Vapor Deposition Using Electrospun PVP Nanofiber Template*, *Nanoscale Res Lett* **2010**, *5*, 279-285.

[215] B. Zhang, M. Wood, H. Lee, *A Silica Nanochannel and Its Applications in Sensing and Molecular Transport*, *Anal Chem* **2009**, *81*, 5541-5548.

[216] V. D. Sobolev, N. V. Churaev, M. G. Velarde, Z. M. Zorin, *Surface tension and dynamic contact angle of water in thin quartz capillaries*, *J Colloid Interf Sci* **2000**, *222*, 51-54.

[217] J. T. McCann, D. Li, Y. N. Xia, *Electrospinning of nanofibers with core-sheath, hollow, or porous structures*, *J Mater Chem* **2005**, *15*, 735-738.

[218] A. L. Yarin, *Coaxial electrospinning and emulsion electrospinning of core-shell fibers*, *Polym Advan Technol* **2011**, *22*, 310-317.

[219] D. Quere, *Inertial capillarity*, *Europhys Lett* **1997**, *39*, 533-538.

[220] N. R. Tas, J. Haneveld, H. V. Jansen, M. Elwenspoek, A. van den Berg, *Capillary filling speed of water in nanochannels*, *Appl Phys Lett* **2004**, *85*, 3274-3276.

[221] B. V. Zhmud, F. Tiberg, K. Hallstensson, *Dynamics of capillary rise*, *J Colloid Interf Sci* **2000**, *228*, 263-269.

[222] F. Vollrath, D. Porter, C. Holland, *The science of silks*, *Mrs Bull* **2013**, *38*, 73-80.

[223] D. Li, Y. N. Xia, *Electrospinning of nanofibers: Reinventing the wheel?*, *Adv Mater* **2004**, *16*, 1151-1170.

[224] D. H. Reneker, I. Chun, *Nanometre diameter fibres of polymer, produced by electrospinning*, *Nanotechnology* **1996**, *7*, 216-223.

[225] T. Subbiah, G. S. Bhat, R. W. Tock, S. Pararneswaran, S. S. Ramkumar, *Electrospinning of nanofibers*, *J Appl Polym Sci* **2005**, *96*, 557-569.

[226] L. Romer, T. Scheibel, *The elaborate structure of spider silk Structure and function of a natural high performance fiber*, *Prion* **2008**, *2*, 154-161.

[227] A. Sponner, W. Vater, S. Monajembashi, E. Unger, F. Grosse, K. Weisshart, *Composition and Hierarchical Organisation of a Spider Silk*, *Plos One* **2007**, *2*, 2(10): e998.

[228] A. Han, G. Mondin, N. G. Hegelbach, N. F. de Rooij, U. Staufer, *Filling kinetics of liquids in nanochannels as narrow as 27 nm by capillary force*, *J Colloid Interf Sci* **2006**, *293*, 151-157.

[229] J. Haneveld, N. R. Tas, N. Brunets, H. V. Jansen, M. Elwenspoek, *Capillary filling of sub-10 nm nanochannels*, *J Appl Phys* **2008**, *104*, 014309.

[230] H. Brenner, J. R. Happel, *Low Reynolds Number Hydrodynamics, Vol. 1*, Springer, **1983**.

[231] R. G. Cox, *The Dynamics of the Spreading of Liquids on a Solid-Surface .1. Viscous-Flow*, *J Fluid Mech* **1986**, *168*, 169-194.

[232] O. V. Voinov, *Hydrodynamics of wetting*, *Fluid Dyn* **1976**, 714-721.

LIST OF PUBLICATIONS

PUBLICATIONS

L. Mammen, K. Bley, P. Papadopoulos, F. Schellenberger, H. J. Butt, C. K. Weiss and D. Vollmer. *Superhydrophobic Arrays of Functional Janus Micropillars*. Submitted, **2013**.

D. Vijayshankar, L. Mammen, P. Papadopoulos and D. Vollmer. *Nanorough Silica Coatings by Chemical Vapor Deposition*. Submitted, **2013**.

M. Paven, P. Papadopoulos, L. Mammen, X. Deng, H. Sachdev, D. Vollmer and H. J. Butt. *Optimization of Superamphiphobic Layers Based on Candle Soot*. Submitted, **2013**.

P. Papadopoulos, L. Mammen, X. Deng, D. Vollmer and H. J. Butt. *How Superhydrophobicity Breaks Down. P. Natl. Acad. Sci. USA* **2013,** *110* (9), 3254-3258.

L. Mammen, P. Papadopoulos, K. Friedemann, S. Wanka, D. Crespy, D. Vollmer, H. J. Butt. *Transparent and Airtight Silica Nano- and Microchannels with Uniform Tubular Cross-Section. Soft Matter* **2013,** *9* (41), 9824-9832.

P. Papadopoulos, L. Mammen, X. Deng, D. Vollmer and H. J. Butt. *Pinning-Induced Variations of the Contact Angle of Drops on Microstructured Surfaces. Chem. Lett.* **2012,** *41* (10), 1343-1345.

P. Papadopoulos, X. Deng, L. Mammen, D. M. Drotlef, G. Battagliarin, C. Li, K. Mullen, K. Landfester, A. del Campo, H. J. Butt and D. Vollmer. *Wetting on the Microscale: Shape of a Liquid Drop on a Microstructured Surface at Different Length Scales. Langmuir* **2012,** *28* (22), 8392-8398.

L. Mammen, X. Deng, M. Untch, D. Vijayshankar, P. Papadopoulos, R. Berger, E. Riccardi, F. Leroy and D. Vollmer. *Effect of Nanoroughness on Highly Hydrophobic and Superhydrophobic Coatings. Langmuir* **2012,** *28* (42), 15005-15014.

M. Klapper, F. Golling, T. Schuster, L. Mammen, D. Vollmer and K. Müllen. *The Power of Perfluorinated Amphiphilic Polymers at Interfaces.* ACS Books: *Advances in Fluorine-Containing Polymers* **2012**, *1106*, Chap. 8, 111-126.

X. Deng, L. Mammen, H. J. Butt and D. Vollmer. *Candle Soot as a Template for a Transparent Robust Superamphiphobic Coating. Science* **2012,** *335* (6064), 67-70.

X. Deng, L. Mammen, Y. F. Zhao, P. Lellig, K. Mullen, C. Li, H. J. Butt and D. Vollmer. *Transparent, Thermally Stable and Mechanically Robust Superhydrophobic Surfaces Made from Porous Silica Capsules. Adv. Mater.* **2011,** *23* (26), 2962-2965.

D. Vollmer, L. Mammen, X. Deng und H. J. Butt. *Dem Lotus abgeschaut. Farbe und Lack* **2011**, *11*, 26-31.

M. D'Acunzi, L. Mammen, M. Singh, X. Deng, M. Roth, G. K. Auernhammer, H. J. Butt and D. Vollmer. *Superhydrophobic Surfaces by Hybrid Raspberry-Like Particles. Faraday Discuss.* **2010,** *146*, 35-48.

PATENT APPLICATIONS

D. Vollmer, M. D'Acunzi, L. Mammen, X. Deng, M. Klapper and H. J. Butt. *Mechanical Stable, Transparent, Superhydrophobic, and - Oleophobic Surfaces Made of Hybrid Raspberry-Like Particles.* Internationale Patentanmeldung Nr. PCT/EP2012/051971.

H. J. Butt, D. Vollmer, X. Deng, M. Paven, P. Papadopoulos, L. Mammen. *Method and device for transferring gas molecules from a gaseous medium into a liquid medium or vice versa.* Europäische Patentanmeldung Nr. 12008422.3.

CONFERENCE CONTRIBUTIONS

03/2013   Annual meeting of the German Physical Society (DPG),
               Regensburg, Germany:

               *Transparent and Airtight Silica Nano- and Microchannels
               with Uniform Tubular Cross-Section*, Poster

06/2012   19th Surfactants in Solutions (SIS) Conference,
               Edmonton, Canada:

               *Superhydrophobic Surfaces with Multiscale Roughness
               Made from Raspberry Particles*, Talk

               *Transparent Silica Nano- and Microchannels for
               Microfluidic Devices*, Poster

03/2012   8th Zsigmondy Kolloquium, Darmstadt, Germany:

               *Transparent Silica Nano- and Microchannels for
               Microfluidic Devices*, Poster

06/2011   13th European Student Colloid (ESC) Conference,
               Falkenberg, Sweden:

               *Superhydrophobic Surfaces with Multiscale Roughness
               Made from Raspberry Particles*, Poster

DANKSAGUNG

[In der elektronischen Fassung aus Datenschutzgründen entfernt]

DANKSAGUNG

CURRICULUM VITAE

[In der elektronischen Fassung aus Datenschutzgründen entfernt]